

# Electromagnetic NDE

Peter B. Nagy

School of Aerospace Systems

University of Cincinnati

Cincinnati, Ohio 45221, USA

and

UK Research Centre in NDE

Imperial College

London, SW7 2AZ, UK

March 2011

## Table of Contents

Introduction .....	4
1 Electromagnetism .....	4
1.1 Fundamentals .....	5
1.2 Maxwell's Equations .....	13
1.3 Electromagnetic Wave Propagation .....	15
2 Eddy Current Theory .....	22
2.1 Eddy Current Method .....	22
2.2 Impedance Diagrams .....	25
2.3 Test Coil Impedance .....	28
2.4 Field Distributions .....	36
3 Eddy Current NDE .....	39
3.1 Eddy Current Inspection Techniques .....	39
3.2 Eddy Current Applications .....	47
3.2.1 Conductivity .....	48
3.2.2 Permeability .....	52
3.2.3 Metal Thickness .....	55
3.2.4 Coating Thickness .....	58
3.2.5 Depth Profiling .....	60
3.2.6 Flaw Detection .....	66
3.3 Eddy Current Materials Characterization .....	74
3.3.1 Texture .....	75
3.3.2 Grain Structure .....	80

3.3.3 Hardness .....	82
3.3.4 Residual Stress .....	84
4 Current Field Measurement .....	88
4.1 Alternating Current Field Measurement .....	89
4.2 Direct Current Potential Drop .....	92
4.3 Alternating Current Potential Drop .....	97
5 Special Inspection Methods .....	99
5.1 Microwave Inspection .....	100
5.2 Dielectric Inspection .....	106
5.3 Thermoelectric Inspection .....	111
Exercise Problems .....	116
References .....	122

## ***Introduction***

The aim of this Chapter is to familiarize the readers with Electromagnetic (EM) Nondestructive Evaluation (NDE), to integrate this knowledge into their broader understanding of NDE principles and to enable them to judge the applicability, advantages, disadvantages, and technical limitations of EM techniques when faced with NDE challenges. Section 1 reviews the fundamental physical principles of EM NDE methods with special emphasis on electromagnetic wave propagation. Section 2 focuses on diffuse eddy current fields in conducting materials and the principal relationship between the measured complex electric impedance of the probe coil and the sought electromagnetic properties of the material under test. Section 3 and 4 review the main Eddy Current and Current Field Measurement techniques, respectively. Finally, Section 5 introduces three emerging special EM NDE methods, namely Microwave, Dielectric, and Thermoelectric inspections.

### ***1 Electromagnetism***

This introductory section briefly reviews the fundamental physical principles of electromagnetism and lays down the groundwork for subsequent sections on electromagnetic NDE. The theory of electromagnetism is built on a series of empirical discoveries such as Coulomb's law for electric forces acting between charged objects [1], Ampère's law for the strength of magnetic field produced by a current carrying wire [2], and Faraday's law for the induction of an electromotive force by magnetic fields that vary with time [3]. These discoveries led to the formulation of Maxwell's famous set of four coupled partial differential equations that govern all classical electromagnetic phenomena [4]. For a deeper discussion and historical overview of electromagnetics the interested reader should consult the classic text by Elliott [5].

The second part of this section introduces the reader to electromagnetic wave propagation

first in dielectrics and then in conductors where the diffuse nature of the electromagnetic field leads to specific phenomena of great practical importance that lie at the foundation of the arguably most important electromagnetic NDE method, eddy current inspection. Undoubtedly, the reader has a tremendous variety of excellent textbooks on electromagnetism to choose from (see, for example, [6-10] to name a few). Still, it is likely that a brief review of the foundations of EM NDE would be a valuable addition to this book and might help the reader navigate through the remainder of this and the following chapters.

### 1.1 Fundamentals

In its simplest form, electricity exhibits itself through an electrostatic  $\mathbf{F}_e$  Coulomb force between two point charges  $Q_1$  and  $Q_2$  as shown in Figure 1a.

$$\mathbf{F}_e = \frac{Q_1 Q_2}{4\pi\epsilon r^2} \mathbf{e}_r, \quad (1)$$

where  $\mathbf{e}_r$  is the unit vector directed from the source to the target,  $r$  is the distance between the charges, and  $\epsilon$  is the permittivity (for free space,  $\epsilon_0 \approx 8.85 \times 10^{-12}$  As/Vm). Because of the discrete nature of electric charges, both  $Q_1$  and  $Q_2$  must be equal to  $\pm ne$ , where  $n$  is an integer and  $e \approx 1.602 \times 10^{-19}$  As is the charge of a proton. It is instructive to consider the electrostatic force acting between an infinite plane of uniform charge density  $q$  and a point charge  $Q_1$  placed at a distance  $x$  from it as shown in Figure 1b. The Coulomb force can be readily calculated from

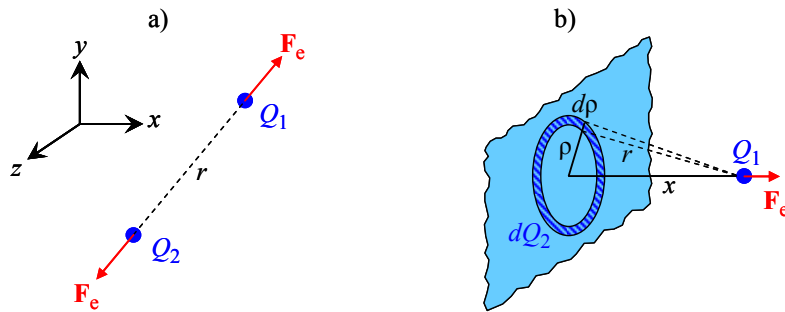


Figure 1 Electrostatic force between (a) two point charges and (b) an infinite plane of uniform charge density and a point charge.

Eq. (1) by integration as follows

$$\mathbf{F}_e = \frac{Q_1 q x \mathbf{e}_x}{4\pi\epsilon} \iint \frac{2\pi\rho d\rho}{r^3} = \frac{Q_1 q x \mathbf{e}_x}{2\epsilon} \int_{r=x}^{\infty} \frac{dr}{r^2} = \frac{Q_1 q \mathbf{e}_x}{2\epsilon}, \quad (2)$$

i.e., it is independent of the distance between the plane and the point charge since the plane is infinitely large, therefore produces a uniform electric field on both sides.

The electric field intensity, or briefly electric field,  $\mathbf{E}$  at any given point is defined as the electric force acting on a unit charge at that point so that for an arbitrary charge  $Q$

$$\mathbf{F}_e = \mathbf{E} Q. \quad (3)$$

The electric field of a single positive point charge  $Q$  is an outgoing spherical field of  $\mathbf{E} = Q/(4\pi\epsilon r^2)\mathbf{e}_r$ , while that of an infinite plane of uniform positive charge density  $q$  is a uniform field  $\mathbf{E} = q/(2\epsilon)\mathbf{e}_x$  directed away from the plane on both sides. The latter formula can be easily extended to approximate the electrostatic field between the parallel plane electrodes of the simple capacitor shown in Figure 2. Assuming that the dimensions of the two electrodes of area  $A$  facing each other is much larger than the separation distance  $\ell$  between them, the individual fields of the oppositely charged electrodes cancel each other outside the capacitor, while inside they add together to produce a more or less uniform normal electric field  $E = q/\epsilon$ , where the charge density is simply  $q = Q/A$ .

Electric charges often occur in pairs of equal magnitude and opposite sign separated by a

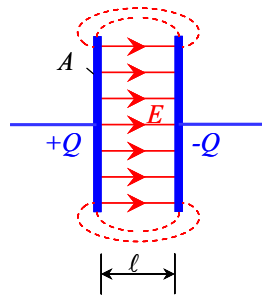


Figure 2 Essentially uniform normal electrostatic field  $E$  between the parallel electrodes of a charged plane capacitor.

small distance  $\mathbf{d}$ , which is called a dipole. Figure 3 shows an electric dipole  $\mathbf{p}_e = Q\mathbf{d} = Qd\mathbf{e}_d$  placed in an electric field  $\mathbf{E}$ . The resulting electrostatic force on the dipole is zero, but a torque

$$\mathbf{T}_e = \mathbf{d} \times \mathbf{F}_e = \mathbf{p}_e \times \mathbf{E} \quad (4)$$

acts to align the dipole with the external electric field.

The work  $W_{AB}$  done when moving an electric charge from point A to point B under the influence of an electric field  $\mathbf{E}$  can be calculated as follows

$$W_{AB} = -Q \int_A^B \mathbf{E} \cdot d\mathbf{l}. \quad (5)$$

The electric potential energy of the charge is  $U = QV$ , where  $V$  denotes the potential of the electric field  $V$ . Due to energy conservation, the potential energy of the charge increases by an amount equal to the work done while moving it from point A to point B, i.e.,  $\Delta U = W_{AB}$ , so that

$$\Delta V = V_B - V_A = - \int_A^B \mathbf{E} \cdot d\mathbf{l}, \quad (6)$$

or  $\mathbf{E} = -\nabla V$ . The electric capacitance of a charged device is defined as  $C = Q/V$ , where  $Q$  is the stored electric charge when the potential difference between the electrodes is  $V$ . For example, the uniform normal electric field between the parallel flat electrodes of the plane capacitor previously shown in Figure 2 is  $E = Q/(\epsilon A)$ , therefore the potential difference between them is  $V = E\ell$  and the electric capacitance can be calculated from the well-known equation  $C =$

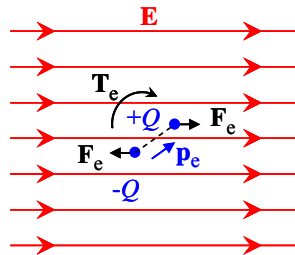


Figure 3 Torque  $\mathbf{T}_e$  acting on an electric dipole  $\mathbf{p}_e$  in an electric field  $\mathbf{E}$ .

$\epsilon A / \ell$ .

In three-dimensions, the electric flux density  $\mathbf{D}$  is given by  $\nabla \cdot \mathbf{D} = q$ , where  $q$  denotes the volumetric charge density. Figure 4a illustrates the electric flux  $\Psi$  crossing a closed surface  $S$ . According to Gauss' law,  $\Psi$  must be equal to the total enclosed electric charge

$$\Psi = \iint_S \mathbf{D} \cdot d\mathbf{S} = \iiint_V q dV = Q_{\text{enc}} \quad (7)$$

and a quick comparison with Eqs. (1) and (3) shows that  $\mathbf{D} = \epsilon \mathbf{E}$ , i.e., the electric flux density is equal to the electric field multiplied by the electric permittivity, which is the principal constitutive equation of all dielectric (nonconducting) materials.

The electric current  $I$  flowing through a given cross section  $A$  of a conducting material is defined as the total charge crossing  $A$  over a unit time period, i.e.,  $I = dQ/dt$  and can be also calculated by integrating the convection current density  $\mathbf{J}$  over  $A$  as illustrated in Figure 4b so that  $I = \iint \mathbf{J} \cdot d\mathbf{A}$ . In metals and other materials containing free charge carriers, the current density is proportional to the electric field  $\mathbf{J} = \sigma \mathbf{E}$ , which is the principal constitutive equation of all conducting materials.

Up to this point we considered static or quasi-static problems. Generally, the total so-called Lorenz force  $\mathbf{F} = \mathbf{F}_e + \mathbf{F}_m$  acting on moving charges includes not only an electric force  $\mathbf{F}_e$ , but

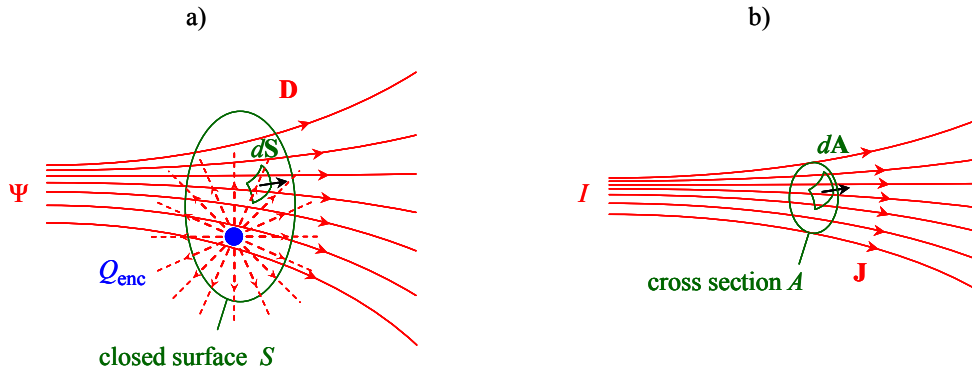


Figure 4 Schematic diagrams of (a) electric flux  $\Psi$  crossing a closed surface  $S$  and (b) electric current  $I$  flowing through a cross sectional area  $A$  of a conductor.



also a magnetic force  $\mathbf{F}_m$  which depends not only on the charge  $Q$  but also on its velocity  $\mathbf{v}$  as follows

$$\mathbf{F}_m = Q \mathbf{v} \times \mathbf{B}, \quad (8)$$

where  $\mathbf{B}$  is the magnetic flux density. As it is illustrated in Figure 5a, the magnetic force is always normal to the instantaneous velocity and the local magnetic flux density.

When an electric current  $I$  flowing in a closed loop interacts with a magnetic flux density  $\mathbf{B}$ , as it is shown in Figure 5b, the pair formed by the magnetic force acting on the moving charge carriers produces a magnetic torque  $\mathbf{T}_m$  that can be calculated from

$$\mathbf{T}_m = \mathbf{p}_m \times \mathbf{B}, \quad (9)$$

where  $\mathbf{p}_m = N I \mathbf{A}$  is the so-called magnetic dipole moment,  $N$  is the number of turns in the loop and  $\mathbf{A}$  is the encircled vector area. This relationship is analogous to Eq. (4) showing the electric torque produced by the electric field on an electric dipole moment. It should be mentioned, that the magnetic force acts only on moving charge carriers, and in the case of a current flowing through the turns of a conducting coil this force is transferred to the conductor via collisions between the lattice and the moving charge carriers.

A static magnetic field can be produced either by a constant current or a permanent magnet

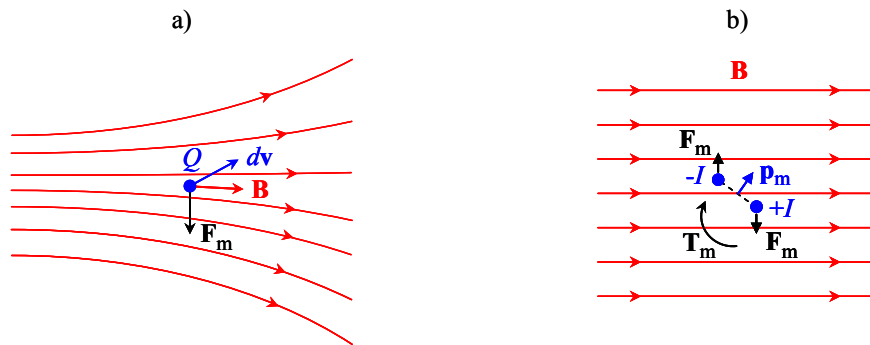


Figure 5 Schematic diagrams of (a) magnetic force  $\mathbf{F}_m$  acting on a moving charge and (b) torque  $\mathbf{T}_m$  acting on a magnetic dipole  $\mathbf{p}_m$  produced by a current loop.

which is created by preferential macroscopic alignment of spinning charges and microscopic current loops formed by orbiting charges. In this section we will consider only the magnetic field strength  $\mathbf{H}$ , or briefly magnetic field, produced by a current  $I$  flowing around a path  $\ell$ . According to the Biot-Savart law, for a closed current loop, the integrated magnetic field can be calculated as follows

$$\mathbf{H} = \oint \frac{I d\ell}{4\pi r^2} \mathbf{e}_\ell \times \mathbf{e}_r . \quad (10)$$

In a similar way as the electric flux density  $\mathbf{D}$  is proportional to the electric field  $\mathbf{E}$ , the magnetic flux density  $\mathbf{B}$  is proportional to the magnetic field  $\mathbf{H}$  via  $\mathbf{B} = \mu\mathbf{H}$ , where  $\mu$  is the magnetic permeability (for free space,  $\mu_0 = 4\pi \times 10^{-7}$  Vs/Am). Using Stokes' theorem, the Biot-Savart law can be re-written in a differential form called Ampère's law that states that the closed-loop vector integral of the magnetic field around the boundary of a surface area is equal to the total current passing through that surface

$$\oint \mathbf{H} \cdot d\mathbf{s} = I_{\text{enc}} . \quad (11)$$

This relationship is analogous to Gauss' law given by Eq. (7) that states that the vector integral of the electric flux density over a closed surface is equal to the total electric charge enclosed by that surface.

Ampère's law explains how an electric field can give rise to a magnetic field through conduction current. However, this is only half of the two-way relationship between electric and magnetic fields that is the underlying physical mechanism behind electromagnetism. The other half of this relationship is how a changing magnetic field can give rise to an electric field via induction. Figure 6a illustrates electromagnetic induction in a loop by a changing magnetic flux

$\Phi$ . According to Faraday's law, the induced electromotive force  $\mathcal{E}$  is equal to the negative of the time rate of change of the total magnetic flux  $\Phi$  passing through the surface encircled by the loop

$$\mathcal{E} = -\frac{\partial\Phi}{\partial t} = -\frac{\partial}{\partial t} \iint_S \mathbf{B} \cdot d\mathbf{S} . \quad (12)$$

Again, we can re-write Faraday's law using Stokes' theorem in a differential form which states that the curl of the induced electric field  $\mathbf{E}$  is equal to the negative of the time rate of change of the magnetic flux density  $\nabla \times \mathbf{E} = -\partial \mathbf{B} / \partial t$ .

Let us assume that a current  $I$  flows through a coil of  $N$  turns as shown in Figure 6b. The total flux  $\Phi$  generated by this current can be calculated by first determining the magnetic field  $\mathbf{H}$  using the Biot-Savart law and then integrating  $\mathbf{B} = \mu \mathbf{H}$  over the cross section of the coil, which yields  $\Phi = \mu N I \Lambda$ , where  $\Lambda$  is geometrical constant determined by the size and shape of the coil. When the current flowing through the coil changes, an electric voltage  $V$  is induced between the ends of the coil so that  $V = -\mathcal{E} = N d\Phi / dt$ . The ratio between the induced voltage and the time rate of change of the current is called the self-inductance, or briefly just inductance,  $L$  of the coil

$$V = L \frac{dI}{dt} , \quad (13)$$

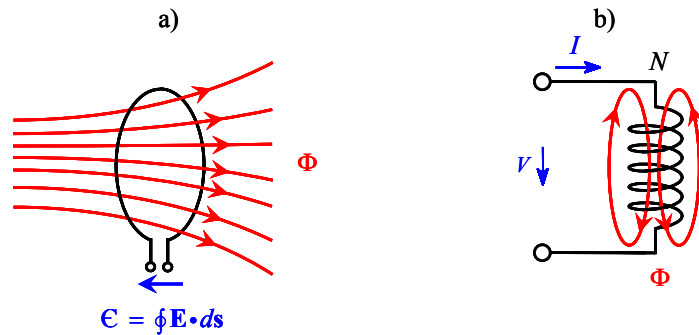


Figure 6 Schematic diagrams of (a) electromagnetic induction in a loop by a changing magnetic flux and (b) self-induction in a coil.

where the inductance can be expressed with the parameters of the coil as  $L = \mu N^2 \Lambda$ . An alternative definition of the inductance that is also used in the literature is based on the total flux generated by the coil  $\Phi = I L / N$ , which can be shown to be identical to Eq. (13).

Figure 7 illustrates the boundary conditions that static electric and magnetic fields must satisfy at a plane interface between two media. Gauss' laws for electric charges and magnetic monopoles require the continuity of the normal components of the (a) electric flux density  $D_{I,n} = D_{II,n}$  and (b) magnetic flux density  $B_{I,n} = B_{II,n}$ , respectively, while Faraday's and Ampère's laws require the continuity of the tangential components of the (c) electric field  $E_{I,t} = E_{II,t}$  and (d) magnetic field  $H_{I,t} = H_{II,t}$ , respectively.

Combining the two electric boundary conditions yields the rule of refraction for static electric fields

$$\frac{\tan \theta_I}{\epsilon_I} = \frac{\tan \theta_{II}}{\epsilon_{II}}, \quad (14a)$$

while similarly combining the two magnetic boundary conditions yields the rule of refraction for static magnetic fields

$$\frac{\tan \theta_I}{\mu_I} = \frac{\tan \theta_{II}}{\mu_{II}}. \quad (14b)$$

These static refraction rules are separate because the electric and magnetic fields are not coupled to each other. For coupled dynamic electric and magnetic fields constituting an electromagnetic wave, the same boundary conditions will apply in a simplified form and refraction directions will be governed by the well known Snell's law.

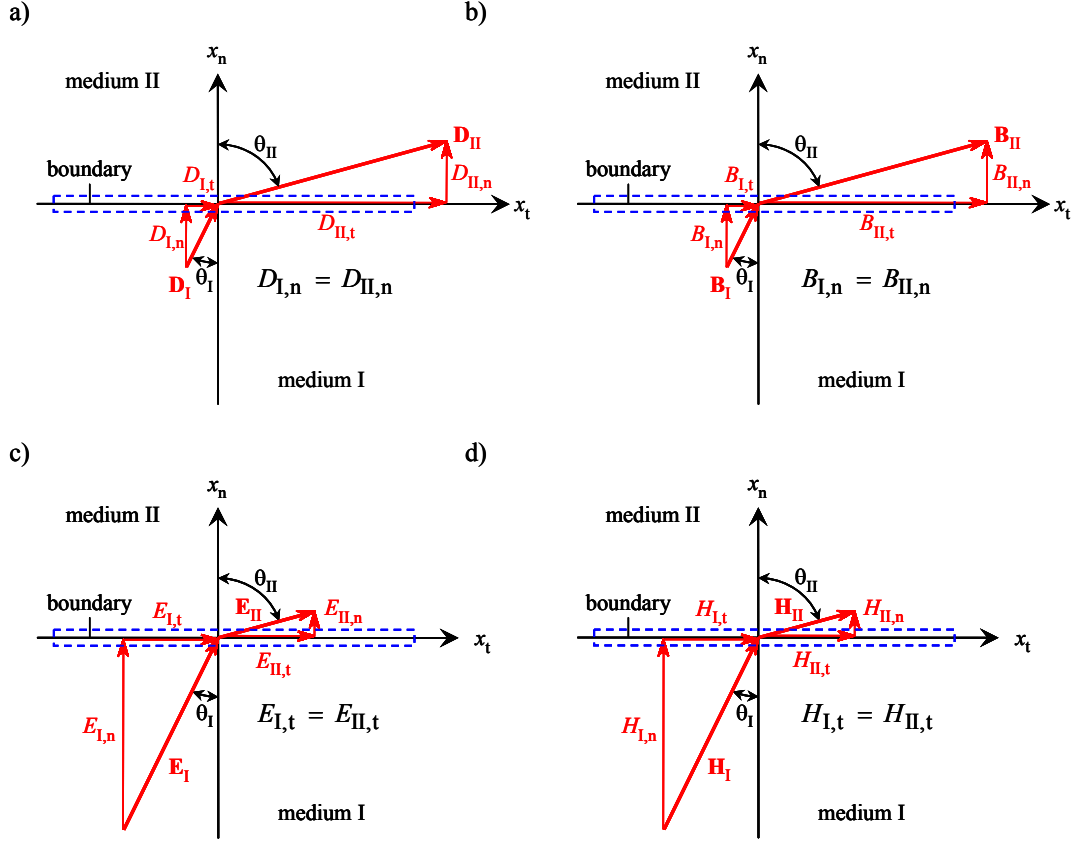


Figure 7 Boundary conditions at a plane interface between two media require the continuity of the normal components of the electric (a) and magnetic (b) flux densities and the tangential components of the electric (c) and magnetic (d) fields.

### 1.2 Maxwell's Equations

The fundamental empirical laws of electromagnetism introduced in the previous section can be conveniently compiled in a set of four partial differential equations named after Maxwell. Using the earlier notation, these equations are (i) Ampère's modified law

$$\nabla \times \mathbf{H} = \mathbf{J} + \frac{\partial \mathbf{D}}{\partial t}, \quad (15a)$$

which can be derived from Eq. (11) using Stokes' theorem and adding the so called displacement current density  $\partial \mathbf{D} / \partial t$  to the conduction current density  $\mathbf{J}$  in order to account for dynamic magnetic fields generated in dielectric media, (ii) Faraday's law

$$\nabla \times \mathbf{E} = -\frac{\partial \mathbf{B}}{\partial t}, \quad (15b)$$

which was previously derived from Eq. (12), (iii) Gauss' law for electric charges

$$\nabla \cdot \mathbf{D} = q, \quad (15c)$$

which is equivalent to Eq. (7), and (iv) Gauss' law for magnetic monopoles

$$\nabla \cdot \mathbf{B} = 0, \quad (15d)$$

which cannot exist as magnetic flux lines always form closed loops. In order to describe electromagnetic phenomena, these four field equations must be supplemented by three constitutive equations. In their simplest linearized isotropic form these are (i) the relationship between electric field and conduction current density in conductors

$$\mathbf{J} = \sigma \mathbf{E}, \quad (16a)$$

(ii) the relationship between electric field and electric flux density in dielectrics

$$\mathbf{D} = \varepsilon \mathbf{E}, \quad (16b)$$

and the relationship between magnetic field and magnetic flux density

$$\mathbf{B} = \mu \mathbf{H}, \quad (16c)$$

where  $\sigma$ ,  $\varepsilon$ , and  $\mu$  denote the electric conductivity, permittivity, and magnetic permeability of the medium, respectively. It should be pointed out that, in contrast to conductivity, the electric permittivity and magnetic permeability cannot be considered as pure material properties since they exhibit well-defined finite values, listed earlier as  $\varepsilon_0$  and  $\mu_0$ , even in the absence of material, i.e., in free space. Therefore, in order to describe electric and magnetic polarization in real

materials, the electric permittivity and magnetic permeability are often expressed as  $\epsilon = \epsilon_0 \epsilon_r$  and  $\mu = \mu_0 \mu_r$ , where  $\epsilon_r$  and  $\mu_r$  are called relative permittivity and relative permeability, respectively.

### 1.3 Electromagnetic Wave Propagation

Let us look for a time-harmonic solution of Maxwell's equations in order to study electromagnetic wave propagation in various media. Then, the electric and magnetic fields can be written in complex notation as  $\mathbf{E} = \mathbf{E}_0 e^{i\omega t}$  and  $\mathbf{H} = \mathbf{H}_0 e^{i\omega t}$ , where  $\omega$  denotes the angular frequency and  $\mathbf{E}_0$  and  $\mathbf{H}_0$  are complex amplitudes. Substituting these solutions into Eqs. (15a) and (15b), taking their curl, and then exploiting the vector identity  $\nabla \times (\nabla \times \mathbf{A}) = \nabla(\nabla \cdot \mathbf{A}) - \nabla^2 \mathbf{A}$  yields identical wave equations for the electric and magnetic fields in the form

$$(\nabla^2 + k^2)\mathbf{E} = \mathbf{0} \quad (17a)$$

and

$$(\nabla^2 + k^2)\mathbf{H} = \mathbf{0}, \quad (17b)$$

where  $k^2 = -i\omega\mu(\sigma + i\omega\epsilon)$ . In one dimension (e.g., along the  $x$ -axis), the plane wave solutions of these wave equations can be written as  $\mathbf{E} = E_y \mathbf{e}_y = E_0 e^{i(\omega t - kx)} \mathbf{e}_y$  and  $\mathbf{H} = H_z \mathbf{e}_z = H_0 e^{i(\omega t - kx)} \mathbf{e}_z$ , where  $k$  is the wave number. Both fields are transversely polarized with respect to the propagation direction and they are mutually orthogonal to each other (the polarization of the electric field was chosen arbitrarily to coincide with the  $y$ -axis). The complex velocity of the electromagnetic wave is  $c = \omega/k$  while the constant ratio between the amplitudes of the electric and magnetic fields is called the intrinsic wave impedance of the medium

$$\eta = \frac{E_0}{H_0} = \sqrt{\frac{i\omega\mu}{\sigma + i\omega\epsilon}}. \quad (18)$$

For our immediate purposes, three cases should be distinguished. First, in free space  $\varepsilon = \varepsilon_0$ ,  $\mu = \mu_0$ , and  $\sigma = 0$ , therefore  $k$  is real and the phase velocity of the resulting propagating wave is equal to the velocity of light in a vacuum  $c_0 = 1/\sqrt{\mu_0 \varepsilon_0} \approx 3 \times 10^8$  m/s and the intrinsic wave impedance is  $\eta_0 = \sqrt{\mu_0 / \varepsilon_0} \approx 377 \Omega$ . Second, in a dielectric material  $\varepsilon = \varepsilon_0 \varepsilon_r$ ,  $\mu = \mu_0$ , and  $\sigma = 0$ , therefore  $k$  is still real and the phase velocity of the propagating wave is  $c = c_0/n$ , where  $n = \sqrt{\varepsilon_r}$  is the so-called refractive index while the intrinsic wave impedance is  $\eta = \eta_0/n$ . Third, in a conducting material when  $\sigma \gg \omega \varepsilon$ , which is satisfied in all metals and their alloys up to very high frequencies beyond our range of interest in electromagnetic nondestructive evaluation, the wave number is complex with real and imaginary parts of equal magnitude  $k = \sqrt{-i \omega \mu \sigma} = 1/\delta - i/\delta$ , where  $\delta$  is called the standard penetration depth or skin depth

$$\delta = \frac{1}{\sqrt{\pi f \mu \sigma}} \quad (19)$$

and  $f$  denotes the cyclic frequency ( $\omega = 2\pi f$ ). Using the frequency-dependent standard penetration depth, the previously given general plane wave solution can be re-written as a diffuse wave of the form  $\mathbf{E} = E_0 e^{-x/\delta} e^{i(\omega t - x/\delta)} \mathbf{e}_y$  and  $\mathbf{H} = H_0 e^{-x/\delta} e^{-i(\omega t - x/\delta)} \mathbf{e}_z$ , while the intrinsic impedance is also complex  $\eta = (1 + i)/(\sigma \delta)$ .

Electromagnetic waves are always transversely polarized, therefore there are two mutually orthogonal polarization directions for plane waves propagating in the  $x$ -direction

$$\mathbf{E} = E_y \mathbf{e}_y + E_z \mathbf{e}_z = E_{y0} e^{i(\omega t - kx)} \mathbf{e}_y + E_{z0} e^{i(\omega t - kx)} \mathbf{e}_z \quad (20a)$$

$$\mathbf{H} = H_y \mathbf{e}_y + H_z \mathbf{e}_z = H_{y0} e^{i(\omega t - kx)} \mathbf{e}_y + H_{z0} e^{i(\omega t - kx)} \mathbf{e}_z. \quad (20b)$$

where  $E_{y0}$ ,  $E_{z0}$ ,  $H_{y0}$ ,  $H_{z0}$  are complex field amplitudes. The ratio of the coupled electric and magnetic field components is given by the previously defined intrinsic wave impedance



$$\eta = \frac{E_{y0}}{H_{z0}} = -\frac{E_{z0}}{H_{y0}}, \quad (21)$$

while the polarization of the wave is determined by the ratio between the two orthogonal electric field components

$$\frac{E_{y0}}{E_{z0}} = \frac{|E_{y0}|}{|E_{z0}|} e^{i(\phi_y - \phi_z)}. \quad (22)$$

Figure 8 illustrates the phase relationship between the electric field components of an electromagnetic plane wave propagating in the  $x$ -direction with (a) linear, (b) elliptical, and (c) circular polarization. In the case of linear polarization,  $\phi_y - \phi_z = 0^\circ$  or  $180^\circ$  and the polarization direction is determined by the relative strength of the two components. When the two components are identical in magnitude and  $\phi_y - \phi_z = +90^\circ$  or  $-90^\circ$ , the wave exhibits counter clockwise or clockwise circular polarization, respectively. If the two components are not exactly equal, the polarization becomes elliptically oriented with major and minor axes lying in the  $y$ - and  $z$ -directions. Generally, the wave exhibits elliptical polarization the direction and aspect ratio of which depends on the amplitude and phase of the components.

Figure 9 illustrates schematically the phenomenon of electromagnetic wave reflection and transmission at a plane boundary between two different media at normal incidence. Assuming

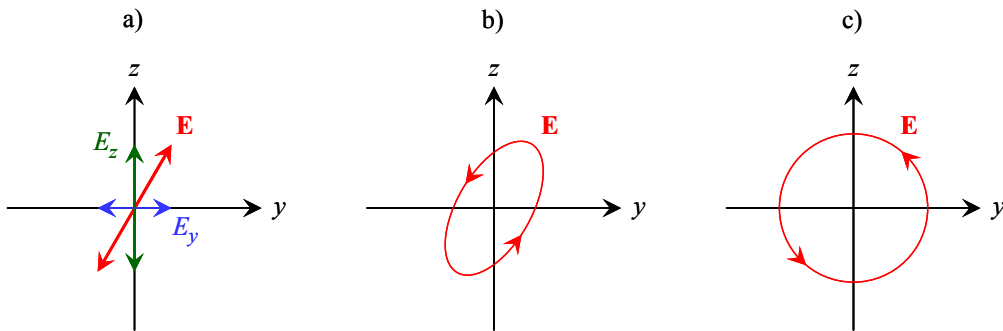


Figure 8 Phase relationship between the electric field components of an electromagnetic plane wave propagating in the  $x$ -direction with (a) linear, (b) elliptical, and (c) circular polarization.

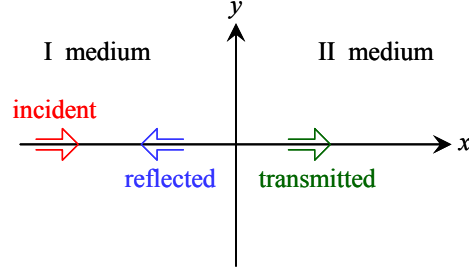


Figure 9. Electromagnetic wave reflection and transmission at a plane boundary between two different media at normal incidence.

that the electric component of the incident wave is polarized in the  $y$ -direction, the incident, reflected and transmitted electric and magnetic fields can be written as follows

$$\mathbf{E}_i = E_{i0} e^{i(\omega t - k_I x)} \mathbf{e}_y, \quad \mathbf{E}_r = E_{r0} e^{i(\omega t + k_I x)} \mathbf{e}_y, \quad \mathbf{E}_t = E_{t0} e^{i(\omega t - k_{II} x)} \mathbf{e}_y \quad (23)$$

$$\mathbf{H}_i = \frac{E_{i0}}{\eta_I} e^{i(\omega t - k_I x)} \mathbf{e}_z, \quad \mathbf{H}_r = -\frac{E_{r0}}{\eta_I} e^{i(\omega t + k_I x)} \mathbf{e}_z, \quad \mathbf{H}_t = \frac{E_{t0}}{\eta_{II}} e^{i(\omega t - k_{II} x)} \mathbf{e}_z. \quad (24)$$

The boundary conditions at  $x = 0$  require the continuity of the tangential electric and magnetic fields, i.e.,  $E_y(x = 0^-) = E_y(x = 0^+)$  and  $H_z(x = 0^-) = H_z(x = 0^+)$ , which can be further written as (without the common  $e^{i\omega t}$  term)

$$E_{i0} + E_{r0} = E_{t0} \quad (25)$$

$$H_{i0} + H_{r0} = H_{t0}, \quad (26)$$

or more conveniently expressed with the electric fields and the intrinsic impedances of the media

$$\frac{E_{i0}}{\eta_I} - \frac{E_{r0}}{\eta_I} = \frac{E_{t0}}{\eta_{II}}. \quad (27)$$

Equations (25) and (27) can be easily solved for the sought reflection  $R$  and transmission  $T$  coefficients as follows

$$R = \frac{E_{r0}}{E_{i0}} = \frac{\eta_{II} - \eta_I}{\eta_{II} + \eta_I} \quad (28)$$

$$T = \frac{E_{t0}}{E_{i0}} = \frac{2\eta_{II}}{\eta_{II} + \eta_I}. \quad (29)$$

In the special case of a plane interface separating a dielectric material  $\eta_I = \eta_0/n$  from a conducting one  $\eta_{II} = \sqrt{i\omega\mu/\sigma}$ ,  $\eta_I \gg |\eta_{II}|$  except at extremely high frequencies beyond the range of interest in electromagnetic NDE. Under such conditions, almost perfect reflection occurs with phase reversal, i.e.,  $R \approx -1$  and the transmitted wave is diffuse with a standard penetration depth of  $\delta = 1/\sqrt{\pi f \mu \sigma}$ .

For dynamic electromagnetic waves the electric and magnetic fields are coupled in both media according to their respective intrinsic wave impedances and propagate in the same wave direction with orthogonal polarizations with respect to the wave direction as well as each other. Under oblique incidence at a plane interface between dielectrics the refraction law applies to the common electromagnetic wave direction and is called Snell's law

$$\frac{\sin \theta_I}{c_I} = \frac{\sin \theta_{II}}{c_{II}}, \quad (30)$$

where  $c_I = 1/\sqrt{\mu_I \epsilon_I}$  and  $c_{II} = 1/\sqrt{\mu_{II} \epsilon_{II}}$  are the wave velocities in the two media. Of course, satisfying Snell's law is only a necessary but not satisfactory condition to comply with all the boundary conditions. For any direction of incidence, Snell's law defines the reflection and refraction angles of the secondary waves generated at the interface at a given angle of incidence while the amplitudes of these waves, i.e., the reflection and transmission coefficients, are determined by the boundary conditions, namely the continuity of the tangential electric and magnetic fields.

One of the most important phenomena in electromagnetic NDE is wave interaction with an interface separating a conducting medium from a dielectric (nonconducting) medium. Because

the electromagnetic wave becomes diffuse in the conductor, it exhibits an exponential decay controlled by the skin depth given in Eq. (19). Two versions of the skin effect are of particular importance in NDE. First, there is an axial skin effect that occurs when the diffuse wave in the conductor is normal to the surface as shown in Figure 10a. Both the electric field  $\mathbf{E} = E_0 F(x) e^{i\omega t} \mathbf{e}_y$  and the magnetic field  $\mathbf{H} = H_0 F(x) e^{i\omega t} \mathbf{e}_z$  will exhibit the same axial decay  $F(x) = e^{-x/\delta} e^{-ix/\delta}$  with depth. Figure 10b illustrates both the magnitude and real part of this depth profile. Although the dominant effect is the rapidly decreasing magnitude with depth, it is important to recognize that the phase also changes and at three times the standard penetration depth, where the magnitude is small but not entirely negligible (about 5% of its corresponding value on the surface) the phase becomes opposite relative to the surface and the real part is negative.

Second, there is a transverse skin effect that occurs when the diffuse wave in the conductor is tangential to the surface. As an example, let us consider the canonical problem an electric current  $I$  flowing through a cylindrical conductor rod of radius  $a$  as shown in Figure 11a. The electric current density is  $J_z(r) = J_{DC} F(r)$ , where  $J_{DC} = I/(\pi a^2)$  is the static uniform current density and  $F(r)$  is the radial profile given by

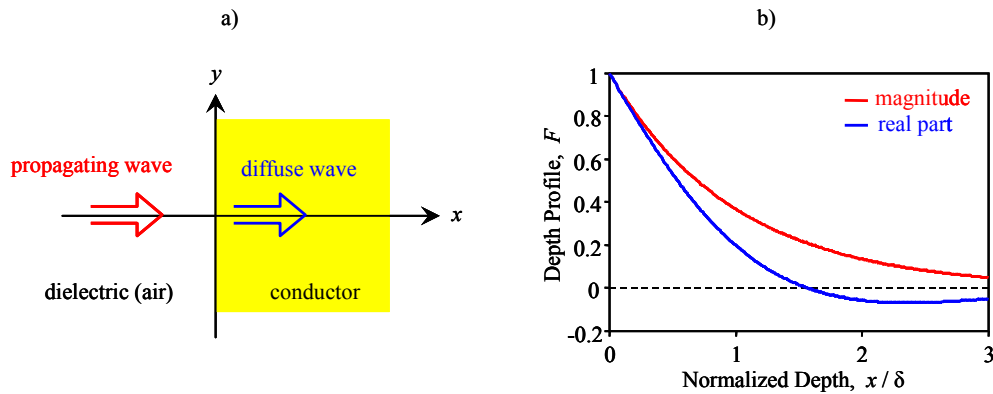


Figure 10 A schematic representation of the axial skin effect (a) and the normalized depth profile of the diffuse electromagnetic wave in the conductor (b).

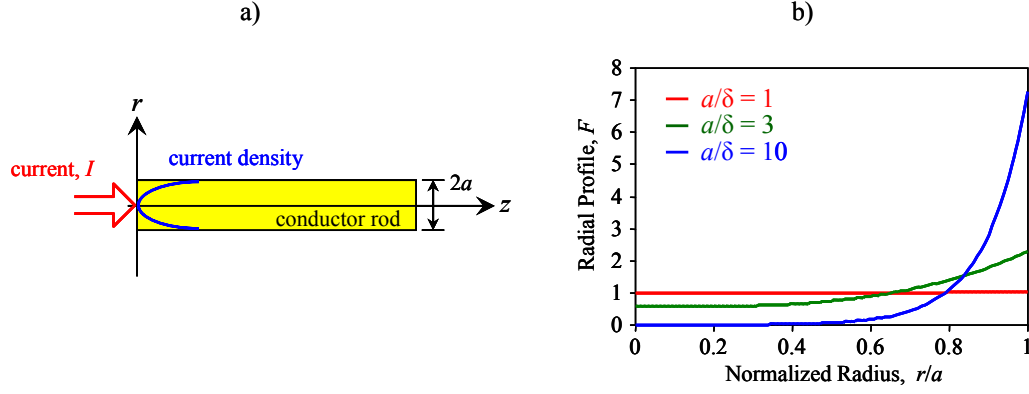


Figure 11 A schematic representation of the transverse skin effect (a) and the radial profile of the diffuse electromagnetic wave in the conductor rod (b).

$$F(r) = \frac{k a J_0(k r)}{2 J_1(k a)}, \quad (31)$$

where  $J_0$  and  $J_1$  are the zeroth- and first-order Bessel functions of the first kind, respectively [11]. At low frequencies ( $\delta \gg a$ ) the current distribution is essentially uniform and its magnitude asymptotically approaches its direct current (DC) asymptote  $J_{DC}$ . At high frequencies ( $\delta \ll a$ ) the current distribution asymptotically approaches one that exponentially decays with increasing depth below the surface with a penetration depth equal to  $\delta$ .

As the frequency increases the current distribution becomes more and more tightly squeezed to the surface while the total current remains the same, therefore the current density, and accordingly the axial electric field keeps increasing proportional to the square root of frequency. As a result, the resistance of the conducting rod over a length  $\ell$  also increases as illustrated in Figure 12 that shows the normalized resistance  $R/R_{DC}$  of a conducting cylindrical rod as a function of its normalized radius  $a/\delta$ . The complex electric impedance of the rod is  $Z = R + iX = R_{DC} F(a)$ , where  $R_{DC} = \ell / (\sigma \pi a^2)$  is the DC resistance and  $F(a)$  is the value of the previously defined radial profile at  $r = a$ . At sufficiently high frequencies, the resistance of the rod can be approximated as  $R = \ell / (\sigma 2 \pi a \delta)$  almost as if the current flowed uniformly in a

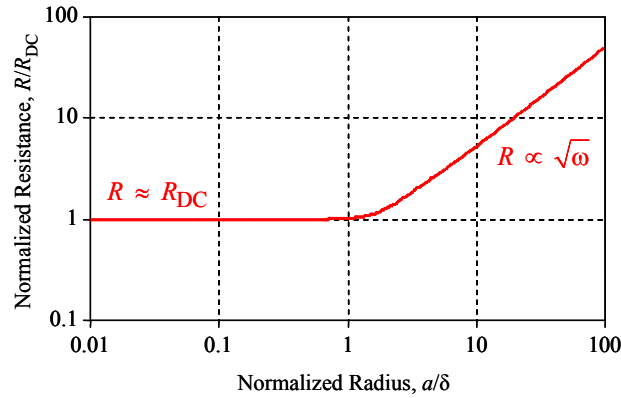


Figure 12 Normalized resistance of a cylindrical conducting rod as a function of its normalized radius.

skin layer of depth  $\delta$ . Of course, physically this is not the case, but this crude approximation of the transverse skin effect seems to be quite accurate over a large range of geometries [12].

## 2 Eddy Current Theory

Eddy current inspection is the most popular electromagnetic NDE method used in both field inspection and laboratory research [13-19]. Eddy currents are caused by electromagnetic induction in conducting materials when the test object is placed in the time-variable magnetic field of a probe coil. Although eddy currents behave very much like their galvanically coupled counterparts, the fact that they are inductively coupled offers the significant advantage of being non-contacting, though it also means that the generation efficiency decreases with frequency, which limits the lowest inspection frequency to typically around 100 Hz.

### 2.1 Eddy Current Method

Figure 13a shows a schematic diagram of eddy current inspection in its simplest form when the same coil that generates the eddy currents in the conducting specimen is also used as the sensor that detects the total magnetic flux which includes the contribution of the eddy currents flowing in the specimen. Figure 13b shows the counter-acting primary (excitation) and secondary (eddy)

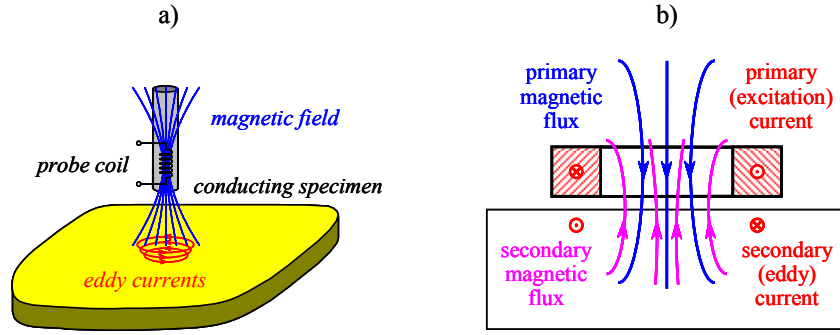


Figure 13 Schematic diagrams of (a) eddy current inspection and (b) the counter-acting primary and secondary currents and magnetic fluxes.

currents and magnetic fluxes in a schematic way.

According to Lenz's law, the induced current always flows in such a direction as to oppose the motion or change causing it. Therefore, the electric voltage  $V_p$  induced in the primary (probe) coil is

$$V_p = -N \frac{d}{dt} (\Phi_p - \Phi_s), \quad (32)$$

where  $\Phi_p = \mu N I_p \Lambda_p$  is the primary magnetic flux produced by the current flowing in the probe coil,  $\Phi_s = \mu I_s \Lambda_s$  is the secondary magnetic flux produced by the eddy current flowing in the specimen,  $N$  is the number of turns in the probe coil, and  $\Lambda_p$  and  $\Lambda_s$  are geometrical parameters determined by the size and shape of the coil, lift-off distance, and the penetration depth. The complex electric impedance  $V_p / I_p = Z_{\text{probe}}(\omega, \sigma, \mu, \ell, \dots)$  of the probe coil is a function of the inspection frequency  $\omega$ , the specimen's conductivity  $\sigma$  and permeability  $\mu$ , the lift-off distance  $\ell$  between the probe coil and the specimen, as well as numerous other parameters that affect the strength and distribution of the produced eddy currents such as the presence of surface-breaking or subsurface cracks.

Arguably, the simplest way to illustrate how changes in the secondary (eddy current) coil can influence the electric impedance of the primary (probe) coil is by considering the simple case of an air-core transformer formed by the two inductively coupled coils shown in Figure 14a. The quantity denoted by  $\Phi_{ij}$  ( $i, j = 1, 2$ ) represents the part of the magnetic flux generated by the current going through the  $i$ th coil that passes through the  $j$ th coil.

The voltages induced at the two ports can be written as follows

$$V_1 = N_1 \frac{d}{dt}(\Phi_{11} + \Phi_{12}), \quad (33a)$$

$$V_2 = N_2 \frac{d}{dt}(\Phi_{21} + \Phi_{22}). \quad (33b)$$

According to the Law of Reciprocity, the same fraction of the total flux generated by  $I_1$  passes through the second coil as the fraction of the total flux generated by  $I_2$  passes through the first coil, i.e.,

$$\frac{\Phi_{12}}{\Phi_{22}} = \frac{\Phi_{21}}{\Phi_{11}} = \kappa, \quad (34)$$

where  $\kappa$  is called the coupling coefficient. Figure 14b shows the simplified two-port network representation with open circuit self inductances  $L_{11}$  and  $L_{22}$  and mutual inductance  $L_{12}$ , where  $\Phi_{11} = I_1 L_{11} / N_1$ ,  $\Phi_{22} = I_2 L_{22} / N_2$ , and  $L_{12} = \kappa \sqrt{L_{11} L_{22}}$ , so that Eq. (33) can be re-written in a simplified matrix form as follows

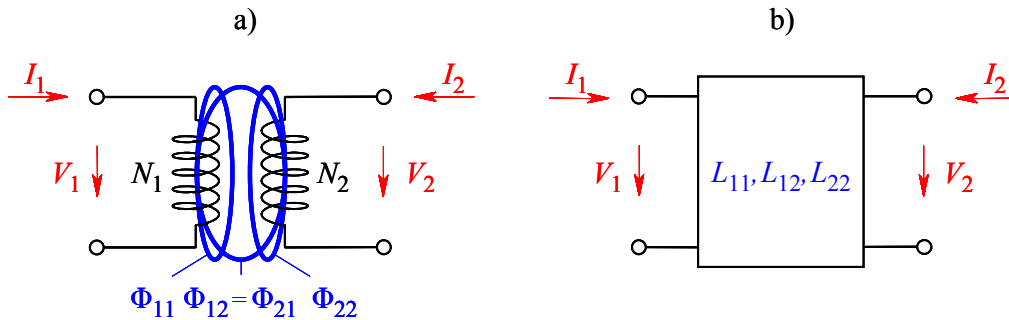


Figure 14 Schematic diagrams of (a) two inductively coupled coils and (b) the two-port equivalent network used to represent it.



$$\begin{bmatrix} V_1 \\ V_2 \end{bmatrix} = i\omega \begin{bmatrix} L_{11} & L_{12} \\ L_{21} & L_{22} \end{bmatrix} \begin{bmatrix} I_1 \\ I_2 \end{bmatrix}. \quad (35)$$

The complex impedance of the primary (probe) coil is defined as  $Z_{\text{coil}} = V_1 / I_1$  which is usually normalized to the reactance  $X_{\text{ref}} \approx \omega L_{11}$  of the probe coil with the secondary coil open ( $I_2 = 0$ ) so that  $Z_n = Z_{\text{coil}} / X_{\text{ref}}$ . Now, let us assume that the secondary coil is loaded by  $R_e$  representing the resistance of the eddy current loop so that  $V_2 = -I_2 R_e$ . Then, Eq. (35) can be readily solved to get the normalized input impedance

$$Z_n = R_n + iX_n = \kappa^2 \frac{\zeta}{1 + \zeta^2} + i(1 - \kappa^2 \frac{\zeta^2}{1 + \zeta^2}), \quad (36)$$

where  $\zeta = \omega L_{22} / R_e$  is the normalized frequency.

## 2.2 Impedance Diagrams

Eddy current instruments usually operate as impedance analyzers and display the measured probe coil resistance and reactance on the complex impedance plane. Accordingly, it is also customary to plot the calculated coil impedance as a function of relevant variables, such as frequency, conductivity, permeability, lift-off distance, crack size, etc, as an impedance diagram. As an example, let us consider the above calculated complex electric impedance of the probe coil as a function of the normalized frequency  $\zeta$  and coupling coefficient  $\kappa$ . It is clear from Eq. (36) that the real and imaginary parts of the complex impedance are not independent of each other since  $X_n = 1 - R_n \zeta$ . For a constant normalized frequency, i.e., when only the coupling coefficient (lift-off distance) changes, this is the equation of a straight line with a negative slope. For constant coupling, i.e., when only the normalized frequency (inspection frequency  $\times$  conductivity) changes

$$R_n^2 + \left( X_n - 1 + \frac{\kappa^2}{2} \right)^2 = \left( \frac{\kappa^2}{2} \right)^2, \quad (37)$$

which is the equation of a circle of radius  $\kappa^2/2$  with the center at  $R_{n0} = 0, X_{n0} = 1 - \kappa^2/2$ .

Figure 15 shows the impedance diagram of the above described coupled pair of coils with resistive loading ( $L_{22} = 3 \mu\text{F}, f = 1 \text{ MHz}$ ). As expected the lift-off trajectories (dashed lines) are straight lines while the conductivity  $\times$  frequency trajectories are semi-circles (except for the different horizontal and vertical scales). Each dot represents a 10% change in the loading resistance, therefore larger the separation between the dots, the larger the sensitivity of the coil impedance to changes in loading.

However, in practice the measurement error is not uniform in every direction in the complex impedance plane. The reason for this is that inevitable lift-off uncertainties due to spurious effects such as specimen curvature and roughness, vibrations, etc., make the lift-off distance highly variable, therefore the mechanical influence could be much stronger than the isotropic effect of random electric noise. Figure 16a illustrates schematically the excess measurement uncertainty parallel to the lift-off trajectory in the complex impedance plane. In order to suppress the large experimental uncertainty exhibited in the lift-off direction, the displayed impedance diagram is often rotated so that the lift-off trajectory is as close to

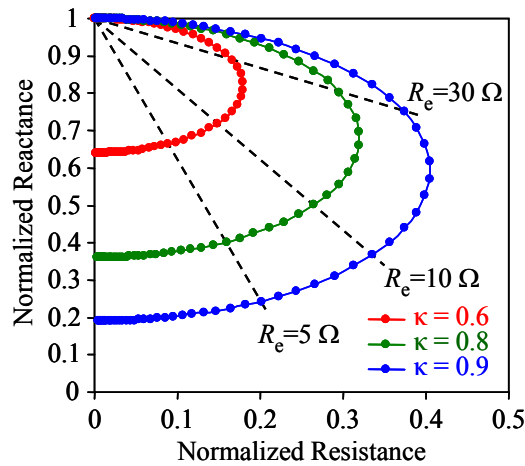


Figure 15 Impedance diagram of a coupled pair of coils with resistive loading.

horizontal as possible. Then, conductivity variations or the presence of cracks are best detected by measuring the vertical component only, i.e.,  $\Delta Z_n^\perp$  in Figure 16a instead of the otherwise larger magnitude of the total change  $|\Delta Z_n|$ .

The relative sensitivity of a sensor can be characterized by its gauge factor. For example, in the case of an ordinary strain gauge, the measured resistance change is  $\Delta R / R_0 = F \varepsilon$ , where  $R_0$  is the resistance of the unstrained gauge and  $\varepsilon = \Delta \ell / \ell$  is the strain to be measured. Similarly, the relative sensitivity of the inductively coupled sensor to resistance variations can be defined based on either the magnitude or normal component of the normalized impedance change

$$F_{\text{abs}} = \frac{|\Delta Z_n|}{\Delta R_e / R_e} \quad \text{and} \quad F_{\text{norm}} = \frac{\Delta Z_n^\perp}{\Delta R_e / R_e}. \quad (38)$$

As an example, Figure 16b shows the gauge factor of the above described inductive sensor to resistance variations at  $R_e = 10 \, \Omega$  reference resistance value. It is clear that the absolute gauge factor  $F_{\text{abs}}$  is slightly higher than the normal gauge factor  $F_{\text{norm}}$ , but of course the advantage of measurements normal to the lift-off trajectory lies not in higher sensitivity but rather in the significantly lower uncertainty level because of the more efficient suppression of lift-off

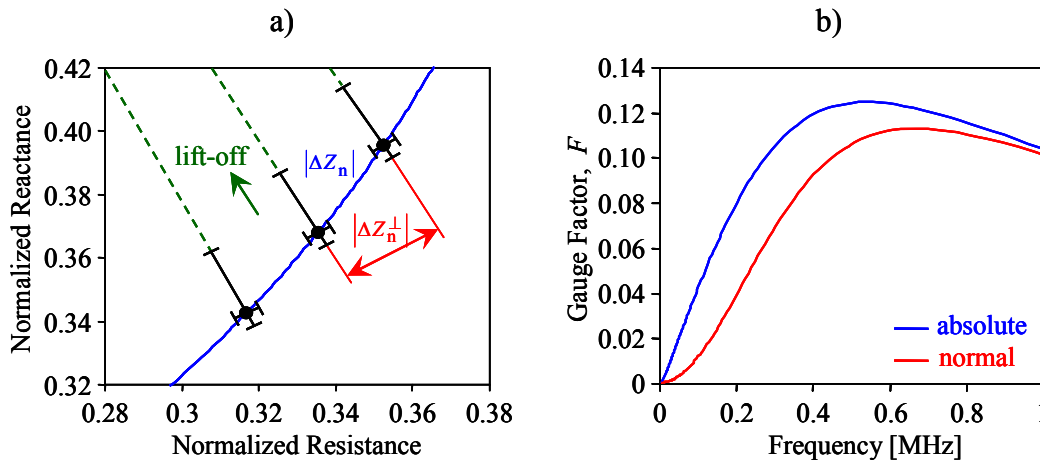


Figure 16 Schematic illustration of the (a) excess measurement uncertainty parallel to the lift-off trajectory in the complex impedance plane and (b) the relative sensitivity of the inductive sensor to resistance variations.

variations. It should be also mentioned that gauge factors around 0.1 are quite typical, therefore 1% accuracy in conductivity measurements requires better than 0.1% accuracy in electric impedance measurements. Fortunately, purely electric measurements tend to be highly accurate therefore this is usually not a problem.

### *2.3 Test Coil Impedance*

The main advantage of the above described simplistic 0-D model of eddy current inspection is that it yields simple explicit formulas for the probe coil impedance. It is helpful in illustrating the main features of impedance diagrams, but by neglecting the true dimensionality of practical problems it certainly oversimplifies real inspection applications. In reality, the eddy current generated in the specimen more or less follows the mirror image of the primary current of the probe, but both the penetration depth and lateral spread of the eddy current changes with frequency. As a result, the coupling coefficient becomes a function of the normalized frequency and the low-frequency top part of the otherwise semicircular conductivity  $\times$  frequency trajectory becomes flat and the high-frequency lower part bends downward and becomes almost straight. In addition, the lift-off trajectory also becomes bent, which makes it more difficult to suppress lift-off uncertainties by the above described horizontal/vertical separation after rotation.

The ideal linear lift-off curve is limited to 0-D cases when the current distribution cannot change, therefore the coupling coefficient cannot depend on frequency. One canonical problem that exhibits this feature is that of an infinitely long thin-wall solenoid [13]. Figure 17 illustrates the two simplest axisymmetric models used for eddy current inspection. The infinite solenoid encircling a solid cylinder or tube shown in Figure 17a is a one dimensional 1-D model that accounts for all radial changes including coating or cladding as well as the radial-dependence of the eddy current distribution in the specimen. One great advantage of this 1-D model over more

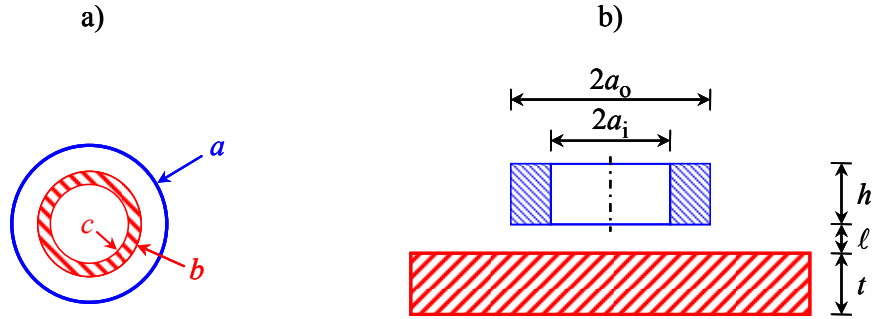


Figure 17 Simple axisymmetric models for (a) 1-D and (b) 2-D eddy current inspection.

complex 2-D and 3-D models is that it yields explicit analytical results [13]. In comparison, the more relevant 2-D model of an infinitely long cylindrical specimen with a co-axial coil of finite length [20] and the pancake coil model shown in Figure 17b properly account for both axial and radial changes at the expense of increased computational difficulties that require elaborate numerical integration [21, 22]. Finally, the presence of a surface-breaking or subsurface imperfection, such as a crack or inclusion, will destroy the remaining axial symmetry and necessitates the use of a fully 3-D numerical simulation based on boundary integration, volume integration, finite difference, finite element analysis, or other computational approaches [15, 18, 23-26].

As an example of the explicit analytical results yielded by the 1-D axisymmetric model, let us consider the normalized impedance of an infinite solenoid probe coil on a solid ( $c=0$ ) conducting cylinder [13]. The normalized coil impedance can be calculated as follows

$$Z_n = \frac{Z}{X_e} = i \{1 - \kappa^2 [1 - g(kb)]\}, \quad (39)$$

where  $g(\xi) = 2J_1(\xi)/[\xi J_0(\xi)]$  is the inverse of the previously introduced radial profile function  $F$  in Eq. (31) and  $\kappa = b/a$  is the so-called fill-factor that controls the maximum coupling between the probe coil and the eddy current loop and thereby corresponds to the lift-off distance

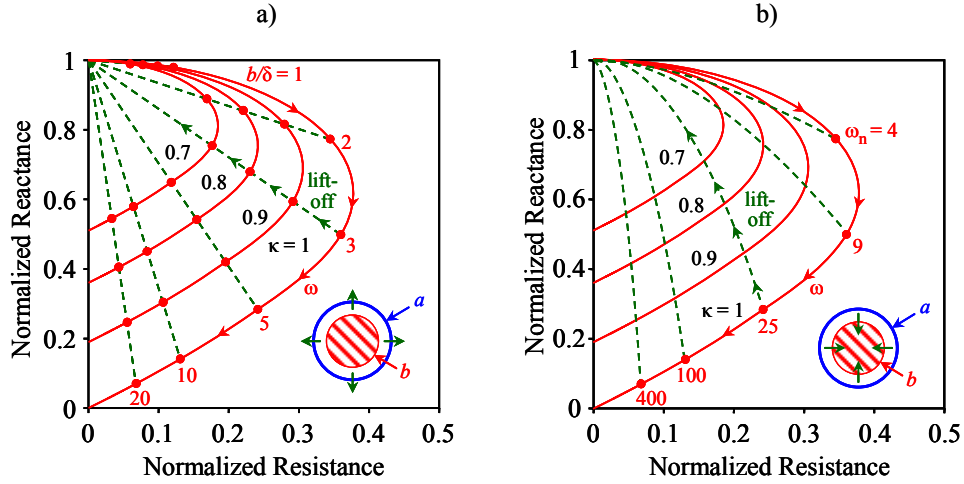


Figure 18 Normalized impedance diagrams of an infinite solenoid probe coil on a solid conducting cylinder with the fill-factor controlled by changing (a) the coil diameter and (b) the specimen diameter.

in the case of a pancake coil.

Figure 18 shows the normalized impedance diagrams of an infinite solenoid probe coil on a solid conducting cylinder with the fill-factor  $\kappa = b/a$  varied by changing (a) the coil diameter and (b) the specimen diameter. In the first case the lift-off is controlled via the  $\kappa = b/a$  fill-factor independent of the normalized frequency  $\xi = kb$ , therefore the lift of lines remain straight, i.e.,  $X_n = 1 - m R_n$ , where  $m$  is a function of the normalized frequency based on Eq. (39). However, in the more realistic second case when  $b$  is changing while the probe coil radius  $a$  remains constant, as the fill factor decreases so does the normalized frequency, therefore the lift-off curves become somewhat curved.

It is also instructional to consider how changing magnetic permeability affects the impedance diagram of the probe coil. Figure 19 shows the normalized impedance diagram of a magnetic rod calculated from the following modified version of Eq. (39)

$$Z_n = i \{1 - \kappa^2 [1 - \mu_r g(bk)]\}, \quad (40)$$

where  $\mu_r$  is the relative magnetic permeability of the conducting rod. The frequency was

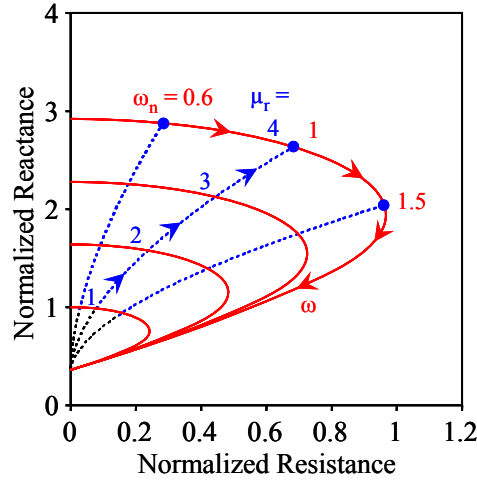


Figure 19 Normalized impedance diagrams of a magnetic rod for fill-factor  $\kappa = b/a = 0.8$ .

normalized as  $\omega_n = \omega/\omega_1$ , where the reference frequency was arbitrarily defined as  $\omega_1 = 1/(a^2\sigma\mu_r\mu_0)$ . In contrast to the effect of conductivity which decreases the reactance due to Lenz's law, increasing permeability increases rather than decreases the normalized reactance.

The same computational approach can be easily expanded to coated and clad rods and tubes and other multi-layered coaxial structures by introducing appropriate boundary condition at the interfaces [13]. Figure 20a illustrates schematically how the impedance diagram of thick-wall tubes is roughly limited by the border lines of solid cylinders and thin-wall tubes. Let us assume that the outer and inner radii of the tube are denoted by  $b$  and  $c$  so that  $d = b - c$  is the wall thickness. In the case of a very thin tube ( $d \ll \delta$ ) the eddy current distribution must be uniform throughout the thickness, therefore the problem becomes essentially 0-D and the conductivity  $\times$  frequency trajectory is circular like in the earlier shown simplistic model of coupled coils when the coupling coefficient is independent of frequency. In contrast, in the case of a solid rod, the coupling increases at higher frequencies, therefore the conductivity  $\times$  frequency trajectory bends downward and becomes almost straight. Furthermore, as it is illustrated by the positions of a low-conductivity ( $\sigma_1$ ) and high-conductivity ( $\sigma_2$ ) points, the

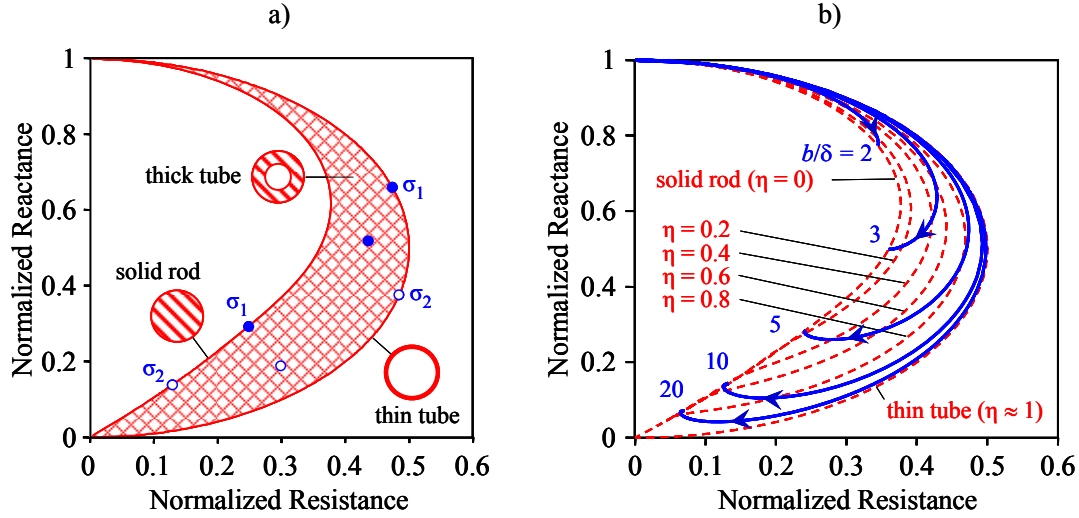


Figure 20 Schematic illustration of the limits of thick-wall tubes in the complex impedance plane (a) and impedance diagram of thick-wall tubes (b). The dashed lines represent various diameter ratios  $\eta = c/b$  while the solid lines correspond to various  $b/\delta$  ratios. In both cases the fill factor  $\kappa = b/a = 1$ .

locus of a given conductivity point on the thin-wall trajectory is lagging behind that of a thick tube because the penetration of the eddy current is limited not only by the standard penetration depth and the cylindrical symmetry, but also by the finite wall thickness.

Figure 20b shows the normalized impedance diagram for an infinitely long solenoid coil encircling a hollow conducting rod. The dotted lines represent frequency  $\times$  conductivity trajectories for constant inner-to-outer diameter ratios. The solid lines are wall thickness loci for constant  $b/\delta$  ratios, i.e., when the wall thickness variation is caused by changes in the inner radius. For very small wall thicknesses, all solid lines asymptotically approach the thin-tube circular asymptote. As the wall thickness increases, first the low-frequency part and later the high-frequency part of the curve switches over to the solid rod asymptote. It is interesting, that at high-frequency the thickness trajectories (solid lines) approach the solid rod asymptote in a small hook caused by the previously mentioned phase-lag of the eddy current components deep below the surface. These relatively weak currents are actually off-phase with the current on the



surface of the tube, therefore cutting them off slightly increases the apparent conductivity of the material.

As a further example, Figure 21 shows a schematic impedance diagram of an infinitely long solenoid coil encircling a brass-cladded copper rod and a copper-cladded brass rod (the cladding thickness is  $d = b - c$ ). Assuming a given inspection frequency, both solid brass and solid copper rods lie on the same conductivity master curve but at different locations since copper exhibits significantly higher electric conductivity than brass. This master curve corresponds to the eddy current depth distribution characteristic to homogeneous solid cylinders.

When a thin copper layer is deposited on a brass rod the eddy current gets stronger and its depth profile is more concentrated towards the surface, which increases the coupling coefficient and deforms the impedance diagram outward towards a more circular trajectory. Finally as the cladding thickness increases the overall conductivity becomes much higher than it was in brass and the impedance returns to the original master curve as the specimen appears apparently homogeneous again. When a thin brass layer is deposited on a copper rod the opposite happens as the eddy current gets weaker and its depth profile is more concentrated away from the surface,

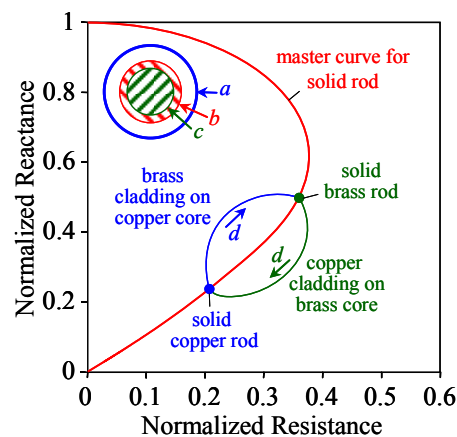


Figure 21 A schematic impedance diagram of an infinitely long solenoid coil encircling a brass-cladded copper rod and copper-cladded brass rod.

which decreases the coupling coefficient and deforms the impedance diagram inwards even further away from a circular trajectory. Finally as the cladding thickness increases the overall conductivity becomes much lower than it was in copper and the impedance returns to the original master curve as the specimen appears homogeneous again.

As we mentioned earlier, such 1-D models are very easy to use because they yield explicit closed-form analytical results while otherwise more relevant 2-D models generally do not facilitate closed-form solutions and require elaborate numerical integration. Still, in today's era of powerful computers, 2-D and even complex 3-D problems are relatively easily solved by numerical means. As a simple example, let us consider the cylindrical coil of rectangular cross section previously shown in Figure 17b. The complex electric impedance of such a pan-cake coil can be calculated as follows [21]

$$Z = \frac{i\omega\pi\mu_0 N^2}{h^2(a_o - a_i)^2} \int_0^\infty \frac{I^2(\alpha)}{\alpha^6} \left\{ 2(\alpha h + e^{-\alpha h} - 1) + [e^{-\alpha(h+\ell)} - e^{-\alpha\ell}]^2 R(\alpha) \right\} d\alpha, \quad (41a)$$

where  $a_i$  and  $a_o$  are the inner and outer radii, respectively,  $h$  is the height of the coil,  $N$  is the number of turns,  $\ell$  is the lift-off distance,  $\alpha$  is an integration parameter that is physically related to the radial wave number in the spatial-frequency decomposition of the coil's magnetic field,  $I$  is the following integral of the first-order Bessel function of the first kind  $J_1$

$$I(\alpha) = \int_{\alpha a_i}^{\alpha a_o} x J_1(x) dx, \quad (42b)$$

and  $R(\alpha)$  is a “reflection coefficient” that contains all the information about the specimen. In the simplest case of a homogeneous infinite half-space

$$R(\alpha) = \frac{\alpha\mu_r - \alpha_1}{\alpha\mu_r + \alpha_1}, \quad (42c)$$

where  $\mu_r$  is the relative permeability of the substrate and

$$\alpha_1^2 = \alpha^2 - k^2 = \alpha^2 + i\omega\mu_r\mu_0\sigma. \quad (43)$$

For a plate of finite thickness, for coated plates, or for any other multilayered structure  $R(\alpha)$  can be easily calculated by satisfying the relevant boundary conditions and, by repeated application of the same procedure, even continuous property variations can be modeled quite easily.

As a simple example, Figure 22a shows the normalized impedance diagram of a flat pancake probe coil for three different lift-off distances ( $a_o = 1$  mm,  $a_i = 0.5$  mm,  $h = 0.05$  mm,  $\ell = 0.1$  mm,  $\sigma = 8.7 \times 10^5$  S/m,  $\mu = \mu_0$ ). Although the general shape of the conductivity  $\times$  frequency and lift-off trajectories are quite similar to those previously derived from 1-D models, subtle changes in the curves contain additional information on the size and shape of the probe coil that was absent from the simpler case. This added capability is illustrated in Figure 22b showing the normal gauge factor of the same type of pancake coil for three different outer diameters keeping the ratio constant at  $a_o/a_i = 2$  while the other parameters are the same as before. According to the widely used rule of thumb, maximum impedance sensitivity for small conductivity variations is reached at an optimal inspection frequency  $f_M$  where the average coil

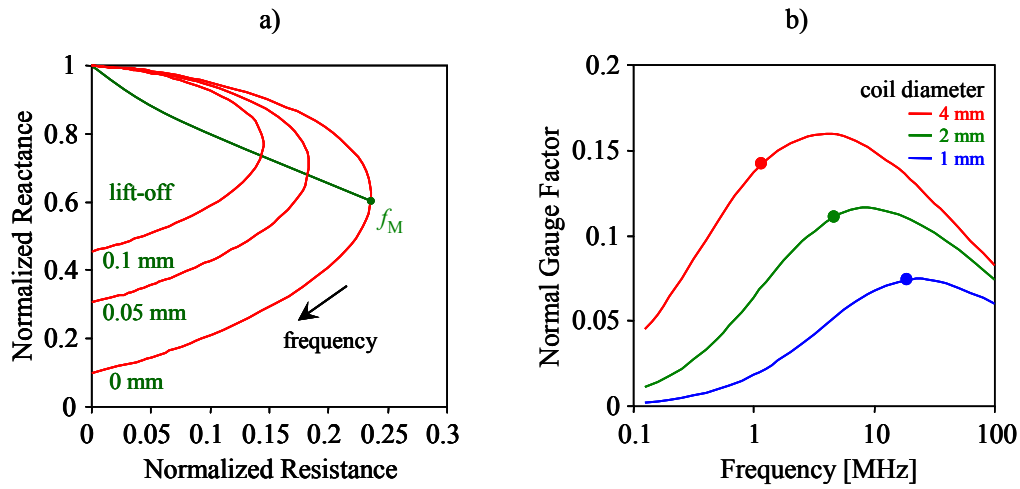


Figure 22 Normalized impedance diagram of a 2-mm-diameter flat pancake probe coil for three different lift-off distances (a) and the normal gauge factor as a function of inspection frequency for three different coil diameters (the symbols indicate the predicted optimal inspection frequency  $f_M$ ).

radius is roughly equal to the standard penetration depth  $\bar{a} = (a_o + a_i)/2 \approx \delta$ , which yields  $f_M = 1/(\pi \bar{a}^2 \sigma \mu)$ . The circular dots in Figure 22b indicate these approximate values of the optimal inspection frequency for the various coil diameters. Of course, if the other geometrical parameters ( $h$  and  $\ell$ ) had been changed proportionally the inner and outer diameters, the sensitivity curves would have been simply shifted and the relative position of  $f_M$  with respect to the actual peak would have remained the same.

In Section 3.2 we will consider more complicated inspection problems such as crack detection and sizing with pancake coils that require complete 3-D analysis. In that context, we will return to some of the above discussed issues and illustrate how state of the art computational methods can be used to solve such problems.

#### *2.4 Field Distributions*

The complex electric impedance of the probe coil is of primary importance in eddy current inspection because typically that is the only parameter we can measure (in some low-frequency applications the normal or tangential magnetic field above the surface is measured instead). However, it is also essential to have a good understanding of the magnetic field and, especially, the eddy current distribution in the specimen under test so that the operation, be it either flaw detection or materials characterization, could be optimized. In some simple 1-D cases such calculations might be done analytically, but in more realistic 2-D and 3-D simulations they require numerical solutions such as finite element (FE) analysis [27-31].

As we showed earlier, for a plane wave incident on a conducting half-space the standard penetration depth  $\delta$  actually gives the  $1/e$  skin depth of the exponentially decaying eddy current density, but for any finite-sized probe coil it is only a useful parameter which happens to be the upper limit for the axial penetration depth. As an example, Figure 23 shows computer

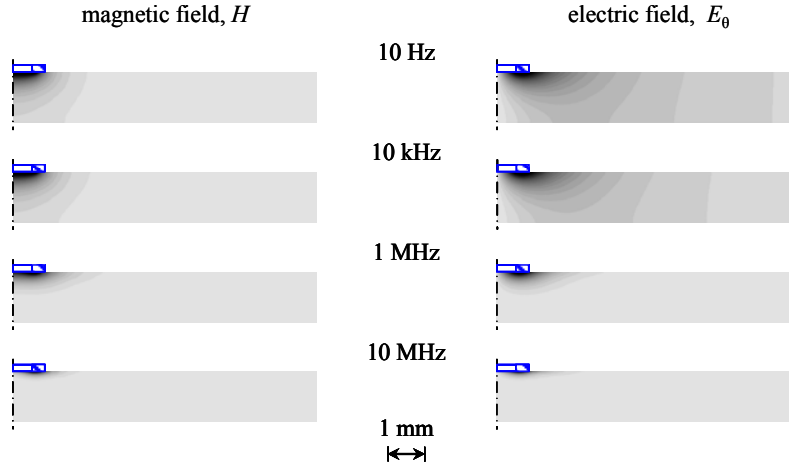


Figure 23 Computer simulations of the magnetic and electric fields produced by an air-core pancake probe coil in Ti-6Al-4V at four different frequencies ( $a_i = 0.5$  mm,  $a_o = 0.75$  mm,  $h = 2$  mm,  $\ell = 0$  mm,  $\sigma = 1$  %IACS,  $\mu = \mu_0$ ).

simulations of the magnetic and electric fields produced by an air-core pancake probe coil ( $a_i = 0.5$  mm,  $a_o = 0.75$  mm,  $h = 2$  mm,  $\ell = 0$  mm) in Ti-6Al-4V ( $\sigma = 1$  %IACS,  $\mu = \mu_0$ ) at four different frequencies [32]. The magnetic field  $\mathbf{H}$  has both axial and radial components, therefore only the magnitude  $H$  is plotted. The electric field  $\mathbf{E}$  exhibits only azimuthal component  $E_\theta$  which is simply proportional to the eddy current density.

Whenever the standard penetration depth is very large with respect to the dimensions of the coil the magnetic field is essentially unaffected by the flow of eddy currents in the specimen and can be approximated by the magnetic field produced by the coil far away from the conducting half-space. In this frequency range (up to about 10 kHz or  $\delta \approx 3.4$  mm in our case) the eddy current distribution is also independent of frequency while its absolute density increases proportionally to frequency. Whenever the standard penetration depth is small with respect to the dimensions of the coil the magnetic field is essentially eliminated by the flow of eddy currents in the specimen below a certain skin depth which approaches the standard penetration depth. In this frequency range (above approximately 1 MHz or  $\delta \approx 0.34$  mm in our case) the

eddy current distribution is limited to a shallow layer determined by the standard penetration depth.

Figure 24a shows the axial penetration depth versus frequency curve for the same 1.5-mm-diameter pancake coil in Ti-6Al-4V [32]. The solid line represents the numerical results calculated by finite element (FE) simulation and the dashed line is the plane wave asymptote calculated from the standard penetration depth. The axial penetration depth  $\delta_a$  was calculated from the eddy current intensity directly under the coil at its middle ( $r = \bar{a}$ ). This figure demonstrates the fundamental difference between the true axial penetration depth of a finite-diameter coil and the standard penetration depth at low frequencies, which was first pointed out by Mottl [33] and later further investigated by Stucky and Lord [34].

The radial penetration depth of eddy currents generated by a finite-diameter probe coil can be determined in a similar way by analyzing the same set of FE data. The effective radius of the eddy current spread  $a_s$  is measured from the axis of the coil to the point on the surface of the conducting half-space where the eddy current density drops to  $1/e$  relative to its maximum, which is directly under the middle of the coil. At low and high frequencies, the radial spread asymptotically approaches  $a_1 \approx 1.8$  mm and  $a_2 \approx 0.9$  mm. These parameters are sensitive to the

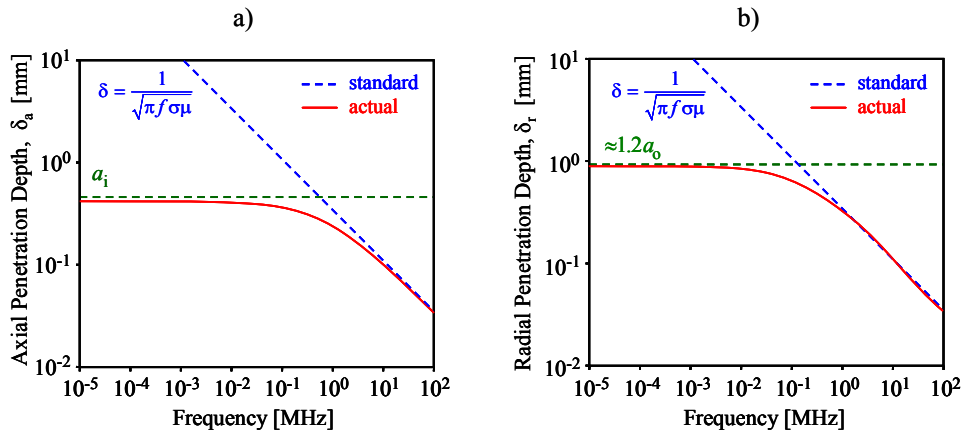


Figure 24 Axial (a) and radial (b) penetration depths versus frequency for the same pancake coil in Ti-6Al-4V.

shape of the coil (both inside-to-outside diameter and diameter-to-height ratios) but  $a_0 < a_2 < a_1$ . The radial “penetration depth” can be defined as  $\delta_r = a_s - a_2$ , which is plotted in Figure 24b as a function of frequency for the same 1.5-mm-diameter pancake coil in titanium [32]. Although this parameter clearly depends on the shape of the probe coil, we can still conclude that at high frequencies the radial penetration depth can be more or less accurately approximated by the standard penetration depth, which depends only on the material properties and frequency. As a rule of thumb, at low frequencies, when the magnetic field generated by the probe coil is not affected significantly by the presence of eddy currents in the specimen, the effective radius of the eddy current loop is  $a_s \approx 2.4 a_0$  and drops to about  $1.2 a_0$  at very high frequencies when  $\delta \ll a_0$ .

### 3 Eddy Current NDE

The goal of this section is to introduce the reader to the technical foundation of eddy current NDE. First, the most popular inspection techniques will be reviewed including near-field and remote-field inspection, single-frequency, multiple-frequency, pulsed eddy current techniques, and nonlinear inspection. The basics of instrumentation will be also discussed, including probe coil configurations and eddy current array transducers. The second part of this section focuses on the most common eddy current NDE applications, including conductivity, permeability, metal thickness, and coating thickness measurements and flaw detection and characterization. Finally, quantitative eddy current materials characterization will be illustrated through a few examples including anisotropic texture, grain structure, hardness, and near-surface residual stress assessment.

#### 3.1 Eddy Current Inspection Techniques

Eddy current inspection can be classified as near-field or far-field depending on whether the

inspection is limited to the range of the primary magnetic field or not. According to Lenz's law, eddy currents always flow in such a direction that they generate secondary magnetic fields that oppose, i.e., weaken, the primary magnetic field. The penetration depth of the combined magnetic field, and therefore also that of the induced eddy current distribution, is less than the range of the undisturbed primary magnetic field generated by the probe coil in the first place, as it was discussed at the end of the previous section. However, the near-field electromagnetic perturbation also gives rise to a diffuse electromagnetic wave that can extend well beyond the range of the undisturbed primary magnetic field, especially in ferromagnetic materials of favorable geometry such as pipes, which is called far-field inspection.

Figure 25 shows the most typical absolute eddy current probe configurations for near-field inspection. The most often used single-coil probe has limited sensitivity because the probe coil impedance is usually only weakly perturbed by variations in material properties and/or the presence of flaws. Better sensitivity and thermal stability can be achieved using “reflection-type” probes that contain separate driving (send) and a sensing (pickup) coils. This arrangement is less sensitive to intrinsic thermal variations in the measured impedance since the measured

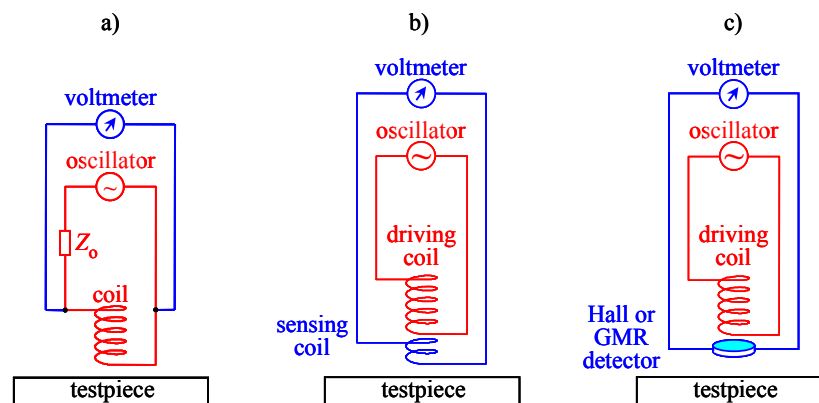


Figure 25 Typical absolute eddy current probe configurations for near-field inspection, namely (a) single-coil probe, (b) reflection-type (send-receive or driver-pickup) probe with separate sensing coil and (c) solid-state detector pickup.



complex mutual inductance is not influenced by the changing resistance of the coil wire. Since the voltage induced in a coil is proportional to the rate of change of the total magnetic flux crossing the coil rather than to its absolute value, sensing with a Hall detector or a Giant Magnetoresistive (GMR) sensor offers great sensitivity benefits at low inspection frequencies.

Absolute probes measure the complex impedance of the coil at one given location in order to characterize the specimen under test. This is true even though most absolute probes include a second identical “dummy” coil inside the casing that is not coupled magnetically to either the main coil or the specimen. By measuring essentially the impedance difference between the two coils in a bridge configuration, this simple technique offers improved thermal stability and sensitivity with respect to absolute probes containing a single active coil only. In comparison, differential eddy current probes measure the difference between the complex impedances of two coils coupled to the specimen under test at two different locations and possibly at two different orientation. Figure 26 shows typical differential eddy current probe configurations with (a) parallel, (b) coaxial, and (c) orthogonal coils. The most often used parallel configuration offers good rejection of spurious material variations in order to reach better flaw detectability, while the coaxial configuration does the same during the inspection of long bore holes, tubes, rods, wires, etc., both inside and outside depending on the application. The orthogonal arrangement is used in special cases when near-surface flaws can be best detected by measuring the changing difference between tangential and normal coil orientations.

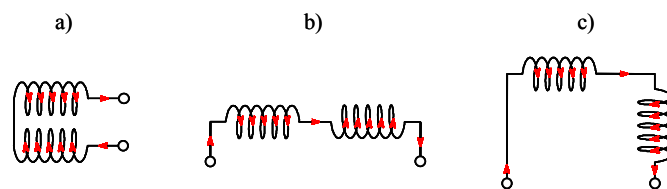


Figure 26 Differential eddy current probe configurations with (a) parallel, (b) coaxial, and (c) orthogonal coils.

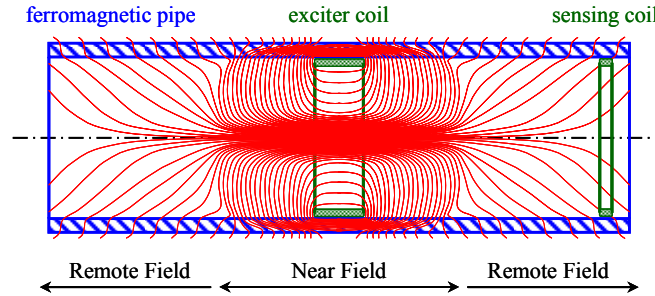


Figure 27 A schematic diagram of remote-field eddy current inspection.

In contrast to the conventional near-field eddy current inspection, remote-field electromagnetic inspection is based on the diffuse electromagnetic wave “propagating” or spreading beyond the range of the primary magnetic field [35-39]. Figure 27 shows a schematic diagram of remote-field eddy current inspection in a ferromagnetic pipe. Low-frequency operation (10-100 Hz) allows the inspection of pipes and tubes from the inside based on through-wall transmission of the electromagnetic field. Exponentially decaying eddy currents propagate mainly on the outer surface.

Figure 28 shows a schematic diagram of the decaying magnetic field in remote-field eddy current inspection. In the near-field region, the field rapidly decays until a transition region is reached. Beyond this point, the decay is strictly exponential with an attenuation coefficient equal to the inverse of the standard penetration depth  $\delta$ . The diffuse magnetic field leaks on both the outside and the inside of the pipe and can be picked up by a sensing coil or an array of solid-state

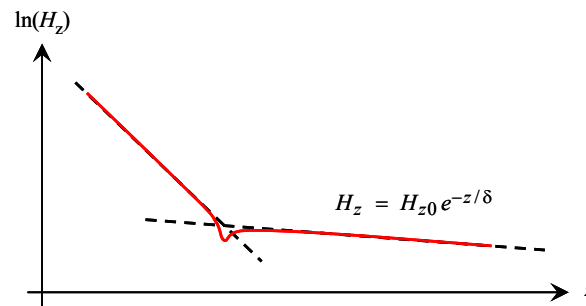


Figure 28 A schematic diagram of the exponentially decaying magnetic field in remote-field eddy current inspection.

magnetic sensors. The through-wall nature of the technique allows the detection of both external and internal defects with either inside or outside sensing.

Figure 29 illustrates the main driving modes used in eddy current inspection. Most applications rely on continuous single-frequency excitation, as shown in Figure 29a. When combined with phase-sensitive detection, this approach offers the best possible signal-to-noise ratio. However, single-frequency measurements can offer only limited information on flaws and material properties and exhibit imperfect suppression of spurious lift-off variations, therefore must be often used in swept-frequency mode that is rather time consuming.

It is more convenient to conduct multiple-frequency measurements simultaneously, or at least quasi-simultaneously using multiplexing. In quasi-simultaneous time-multiplexed mode multiple, typically two to eight, tone burst signals are mixed in a time sharing mode as shown in Figure 29b. The signal-to-noise ratio is necessarily lower than in continuous single-frequency mode of operation because of the wider measurement bandwidth and lower integration time, but this drawback is compensated by the convenience of essentially simultaneous multiple-frequency

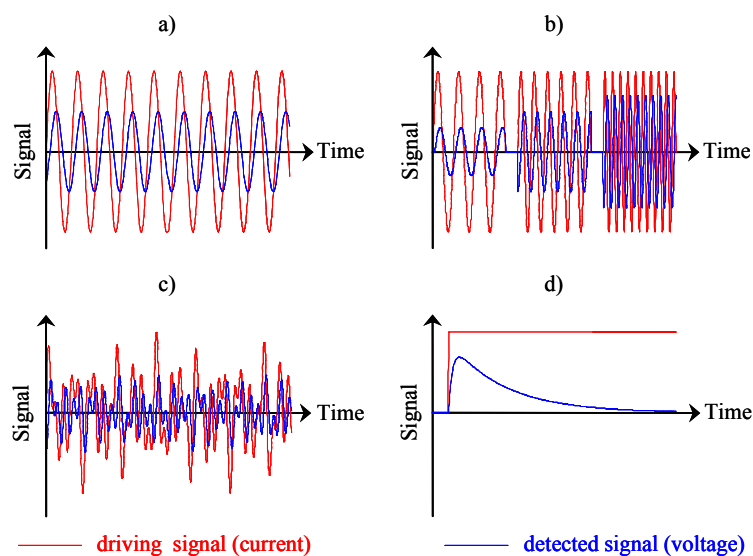


Figure 29 Main driving modes in eddy current inspection: (a) single-frequency, (b) time-multiplexed multiple-frequency, (c) frequency-multiplexed multiple-frequency, and (c) pulsed.

data acquisition. In simultaneous continuous frequency-multiplexed mode numerous continuous harmonic waveforms of different frequencies are mixed as shown in Figure 29c. This method exploits the very high frequency selectivity of lock-in amplifiers used as phase-sensitive detectors to separate the various frequency components.

Pulsed eddy current techniques offer a broadband impulse response somewhat similar to ultrasonic A-scans as shown in Figure 29d [40]. Naturally, the signal-to-noise ratio leaves much to be desired since the available excitation energy is continuously distributed over a wide frequency range, therefore extensive time averaging over repeated excitations might be necessary. Since the impulse function rapidly decays with time, the signal-to-noise ratio gets worse and worse as time progresses. One of the main advantages of pulsed eddy current inspection is that the impulse response can be directly interpreted in terms of penetration depth. The square of the standard diffusion length  $\ell_D^2 \approx \tau_D / (\sigma\mu)$  is proportional to the diffusion time  $\tau_D$  [41]. This effect is analogous to the well-known relationship between the standard penetration depth  $\delta^2 = 1/(\pi f \sigma\mu)$  and the inspection frequency  $f$  in conventional continuous single-frequency eddy current inspection. Just like the previously introduced standard penetration depth  $\delta$ , the standard diffusion length  $\ell_D$  is also valid only approximately when the probe coil diameter is very large.

The eddy current impulse shape can be determined by analytical means for finite-size coils and various excitation types [42]. Ultimately, pulsed eddy current (PEC) inspection yields the same type of information as conventional swept frequency eddy current (SFEC) inspection though various operational parameters are optimized in a different way [43]. For example, spurious lift-off variations can be relatively easily suppressed in SFEC at each frequency in the previously described way by introducing an appropriate phase rotation in the complex impedance

plane that aligns the lift-off trajectory horizontally and assures that the remaining vertical component of the impedance variation is essentially immune to lift-off uncertainties. This method does not have a direct analog in PEC, though it has been observed that the transient responses of semi-infinite half-spaces of different conductivity pass through a common point regardless of the lift-off value, which can be exploited for limited lift-off suppression [44].

In all the above described linear modes of operation the frequency content of the measured voltage  $V(f)$  was assumed to be linearly related to the spectral content of the driving current  $I(f)$  through the complex impedance function of the eddy current probe  $Z(f)$  via  $V(f) = Z(f) I(f)$ , where  $Z(f)$  contained the sought information about the specimen under tests. In the case of ferromagnetic specimens the relationship between the driving current and measured voltage is not necessarily linear because of the nonlinear and hysteretic relationship between the magnetic field  $H$  and the magnetic flux density  $B$  as illustrated in Figure 30a. In the presence of such nonlinearity, a purely harmonic driving current produces a distorted voltage as shown in Figure 30b that contains higher harmonics (integer multiples) of the fundamental harmonic. A recently developed eddy current method called nonlinear harmonic analysis exploits this phenomenon to detect and quantitatively characterize changes specifically in ferromagnetic phases, such as ferrite or martensite, in steels that are typically highly susceptible to prevailing residual stresses

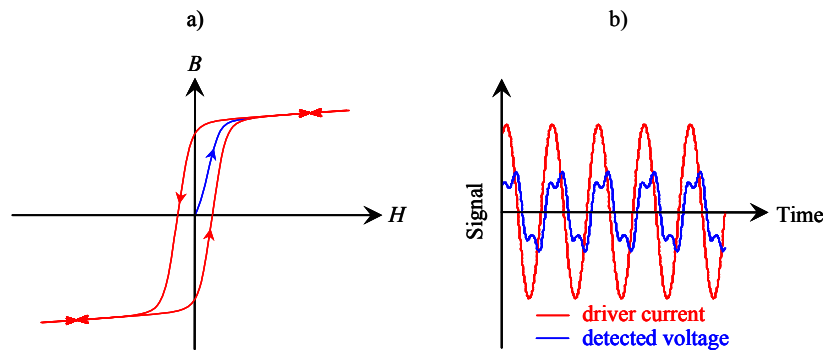


Figure 30 Schematic representations of (a) the nonlinear and hysteretic magnetization curve of materials containing ferromagnetic phases such as ferrite or martensite and (b) the principle of nonlinear harmonic analysis.

and prior plastic deformation, precipitation formation, and other subtle microstructural changes [45-47].

Figure 31 shows a schematic block diagram of a typical single-frequency eddy current instrument. An oscillator drives the measurement bridge through a driver amplifier at adjustable excitation levels of usually 10 V or less. The bridge is built of two identical driver impedances (usually resistors) and can accommodate either a differential coil or a single active coil combined with an identical dummy coil as described above. The output of the differential preamplifier is measured by a phase-sensitive lock-in amplifier that consists of a 90° phase shifter and two analog mixers followed by low-pass filters. The output signals of these filters are then digitized by an A/D converter and digitally processed for display and storage. State of the art instrumentation often starts with digitizing the signal immediately following the preamplifier and implements the phase sensitive detection via digital signal processing. The same configuration can be also used for nonlinear harmonic analysis with the exception that the lock-in amplifier is synchronized to run at the second or third harmonic of the inspection frequency as needed.

Conventional eddy current imaging with a single probe coil necessitates 2D mechanical scanning of the surface. Eddy current array (ECA) technology can achieve electronic scanning by using multiple driving and sensing eddy current coils which are placed side by side in the

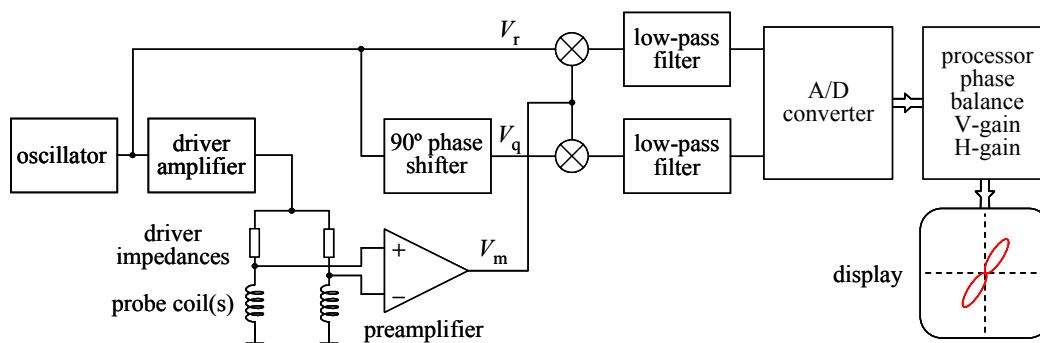


Figure 31 A schematic block diagram of a typical single-frequency eddy current instrument.

same probe assembly [48-54]. Each individual eddy current coil in the probe array produces a signal amplitude and phase determined by the structure directly below it. This data is referenced to an encoded position and time and can be presented graphically as a C-scan image.

Figure 32 shows an example of an eddy current line array with staggered elements to eliminate otherwise inevitable dead zones between neighboring coils. Such line arrays are electronically scanned in the width direction, but still require mechanical scanning in the normal direction to produce 2D images of the test object. Electronic scanning in the width direction offers numerous advantages such as significantly increased overall inspection speed, the ability to scan larger areas in a single pass while maintaining high resolution, less need for complex robotics to move the probe, etc. ECAs can be readily adapted to most conventional eddy current flaw detection applications. Complex shapes can be inspected using probes customized to the profile of the part being inspected and using flexible carrier foils that conform to the surface. Numerous designs are commercially available to detect defects such as surface cracks and pitting as well as subsurface defects like cracks in multilayer structures and corrosion loss.

### *3.2 Eddy Current Applications*

This section briefly reviews the basic principles of the most popular eddy current inspection methods including conductivity, permeability, metal thickness, and coating thickness measurements, depth profiling, and flaw detection.

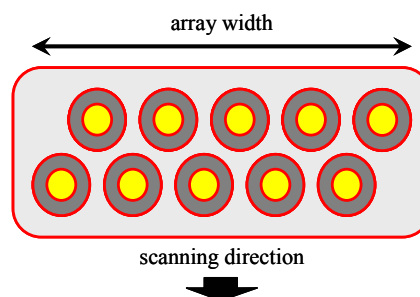


Figure 32 A schematic representation of an eddy current line array transducer.

### 3.2.1 Conductivity

The two physical parameters that directly affect the eddy current response of conducting materials are electric conductivity and magnetic permeability. However, most conductors are essentially nonmagnetic ( $\mu_r \cong 1$ ) therefore their eddy current response is determined solely by their conductivity. Assuming that the specimen is homogeneous and large enough to avoid thickness and edge effects at a given inspection frequency, all materials will lie on the same conductivity master curve previously discussed and their position on this curve can be used to determine their electric conductivity. Figure 33 illustrates schematically the conductivity loci of various metals in the complex impedance plane at a constant inspection frequency. Increasing conductivity corresponds to a clockwise movement along the conductivity trajectory, i.e., among the selected metals Ti-6Al-4V and pure Copper exhibit the lowest and highest conductivity values, respectively. Of course the electric conductivity of the material is a very sensitive function of its alloy content and state of microstructure that depends on its thermo-mechanical processing during manufacturing as well as on subsequent environmentally-assisted and service-related subtle changes.

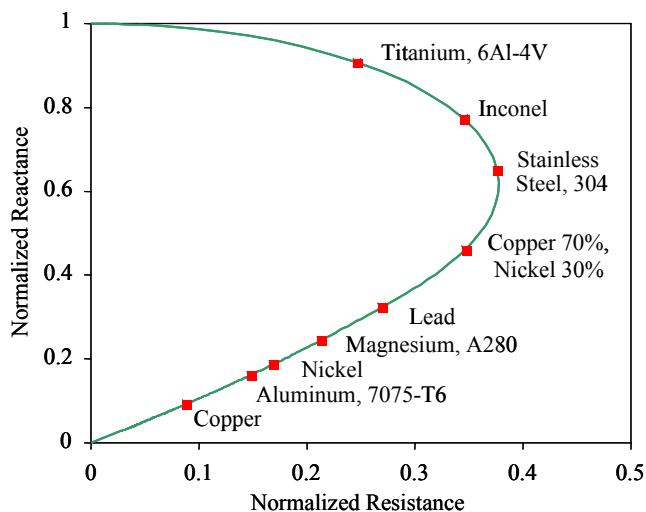


Figure 33 Conductivity loci of various metals in the complex impedance plane at a constant inspection frequency.



The high susceptibility of electric conductivity to so many microstructural state variables translates into high sensitivity and low selectivity for any given material change that renders absolute conductivity measurements rather useless for the purposes of nondestructive materials characterization. Figure 34 illustrates this point through the example of typical electric conductivity variations in different high-strength aluminum alloys of widely used heat treatments or so-called tempers. The absolute electric conductivity is expressed as a percentage of the International Annealed Copper Standard (%IACS), which is  $\sigma_{\text{IACS}} = 5.8 \times 10^7 \text{ } \Omega^{-1}\text{m}^{-1}$ , ( $\rho_{\text{IACS}} = 1.7241 \times 10^{-8} \text{ } \Omega\text{m}$ ) at 20 °C. The conductivity ranges from 30 to 50 %IACS and is more sensitive to temper than to alloying content. Eddy current instruments dedicated entirely to conductivity measurements might be programmed to estimate the specimen's conductivity from the complex probe impedance measured at a particular inspection frequency and calibration data saved in the instrument's memory or in an auxiliary memory chip of smart probes that is automatically recognized by the instrument.

General purpose instruments can be used for the same purpose only after proper calibration. Most instruments use a four-point linear interpolation procedure to determine the apparent eddy

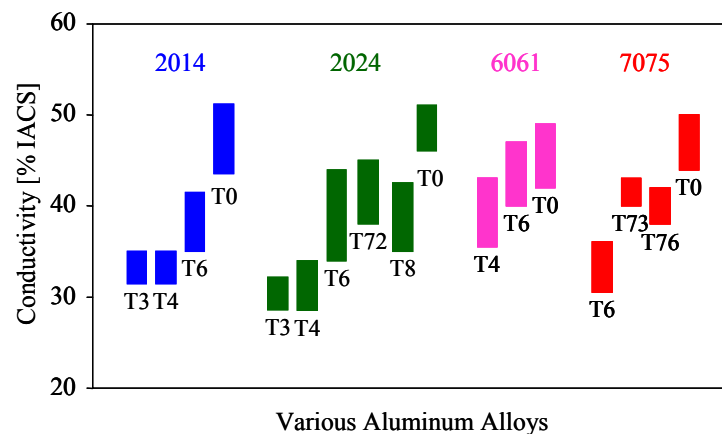


Figure 34 Examples of typical electric conductivity variations in different high-strength aluminum alloys of standardized heat treatments.

current conductivity of metals. Figure 35 shows a schematic representation of the eddy current probe coil impedance in the complex plane and the concept of four-point linear interpolation procedure for assessment of the apparent eddy current conductivity. Four reference points are measured on two appropriate calibration blocks with ( $\ell = s$ ) and without ( $\ell = 0$ ) a polymer foil of thickness  $s$  between the probe coil and the specimens. For small conductivity variations sufficiently accurate results can be achieved by choosing two calibration blocks that closely bracket the conductivity range of interest. Then, the unknown apparent eddy current conductivity (AECC) and apparent eddy current lift-off (AECL) can be calculated from the complex coil impedance produced by the actual specimen using simple linear interpolation method [55].

Of course linear interpolation severely limits the conductivity and lift-off range over which this simple technique can be used successfully. The main difficulty is caused by the curvature of the lift-off trajectory, which is illustrated schematically in Figure 36. At low frequencies the curvature of the lift-off trajectory is usually positive due to inductive effects. In contrast, the curvature becomes negative at high inspection frequencies where the effects of the self- and

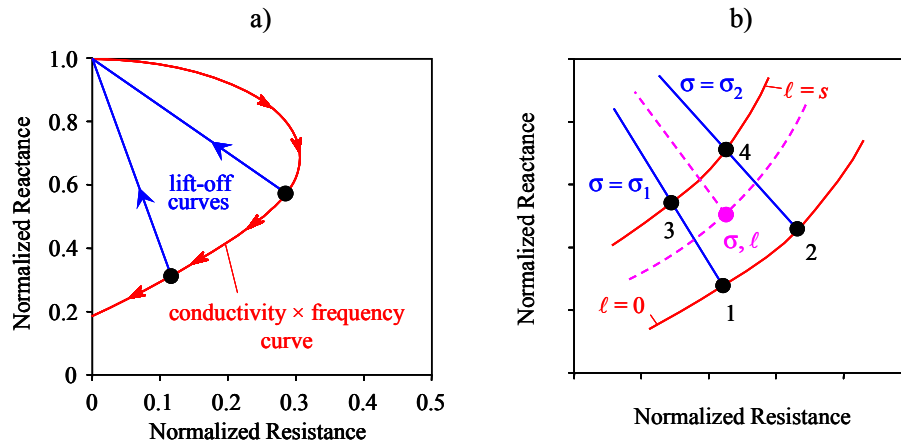


Figure 35 A schematic representation of the eddy current probe coil impedance in the complex plane (a) and the concept of four-point linear interpolation procedure for assessment of the apparent eddy current conductivity.

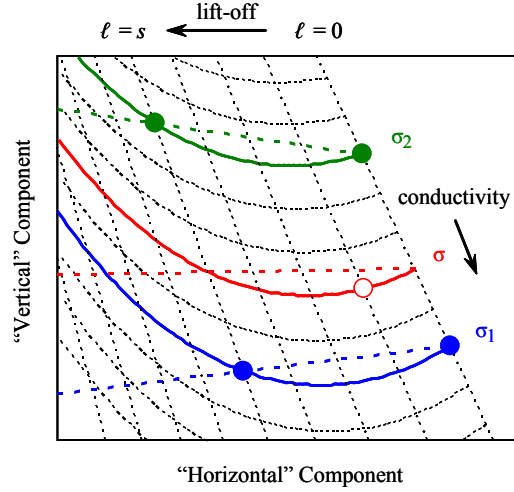


Figure 36 Typical lift-off trajectory with positive curvature in the rotated impedance plane.

stray-capacitance of the probe coil become perceivable [56]. In high-precision conductivity measurements efficient suppression of lift-off variations is of the utmost importance. Suppression can be improved by more precise quadratic interpolation after separately measuring the average curvature of the lift-off trajectory in the conductivity range of interest as a function of frequency. Regardless of how the interpolation is implemented, AECC and AECL represent the conductivity and lift-off of a hypothetical perfectly homogeneous conducting half-space that would produce exactly the same complex coil impedance as the specimen at a given frequency.

The main advantage of this approach is that it effectively eliminates the influence of the measurement system on the actually measured coil impedance, therefore AECC spectra taken with different equipments and different probe coils can be directly compared. To illustrate the robustness of this instrument calibration method, Figure 37 shows the AECC spectra measured by four different commercially available instruments (Nortec 2000S, Agilent 4294A, Stanford Research SR844, and UniWest US-450) on three IN718 specimens of different shot peening intensities [57]. In the overlapping frequency ranges the agreement between the AECC spectra obtained by different instruments is within the respective estimated error of each instrument.

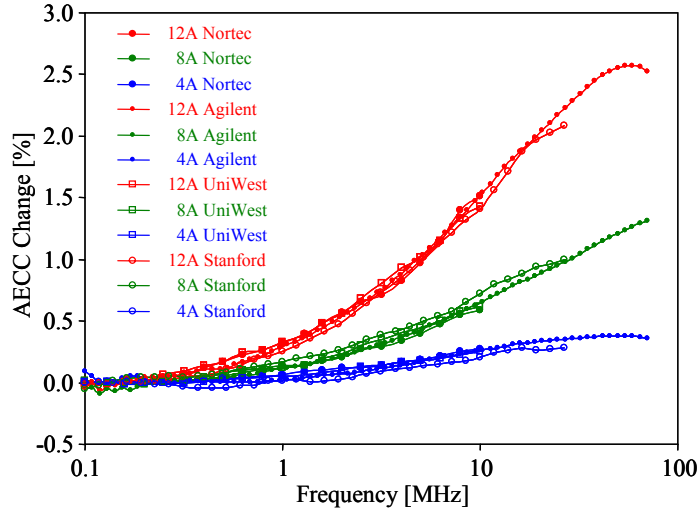


Figure 37 AECC change measured by four different instruments (Nortec 2000S, Agilent 4294A, Stanford Research SR844, and UniWest US-450) on three IN718 specimens of different peening intensities.

Of course, true physical quantities do not depend on the way they are measured. However, eddy current conductivity measurements are inherently susceptible to influence by the measurement system because of the complex relationship between the true material parameter, e.g., the depth-dependent electric conductivity in this case, and the measured physical parameter, i.e., the frequency-dependent AECC. It should be emphasized that the intrinsic electric conductivity of the material depends on depth rather than on frequency. Later in this section we are going to discuss how such frequency-dependent AECC measurements can be inverted into depth-dependent electric conductivity profiles.

### 3.2.2 Permeability

Besides electric conductivity, the most important material property that influences the eddy current response of conductors is their magnetic permeability

$$\mu = \mu_0 \mu_r = \mu_0 (1 + \chi) \quad (44)$$

where  $\mu_0 = 4\pi \times 10^{-7}$  Vs/Am is the permeability of free space,  $\mu_r$  is the relative permeability of the material, and  $\chi$  denotes the magnetic susceptibility. Materials are broadly classified as

diamagnetic ( $\mu_r < 1$ ), paramagnetic ( $\mu_r > 1$ ) or ferromagnetic ( $\mu_r \gg 1$ ). The negative magnetic susceptibility of diamagnetism is caused by the change in the orbital angular momentum of electrons in the presence of an applied magnetic field. The positive susceptibility of paramagnetism is caused by the alignment of electron spin and orbital angular momentum with the applied magnetic field. Depending on the competition between these two opposing effects the material will exhibit either diamagnetic (e.g., copper and zinc) or paramagnetic (e.g., aluminum and titanium) behavior. The very high positive susceptibility of ferromagnetism is caused by collective alignment of magnetic moments within domains that happens below the so-called Curie temperature. Ferromagnetic materials (e.g., iron, nickel, and cobalt) exhibit not only very high magnetic susceptibility ( $\chi \approx 100$ -10,000) but numerous other unique features such as remanence, coercivity, and hysteresis [58].

In practice, conventional eddy current inspection is limited to dia- and paramagnetic conductors and otherwise paramagnetic alloys, like austenitic stainless steels, that contain a small volume fraction of ferromagnetic phases. Although duplex and fully ferromagnetic steels can be also inspected by eddy current instrumentation, then the physical mechanism underlying the operation is mainly of magnetic nature rather than conduction of eddy currents in the material. Figure 38 illustrates schematically how increasing permeability in paramagnetic materials affects the complex probe coil impedance. Increasing magnetic permeability (susceptibility) increases the probe coil's reactance and, to a much lesser degree, its resistance. If left uncorrected, excess magnetic susceptibility translates into a decrease in the apparent eddy current conductivity of the material.

One possible way of separating competing effects of different physical properties is based on the so-called grid method [59]. This model-based inversion method works the best on eddy

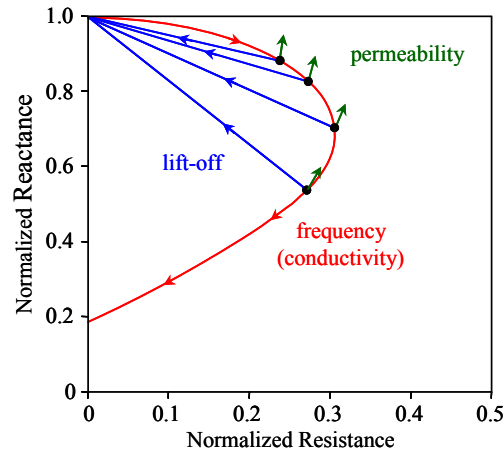


Figure 38 A schematic diagram of how increasing permeability in paramagnetic materials affects the complex probe coil impedance.

current probe coils that are produced in a highly reproducible way, such as Meandering Winding Magnetometer (MWM) probes made by high-precision photolithography, so that their impedance can be accurately pre-calculated as a function of frequency for a set of unknown parameters such as conductivity, permeability, and lift-off distance. Then, absolute physical properties can be separately estimated from the coil impedance values measured at a series of frequencies by simply superimposing the measured data on the pre-calculated grid space and finding the sought parameters by interpolation from the nearest grid points.

In numerous cases, spurious magnetic permeability variations caused by thermal or mechanical effects act like material noise and interfere with the primary goal of eddy current inspection, which could be either conductivity measurement or flaw detection. For example, low-cycle fatigue damage monitoring in austenitic stainless steel components is of primary importance in certain fracture-critical nuclear reactor plant components. Figure 39 illustrates the magnetic susceptibility versus cold work, i.e., plastic deformation, resulting from ferromagnetic martensite formation in austenitic stainless steels at room temperature. In comparison, in nickel-base superalloys, which are also rich in nickel and iron, the permeability remains unaffected by plastic deformation.

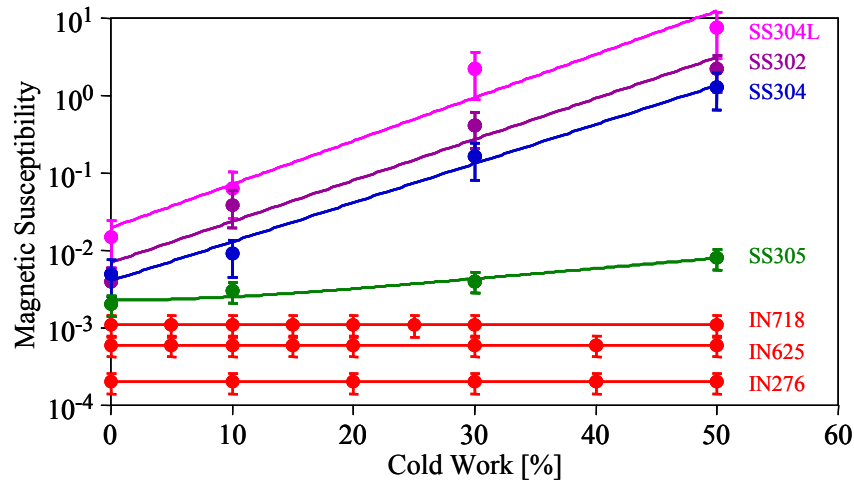


Figure 39 Changing magnetic susceptibility versus cold work as a result of ferromagnetic martensite formation in austenitic stainless steels at room temperature. There is no similar phase transformation in nickel-base superalloys.

Numerous magnetic, electric, ultrasonic, and thermoelectric methods could be exploited for detection of low-cycle fatigue damage in austenitic steels except that all of them are excessively sensitive to, and therefore overwhelmed by, martensite formation that is not directly related to the resulting life reduction [60]. The main problem is that martensite formation is very sensitive to temperature, therefore, depending on whether plasticity took place at 25 °C or 40 °C, the amount of martensite formation could change by as much as 100%, thereby changing most measurable physical parameters, especially those affected by magnetic properties [61]. Under such conditions, magnetic variations act more like spurious material noise than useful material signal and should be suppressed as much as possible. This issue will be further discussed in the following section on eddy current flow detection in connection to intrinsic limitations on the signal-to-noise ratio in eddy current inspection.

### 3.2.3 Metal Thickness

Eddy current metal thickness measurement is widely used for both for manufacturing, quality control, and in-service monitoring when access is limited to one side only [62-66]. In contrast to ultrasonic thickness gages that can be used on virtually any engineering material, eddy current

thickness measurement is limited to thin layers of conductive materials such as aircraft fuselage skin or thin-walled metal tubing. Here “thin” means that the wall thickness must be less than the actual penetration depth of the eddy current field, which is the smaller of the frequency- and material-dependent standard penetration depth and the probe-dependent geometrical penetration depth as discussed in Section 2.4. Eddy current measurement of the thickness of conductive layers is based on the sensitivity of the complex probe coil impedance, i.e., the apparent eddy current conductivity of the material, to its thickness due to the geometrical limit set by the thickness of the conductive layer on the eddy current depth distribution. In contrast, eddy current measurement of the thickness of nonconductive coatings, like polymer paint on metal substrates, is based on the excess lift-off distance presented by such layers and will be discussed separately in the next section.

Figure 40 shows schematic diagrams of (a) eddy current thickness measurement and (b) the shape of the thickness-trajectory along with the ideal thick-plate and thin-plate conductivity trajectories of the same material.

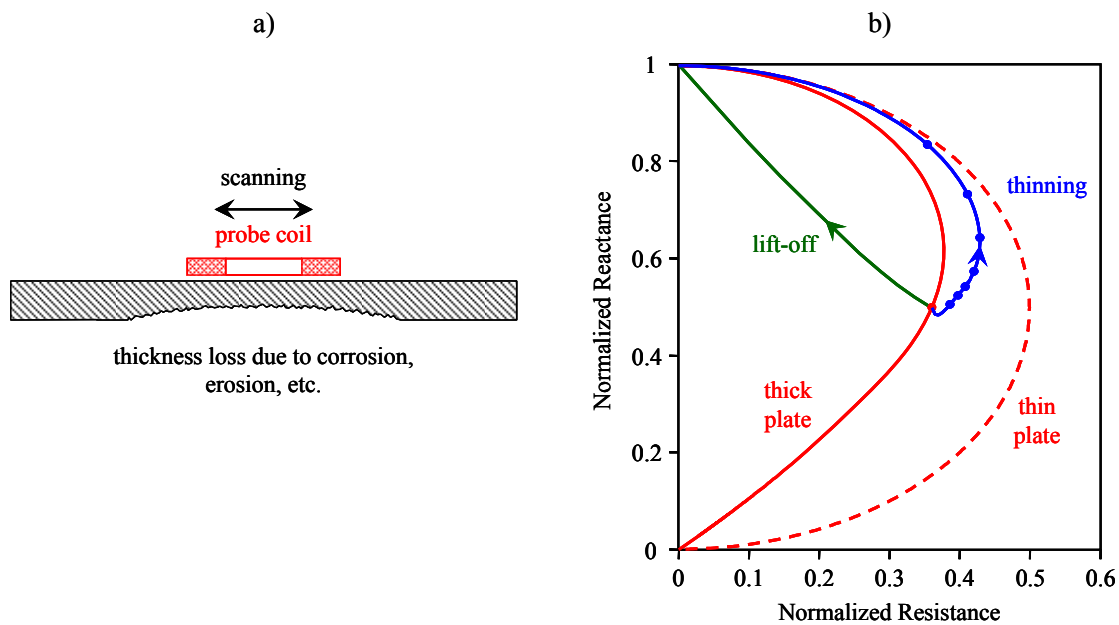


Figure 40 Schematic diagrams of (a) eddy current thickness measurement and (b) the shape of the thickness-trajectory along with the ideal thick-plate and thin-plate conductivity trajectories of the same material.



trajectories of the same material. Finite thickness not only reduces the total amount of eddy current flowing in the plate but also changes its relative distribution pattern by squeezing the current into a shallower channel closer to the probe coil. As a result, both the apparent eddy current conductivity (AECC) and the apparent eddy current lift-off (AECL) distance decrease. Interestingly, this general trend does not hold for thick plates in the transition region where the plate thickness is comparable to the standard penetration depth. As an example of this non-monotonic behavior, Figure 41 shows the apparent eddy current conductivity spectra of Inconel ( $\sigma = 1.33$  %IACS) plates of various thickness between 1 and 6 mm from 0.1 to 10 MHz. These results were obtained using the Vic-3D simulation package for an air-core pancake coil of  $a_o = 4.5$  mm outer radius,  $a_i = 2.25$  mm inner radius, and  $h = 2.25$  mm height. As the inspection frequency decreases and the AECC starts to deviate from the true conductivity of the material, first it slightly increases before it sharply drops due to the fact that the eddy current distribution cannot spread deeper into the material than the finite plate thickness.

The slight AECC increase in the transition zone is due to the fact that the phase of the eddy

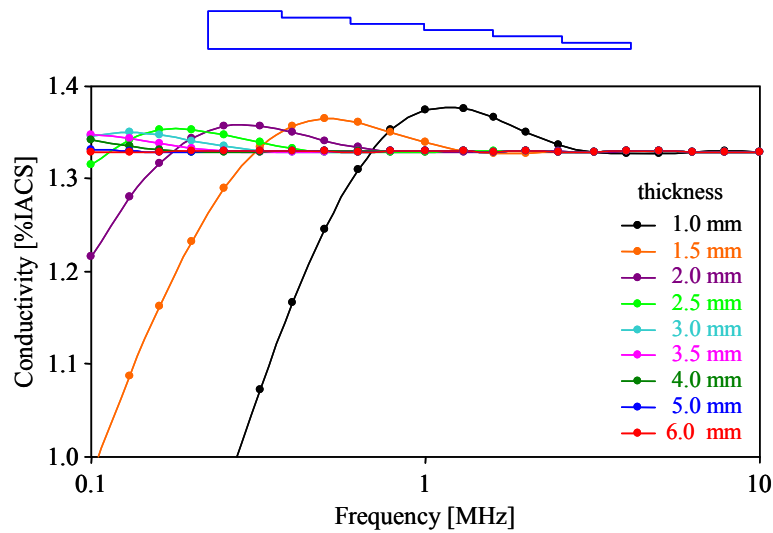


Figure 41 Apparent eddy current conductivity spectra of Inconel plates of various thickness between 1 and 6 mm from 0.1 to 10 MHz ( $\sigma = 1.33$  %IACS,  $a_o = 4.5$  mm,  $a_i = 2.25$  mm, and  $h = 2.25$  mm).

current flowing at a certain depth below the surface is opposite to that of the current flowing at the surface as we discussed it earlier in Section 1.3. While the magnitude of the eddy current intensity rapidly decreases with depth, its phase also changes and at three times the standard penetration depth, where the magnitude is small but not entirely negligible, the phase becomes opposite relative to the surface. When the thickness decreases from a high value, the first perceivable effect on the probe coil impedance is the vanishing of these weak counter rotating eddy currents, therefore the AECC goes through a small maximum before it starts to drop precipitously.

### 3.2.4 Coating Thickness

The simplest case of eddy current thickness measurement involves a nonconducting coating layer on a conducting substrate shown schematically in Figure 42. Let us assume that the outer radius of the probe coil  $a_0$  is much larger than the coating thickness  $t$  to be measured. At a sufficiently high inspection frequency where the standard penetration depth  $\delta$  is significantly less than the substrate thickness  $d$ , the apparent eddy current conductivity AECC is equal to the intrinsic electric conductivity of the substrate while the apparent eddy current lift-off AECL is equal to the sum of the actual lift-off distance  $\ell$  and the coating thickness  $t$ , which allows the accurate assessment of the coating thickness from the measured AECL. The coating thickness measurement can be readily calibrated for any unknown substrate conductivity by repeated impedance measurements over a series of plastic shims of known thickness.

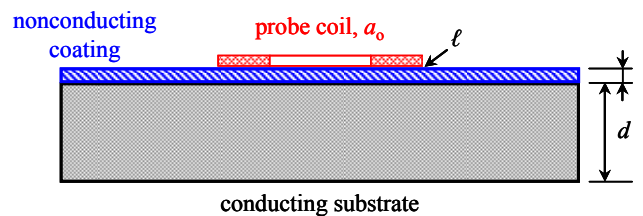


Figure 42 Eddy current thickness measurement of a nonconductive coating layer on a conductive substrate.

As an example, Figure 43 shows the (a) simulated and (b) measured AECL values for various actual lift-off distances from 100 kHz to 100 MHz. A homogenous IN100 block (1.39 %IACS) was tested at carefully controlled lift-off distances using an 8-mm-diameter spiral coil. First, a four-point linear system calibration was conducted by measuring the coil impedance on two homogenous calibration blocks (1.36 and 1.55 %IACS) with and without a 25.4- $\mu\text{m}$ -thick polymer shim. It can be shown that at high inspection frequencies the sensitivity to lift-off variations is significantly lower for smaller coils, which conflicts with the well-known trend expected for purely inductive lift-off sensitivity and can be attributed to capacitive artifacts [56].

Numerous eddy current inversion methods are available to measure conducting coating thickness on both conducting and/or magnetic substrates [59, 67-69]. Figure 44 shows a schematic diagram of eddy current measurement of the thickness and conductivity of a coating layer on a conductive substrate. These applications of eddy current inspection can be considered as special cases of eddy current conductivity profiling when the depth profile of the electric conductivity is sought from the measured complex impedance of the probe coil at different frequencies, which is the topic of the next section.

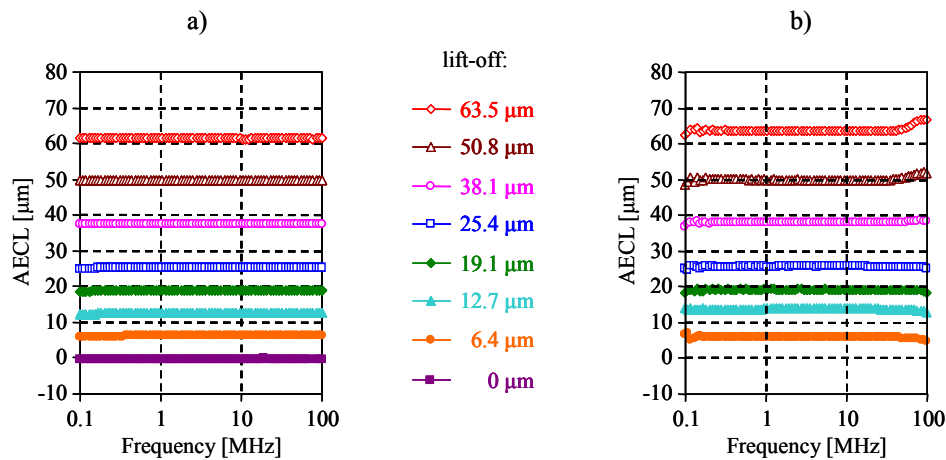


Figure 43 Simulated (a) and measured (b) AECL spectra for various values of actual lift-off distance from 0.1 to 100 MHz using an 8-mm-diameter spiral coil.

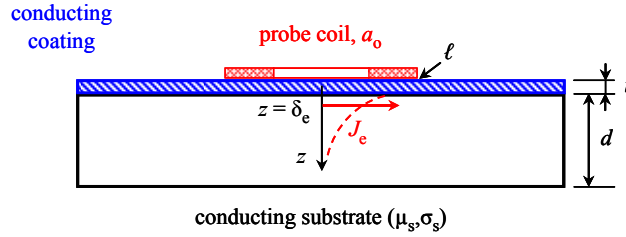


Figure 44 A schematic diagram eddy current measurement of the thickness and conductivity of a coating layer on a conductive substrate.

### 3.2.5 Depth Profiling

As described in Section 3.2.1, the AECC of a specimen represents the conductivity of a hypothetical, perfectly smooth, flat, and homogeneous conducting half-space that would produce exactly the same complex coil impedance as the specimen at the given inspection frequency. When the specimen is inhomogeneous with a given conductivity depth profile, the AECC becomes frequency dependent. Of course, the intrinsic electric conductivity of the material is independent of frequency in practically all cases. The frequency dependence of the AECC is caused by the depth dependence of the electric conductivity combined with the frequency dependence of the eddy current penetration depth.

First, let us consider the direct problem of eddy current characterization of a continuously varying near-surface conductivity profile  $\sigma(z)$  in a nonmagnetic half-space. Solving the direct problem involves the calculation of the frequency-dependent complex coil impedance for a given coil geometry and lift-off distance. Most known solutions of this problem are based on the analytical method originally developed by Dodd and Deeds for a homogeneous half-space covered with a single conducting layer [21]. The same approach was subsequently extended using the transfer matrix method to general stratified media containing an arbitrary number of layers [22]. Because of the excellent numerical stability of this method, it can be very easily adapted to solving the direct problem for a half-space with a continuously varying arbitrary

conductivity profile using discretization into a piecewise homogeneous stratified medium. Both numerical [70-72] and, at least for special profiles, analytical solutions [73, 74] are readily available in the literature. These methods have all been developed for calculating the electric impedance of the probe coil, but they can be extended to determining the AECC of the specimen by the previously described four-point linear interpolation technique if the coil impedance is also calculated for two homogeneous calibration blocks with and without a small lift-off.

Because of the finite size of the probe coil, the direct problem is 2-D for axisymmetric coils. In the case of near-surface conductivity variations, e.g., in the case of apparent conductivity loss due to surface roughness [75-77] or surface-treated metals [55, 78-80], it is advantageous to measure the AECC as a function of frequency instead of just the complex coil impedance. In these cases, most of the information is contained in the high-frequency end of the spectrum, where the standard penetration depth  $\delta$  in the conductor is much less than the diameter of typical probe coils. Under these conditions, we can directly estimate the frequency-dependent AECC from the plane wave reflection coefficient  $R(f)$  of the conductor, which can be readily calculated using the well-known relationship

$$R = \frac{\eta_0 - Z(0)}{\eta_0 + Z(0)}. \quad (45)$$

Here  $Z(0)$  is the electric surface impedance of the conducting half-space and  $\eta_0 = \sqrt{\mu_0 / \epsilon_0}$  ( $\approx 377 \Omega$ ) is the intrinsic electric impedance of free space, where  $\mu_0$  and  $\epsilon_0$  are the electric permeability and permittivity of free space. For a homogeneous conducting half-space, the reflection coefficient is simply

$$R_0 = \frac{\eta_0 - \zeta_i}{\eta_0 + \zeta_i}, \quad (46)$$

where  $\zeta_i = \sqrt{-i\omega\mu_i/\sigma_i}$  is the intrinsic impedance of the intact material,  $\omega = 2\pi f$  denotes the angular frequency, and  $\mu_i$  is the magnetic permeability of the intact conductor. Because of the usually very large impedance mismatch at the boundary, the measured complex reflection coefficient can be approximated from Eq. (46) as follows

$$R_0 \approx 1 - \frac{2\zeta_i}{\eta_0} = 1 - 2\sqrt{\frac{-i\omega\mu_i\epsilon_0}{\sigma_i\mu_0}} = 1 - \alpha + i\alpha, \quad (47)$$

where

$$\alpha = \sqrt{\frac{2\omega\mu_i\epsilon_0}{\sigma_i\mu_0}} \ll 1 \quad (48)$$

is a very small real number. In order to calculate the frequency-dependent AECC( $f$ ) of an inhomogeneous specimen from the measured reflection coefficient,  $R(f)$  must be substituted for  $R_0$  into Eq. (47) and then  $\alpha$  can be calculated from  $\alpha \approx \text{Re}\{1 - R(f)\}$ . Finally, the conductivity of the equivalent hypothetical homogeneous medium AECC( $f$ ) =  $\sigma_i$  can be calculated from Eq. (48) as follows [76, 77]

$$\text{AECC}(f) \approx \frac{4\pi f\mu_i\epsilon_0}{\mu_0[1 - \text{Re}\{R(f)\}]^2}. \quad (49)$$

For an inhomogeneous conductor with known electric conductivity profile  $\sigma(z) = \sigma_i p(z)$  the intrinsic impedance  $\zeta(z) = \zeta_i / \sqrt{p(z)}$  and complex wave number  $k(z) = k_i \sqrt{p(z)}$  are both functions of depth, where  $k_i = \sqrt{i\omega\mu_i\sigma_i}$  denotes the wave number in the intact conductor. The surface impedance can be calculated as a function of depth by repeated application of the well-known wave-guide equation

$$Z(z) = \zeta(z) \frac{Z(z+\Delta) - i\zeta(z)\tan[k(z)\Delta]}{\zeta(z) - iZ(z+\Delta)\tan[k(z)\Delta]}, \quad (50)$$

where  $\Delta$  is a sufficiently small discretization step size and the calculation must be started deep enough below the surface where the electric conductivity is equal to the unperturbed intact

conductivity  $\sigma_i$  of the material. It should be mentioned that this 1-D iterative technique is a simplified version of the local transfer matrix technique commonly used to solve more complicated 2-D and 3-D direct eddy current problems [22, 70-74]. The simplicity of the above described method lies in the fact that the AECC is directly determined from the plane wave reflection coefficient of the surface rather than calculating the complex impedance of a finite-size coil by integration and then evaluating this impedance for the AECC using reference calculations on known calibration blocks.

In order to translate the measured frequency-dependent AECC into a depth-dependent electric conductivity profile in a nonmagnetic medium, a simplistic direct inversion technique can be used [78]. According to this method, at any given frequency the measured AECC is roughly equal to the actual electric conductivity at half of the standard penetration depth assuming that: (i) the electric conductivity variation is limited to a shallow surface region of depth much less than the probe coil diameter, (ii) the relative change in electric conductivity is small, and (iii) the electric conductivity depth profile is continuous and fairly smooth.

Because of the lack of direct physical relationship between the measured complex coil impedance and the sought conductivity profile, most inversion methods start from known solutions of the direct problem and seek to find the best possible fit with the coil impedance to be inverted by multiple-variable optimization. In contrast, the frequency-dependent AECC lends itself to a very simple, though admittedly crude, physical interpretation. In this approximation, the standard penetration depth of the eddy current distribution, which is equal to the actual penetration depth when finite-probe effects are neglected, can be calculated from the conductivity of the intact material as  $\delta_i(f) = 1/\sqrt{\pi f \mu_i \sigma_i}$ . Furthermore, one can completely neglect the exponential decay of the eddy current distribution and the integrating effect of this

distribution below the surface and instead assume very crudely that the eddy current distribution is localized at half of the standard penetration depth so that at any given frequency the apparent eddy current conductivity corresponds directly to the actual electric conductivity at that depth

$$\text{AECC}(f) \approx \sigma(\delta_e) = \sigma \left( \frac{1}{2\sqrt{\pi f \mu_i \sigma_i}} \right), \quad (51)$$

where the “effective” penetration depth  $\delta_e = \delta_i/2$  is equal to half the standard penetration depth in the intact material. Then, the electric conductivity profile can be directly estimated from the measured  $\text{AECC}(f)$  spectrum as follows

$$\sigma(z) \approx \text{AECC} \left( \frac{1}{4\pi z^2 \mu_i \sigma_i} \right). \quad (52)$$

It might seem highly unlikely that such a simplistic inversion procedure could accurately predict the actual conductivity profile  $\sigma(z)$  from the measured frequency-dependent  $\text{AECC}(f)$ . Indeed, generally, this simplistic inversion method yields rather poor results. As an example, Figure 45 shows the comparison of the input conductivity profile, the corresponding AECC as predicted by the 1-D approximation, and the conductivity profile inverted from this AECC spectrum for a 254- $\mu\text{m}$ -thick homogeneous surface layer of 1% excess conductivity. In such a homogeneous layer represented by a rectangular conductivity profile the accuracy of the above described simplistic inversion method obviously leaves much to be desired as the sharp transition is smoothened out by the approximation that completely neglects the integrating effect of the eddy current distribution. However, even in this case, the half-peak depth of the reconstructed profile is almost exactly the same as that of the input profile. In contrast, Figure 46 shows the comparison of the input conductivity profile, the corresponding AECC as predicted by the 1-D approximation, and the conductivity profile inverted from this AECC spectrum for a 254- $\mu\text{m}$ -



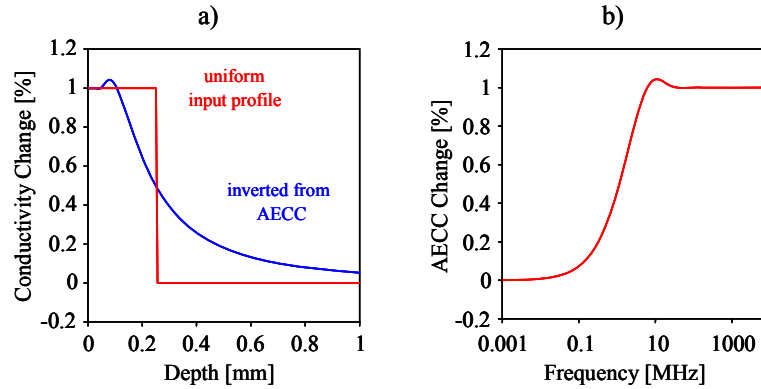


Figure 45 Comparison of (a) the input conductivity profile, (b) the corresponding AECC as predicted by the 1-D approximation, and (a) the conductivity profile inverted from this AECC spectrum for a 254- $\mu\text{m}$ -thick homogeneous surface layer of 1% excess conductivity.

thick Gaussian layer of 1% excess conductivity. Although some discrepancy still exists between the input and inverted conductivity profiles at larger depths, the agreement between them is very good up to about the half-peak depth.

More recently, a highly convergent iterative inversion technique was developed based on the same approach used in the above described simplistic approximation [81]. Alternatively, best fitting of the measured electric coil impedance to the known analytical solution can be used assuming that the conductivity profile can be characterized by a small number of independent parameters [82]. Eddy current conductivity profiling continues to be an active research area [83,

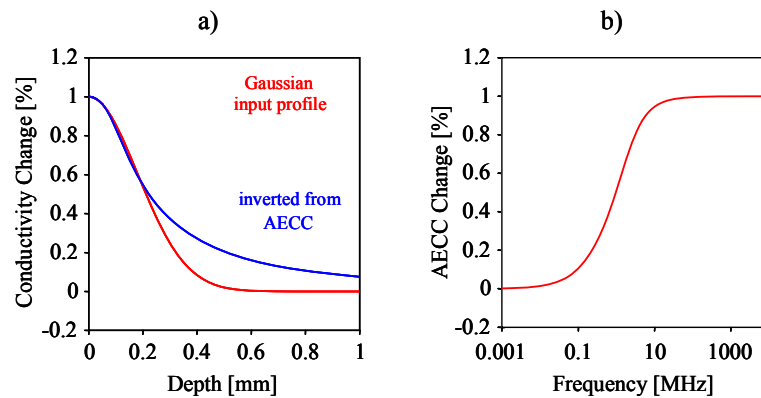


Figure 46 Comparison of (a) the input conductivity profile, (b) the corresponding AECC as predicted by the 1-D approximation, and (a) the conductivity profile inverted from this AECC spectrum for a 254- $\mu\text{m}$ -thick Gaussian layer of 1% excess conductivity.

84]. Based on Dodd and Deeds' classical approach [21] inversion techniques using various best-fitting strategies are available [71-74, 85, 86]. Alternatively, the coil impedance can be calculated from the volume-integral of the 3-D Green's function [70, 87] which was the method used in the numerical calculations presented in the previous chapter. Other known inversion methods are based on spatially periodic excitation and parameter separation, when the penetration depth is controlled by the periodicity of the probe coil rather than by the frequency-dependent standard penetration depth of the material and the overall dimensions of the probe coil [59, 88, 89]. Eddy current data could be also inverted by the application of a diffusion-to-wave transformation, but it was found that the transformation lacks robustness and leads to numerical instabilities when applied to time-harmonic sources [90].

### *3.2.6 Flaw Detection*

Eddy current flaw detection is aimed at the detection and characterization of surface-breaking and near-surface cracks that influence the eddy current distribution in the specimen under test and therefore the complex electric impedance of the probe coil. Numerous theoretical models and analytical and computational solutions are available in the literature to predict the modified complex impedance of a probe coil in the presence of a crack [91-93]. Figure 47 shows schematically the complex impedance change caused by a surface-breaking crack relative to the conductivity trajectory of an intact substrate at two different inspection frequencies. In the presence of a crack the eddy current becomes weaker and is also pushed deeper into the specimen as it flows around and below the crack. As a result, the apparent eddy current conductivity (AECC) decreases while the apparent eddy current lift-off (AECL) increases. The perturbation caused by the flaw in the eddy current distribution depends not only on the properties of the crack, such as its size, shape, and interface conditions, but also on its orientation

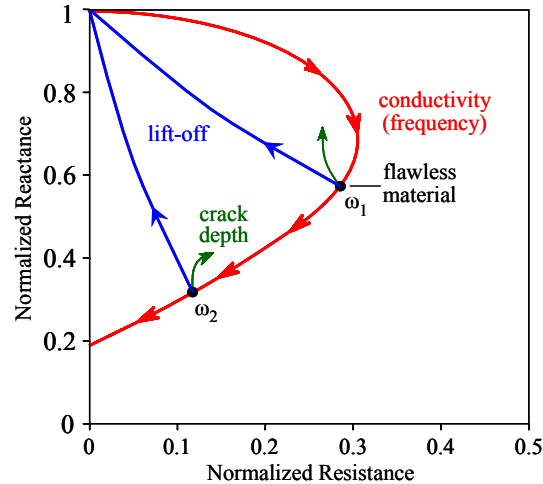


Figure 47 A schematic illustration of the complex impedance change caused by a surface-breaking crack relative to the conductivity trajectory of an intact substrate at two different inspection frequencies.

and location relative to the probe coil and depth below the surface. As an example, let us consider the simple case of a surface-breaking semi-circular open crack. Figure 48 shows the relative position of the crack mouth as the probe coil is scanned along its line on the surface. Out of all possible lines of scanning, this central line offers the best flaw detectability since the presence of the crack deflects only the eddy current flowing normal to it while eddy current running parallel to it remains essentially unaffected.

As it is shown in Figure 48, a small crack intercepts the eddy current that flows around the mirror image of the probe coil inside the specimen, twice. When the probe coil is directly above a small crack that is significantly shorter than the probe diameter, the eddy current distribution remains undisturbed, therefore the coil impedance does not show any indication of the crack. The maximum flaw signal produced by a small crack in eddy current inspection can be

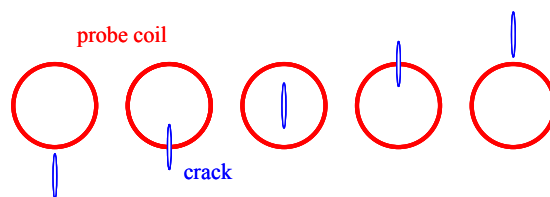


Figure 48 Relative position of the crack mouth as the probe coil is scanned along its line on the surface.

characterized by the change in coil impedance produced by the crack in its optimum position when the center of the coil is offset relative to the center of the crack by exactly the probe radius in such a direction that the local eddy current flows normal to the crack.

Figure 49 shows how the eddy current contrast between the cracked and intact solid changes with increasing flaw radius for a semi-circular crack with its center lying on the surface. These results were calculated with the commercially available Vic-3D volume-integral simulation software for a pancake probe coil of outer radius  $a_o = 1$  mm, inner radius  $a_i = 0.75$  mm, and height  $h = 1.5$  mm. The material used in this example was austenitic stainless steel ( $\sigma = 2.5$  %IACS,  $\mu_r = 1$ ) and the inspection frequency was fixed at  $f = 5$  MHz so that the standard penetration depth  $\delta \approx 0.19$  mm was much smaller than the probe dimensions. For easier interpretation the maximum eddy current contrast produced by a given flaw size under these conditions is plotted as the apparent eddy current conductivity (AECC) of the cracked material normalized to the actual electric conductivity of the intact material.

Figure 50a shows the calculated normalized AECC variation versus normalized flaw size

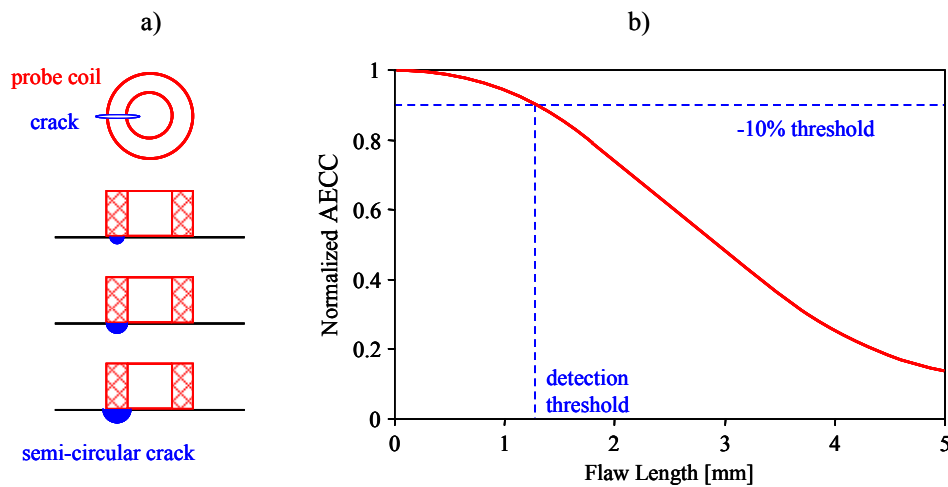


Figure 49 A schematic diagram of the test configuration (a) and the resulting eddy current contrast (b) between the cracked and intact conductor versus flaw length for a semi-circular crack with its center lying on the surface ( $a_o = 1$  mm,  $a_i = 0.75$  mm,  $h = 1.5$  mm, austenitic stainless steel,  $\sigma = 2.5$  %IACS,  $\mu_r = 1$ ,  $f = 5$  MHz,  $\delta \approx 0.19$  mm).

characteristics at two different frequencies in stainless steel. As expected from the results previously presented for the lateral resolution of eddy current inspection in Section 2.4, the eddy current distribution becomes more concentrated below the probe coil as the frequency increases, though the effect is rather limited since the lateral resolution is determined by the probe size at both low and high inspection frequencies. Ultimately, the detectability of a flaw will depend on the signal-to-noise ratio (SNR) produced by it. Here, the signal is defined as the apparent eddy current conductivity loss caused by the presence of the flaw and the material noise is the apparent conductivity variation intrinsic to the flawless material.

Figure 50 illustrates the flaw detection problem in the presence of  $\Delta\sigma_N = 2.5\%$  peak-to-peak AECC noise. The normalized flaw size is defined as the radius of the semi-circular surface crack divided by the outer radius  $a_o = 1$  mm of the probe coil (the inner radius and height of the coil were  $a_i = 0.75$  mm and  $h = 1.5$  mm, respectively). Due to its higher depth and lateral resolution the same probe coil offers much better flaw detectability at 5 MHz than at 1 MHz. In terms of detection threshold at  $\text{SNR} = 1$ , the normalized flaw size is 0.48 at 1 MHz and 0.26 at 5 MHz. While the flaw signal almost always increases with inspection frequency, the material noise can either increase or decrease. In eddy current inspection, material noise could be due to

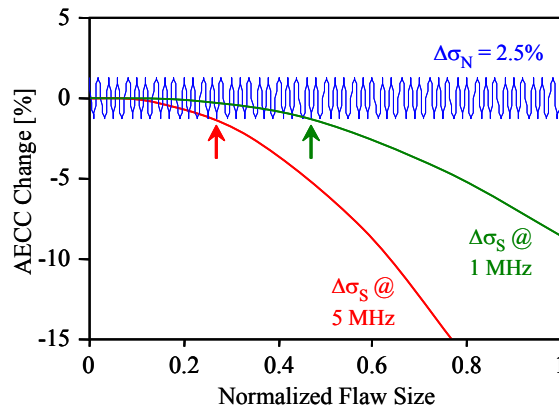


Figure 50 Calculated normalized AECC variation versus normalized flaw size characteristics at two different frequencies in stainless steel ( $\sigma = 2.5\%$  IACS). The arrows indicate the detection threshold at  $\text{SNR} = 1$ .

point to point variations in either electric conductivity or, in some special cases, magnetic permeability.

Figure 51 shows eddy current images of 0.65-mm long cracks in (a) Al2024 and (b) Ti-6Al-4V (12.7 mm  $\times$  12.7 mm). Both scans were taken by the same 1.52-mm-diameter probe coil at 2 MHz. The aluminum alloy exhibits not only relatively high, but also very uniform, electric conductivity, therefore the characteristic eight-shaped flaw signal expected from Figure 48 perfectly separates from the essentially noiseless background. In contrast, the titanium alloy exhibits not only relatively low, but also highly non-uniform electric conductivity, therefore the otherwise similar flaw signal can be barely separated from the background material noise. In the case of titanium alloys, which preferentially crystallize in hexagonal symmetry, the electric conductivity exhibits crystallographic anisotropy and therefore electric material conductivity noise [32, 94]. This material noise is very similar to the ultrasonic grain noise observed in most coarse-grained polycrystalline materials, though it is limited to only a few noncubic metals that are used as structural materials. The reason for this is that, in contrast to elastic stiffness, which is a fourth-order tensor and therefore strongly anisotropic in cubic crystals, second-order tensors

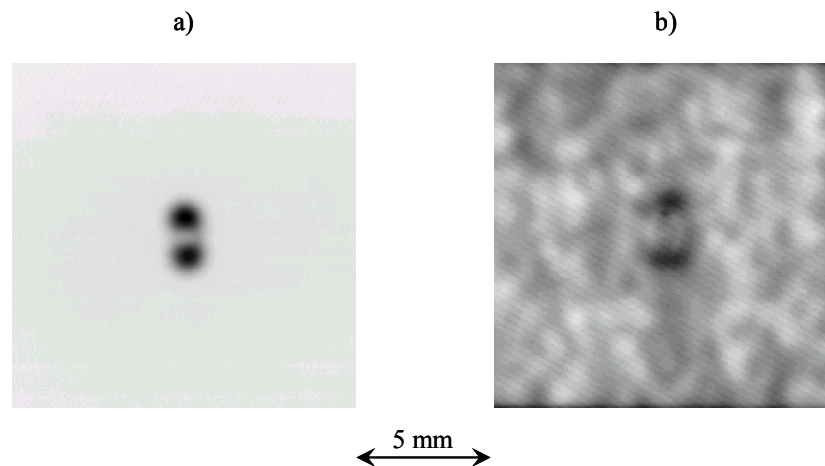


Figure 51 Eddy current images of 0.65-mm long cracks in (a) Al2024 and (b) Ti-6Al-4V (2 MHz, 1.52-mm-diameter probe coil, 12.7 mm  $\times$  12.7 mm).

like the electric conductivity are perfectly isotropic in cubic crystals therefore such materials do not produce anisotropic grain noise in eddy current inspection. This issue will be discussed in further detail in the next section dedicated to eddy current materials characterization.

Of course, sources other than anisotropic grain noise could also contribute to a non-uniform conductivity distribution that might appear as material noise in eddy current inspection. As an example, Figure 52 shows the AECC images of (a) inhomogeneous forged Waspaloy (107 mm  $\times$  53.3 mm) and (b) homogeneous powder metallurgy IN100 (56 mm  $\times$  28 mm) specimens at 6 MHz. The inhomogeneous as-forged Waspaloy exhibits a conductivity range of  $\approx 1.38$ -1.47 %IACS or  $\pm 3$  % relative variation around the average value. In comparison, the otherwise fairly similar IN100 nickel-base superalloy is made by powder metallurgy and exhibits a very homogeneous electric conductivity in the range of  $\approx 1.33$ -1.34 %IACS or  $\pm 0.4$  % relative variation around the average value. In spite of their high nickel and iron content, nickel-base superalloys are nonmagnetic at room temperature, therefore the observed AECC variations are also nonmagnetic in nature.

This conclusion can be easily verified by checking the frequency dependence of the measured AECC at various locations [79]. Figure 53 shows the AECC spectra of the measured

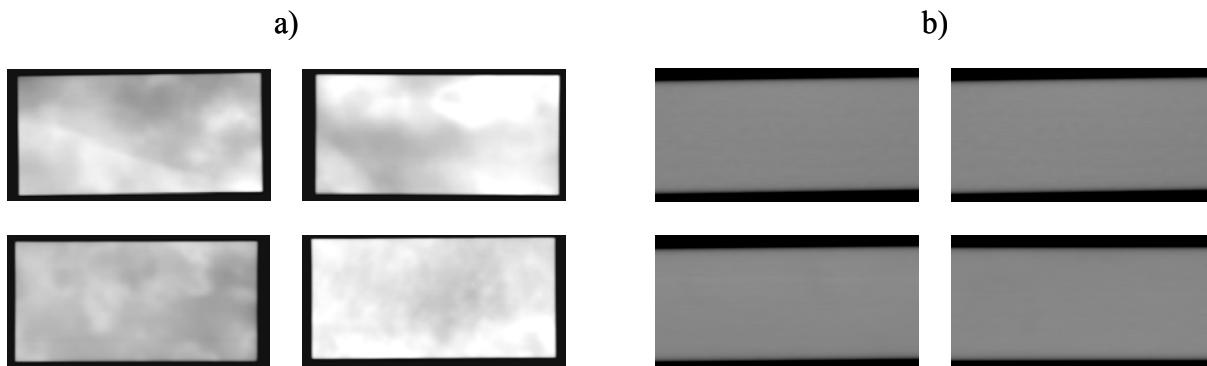


Figure 52 AECC images of (a) inhomogeneous forged Waspaloy (107 mm  $\times$  53.3 mm) and (b) homogeneous powder metallurgy IN100 (56 mm  $\times$  28 mm) specimens at 6 MHz.

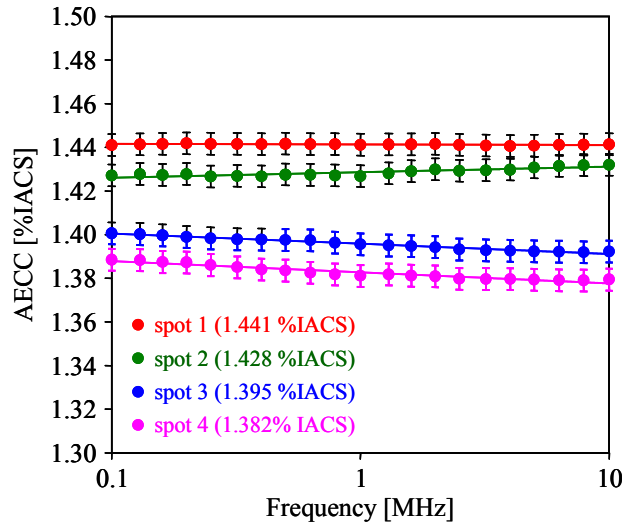


Figure 53 AECC spectra of conductivity material noise at four locations in as-forged Waspaloy.

AECC in as-forged Waspaloy at four locations from 0.1 MHz to 10 MHz. The variation of the AECC is essentially frequency independent due to the large volumetric size of the inhomogeneous domains. As the frequency decreases, the eddy current penetrates deeper into the material and also spreads a little wider in the radial direction. As a result, there is some change in the AECC with frequency at most locations, however on the average this frequency dependence essentially cancels out over many points.

Another common source of AECC variation that can significantly limit the detectability of surface-breaking and near-surface cracks is inhomogeneous magnetic permeability distribution. It is well known that cold work or spurious thermal effects can cause partial ferromagnetic transformation and the formation of ferromagnetic precipitates in otherwise paramagnetic materials. This phenomenon is best known for austenitic stainless steels that exhibit significant martensite formation under relatively small levels of plastic strain [95, 96]. What makes this effect especially unpredictable is that it is strongly temperature dependent [97]. Depending on whether the otherwise negligible plastic deformation took place at 25 °C or 40 °C, the amount of the generated martensite could change by as much as 100%, thereby significantly changing most



measurable physical parameters, especially those affected by magnetic properties such as AECC. Usually, the result is a microstructure with magnetic permeability changing significantly from point to point. As an example, Figure 54 shows the eddy current images of identical edm notches in SS304 coupons of varying material noise level at  $f = 5$  MHz. In each case the average AECC far away from the flaw was  $\approx 2.4$  %IACS. The peak AECC reduction caused by the  $0.40 \times 0.20 \times 0.03$  mm<sup>3</sup> (length $\times$ depth $\times$ width) edm notches was essentially the same at  $\Delta\sigma_S \approx 1.4\%$  in each specimen. What influenced the detectability of these flaws was the changing level of material noise that varied from a high value of  $\Delta\sigma_N \approx 2.9\%$  standard deviation yielding  $\text{SNR} \approx 0.5$  to a low value of  $\Delta\sigma_N \approx 0.4\%$  standard deviation yielding a much better  $\text{SNR} \approx 3.5$ .

Undoubtedly, the characteristic eight-shaped image produced by small directional cracks could be recognized by specialized signal processing, and even more so by a trained human inspector, even when the SNR produced by the flaw is close to unity. Still, it is clear that material noise of magnetic origin can easily overwhelm any eddy current inspection system regardless of the intrinsic electric SNR of the system itself. What makes material noise of magnetic origin unique and markedly different from otherwise similar looking conductivity noise is the characteristic frequency dependence of the AECC variations caused by magnetic

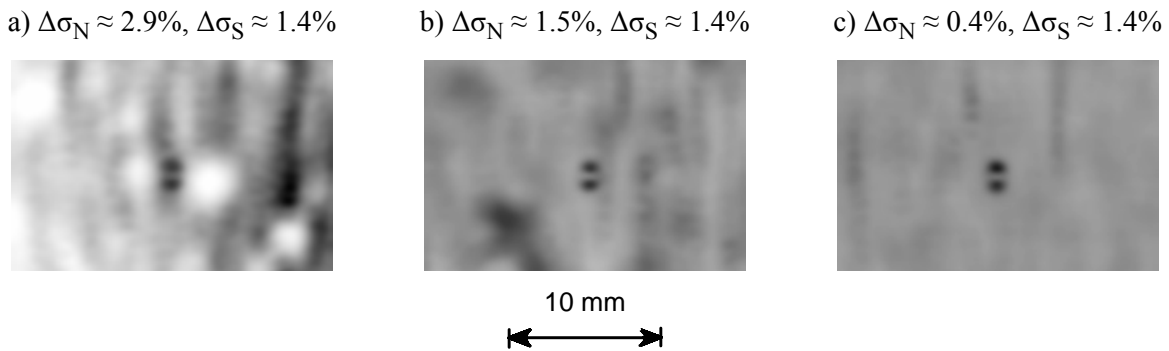


Figure 54 Eddy current images of  $0.40 \times 0.20 \times 0.03$  mm<sup>3</sup> (length $\times$ depth $\times$ width) edm notches in SS304 coupons of varying material noise level at  $f = 5$  MHz.

susceptibility variations. In order to illustrate this effect, Figure 55 shows the various levels of magnetic susceptibility material noise in the same stainless steel 304 block containing a  $0.51 \times 0.26 \times 0.03 \text{ mm}^3$  edm notch at (a) 0.1 MHz and (b) 5 MHz ( $25.4 \text{ mm} \times 25.4 \text{ mm}$ ). For a given primary magnetic field produced by the probe, magnetic variations exert mainly direct, i.e., frequency-independent effect on the magnetic flux density. In contrast, electric conductivity exerts an indirect effect that is proportional to the time rate of change through the strength of the induced eddy currents, therefore the effect increases in relative terms as the frequency increases.

Although the magnetic permeability also influences the average eddy current penetration depth, this overall influence is less significant than the accompanying inhomogeneity. As a result, the AECC noise caused by magnetic susceptibility variations actually decreases roughly proportionally to the square root of frequency. At high frequencies, the SNR of near-surface flaws further increases because the flaw signal itself also increases due to better lateral and, especially, depth resolution, therefore magnetic susceptibility noise is most efficiently suppressed by increasing the inspection frequency. In comparison, as we saw, electric conductivity material noise cannot be suppressed simply by increasing the inspection frequency.

### 3.3 Eddy Current Materials Characterization

Although quantitative eddy current materials characterization is far less developed than its

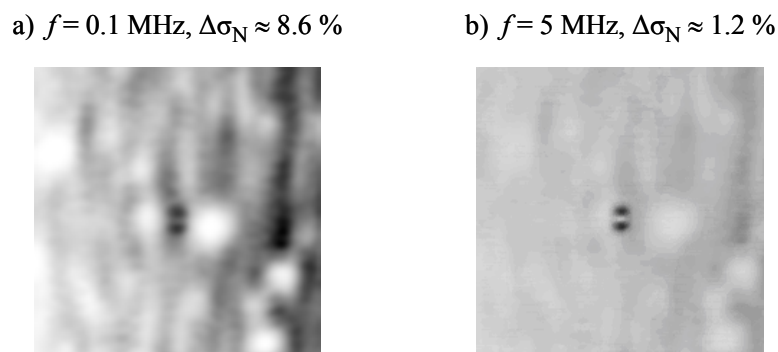


Figure 55 Magnetic susceptibility material noise in the same stainless steel 304 block containing a  $0.51 \times 0.26 \times 0.03 \text{ mm}^3$  edm notch at two different inspection frequencies ( $25.4 \text{ mm} \times 25.4 \text{ mm}$ ).

ultrasonic counterpart, it is certainly an evolving field with excellent opportunities. In the following brief summary only a few typical applications will be reviewed to illustrate this potential. These particular examples will include characterization of crystallographic texture, grain size, hardness, and residual stress assessment.

### 3.3.1 Texture

Generally, the term texture is used in materials characterization to describe the prevailing directionality, i.e., anisotropy of material properties. Figure 56 illustrates the microstructures of (a) texture-free and (b) textured polycrystalline materials. The texture-free, e.g., cast or annealed, material consists of equiaxed randomly oriented grains. In contrast, the textured, e.g., forged, rolled, pressed, or drawn, material consists of grains that are elongated in a common direction determined by the thermo-mechanical effect (plastic strain, temperature gradient, etc.) that caused the texture. In addition to this so-called morphological texture, the grains often crystallize in a preferential direction so that their individual anisotropic properties do not completely average out on the macroscopic scale, which is referred to as crystallographic texture.

Elastic anisotropy of single crystals plays an important role in ultrasonic materials characterization of polycrystalline materials. While acoustic grain noise has an obvious adverse, often prohibitive, effect on ultrasonic flaw detection, it can be also exploited for ultrasonic characterization of the grain structure. Electric anisotropy exhibited by specific types of

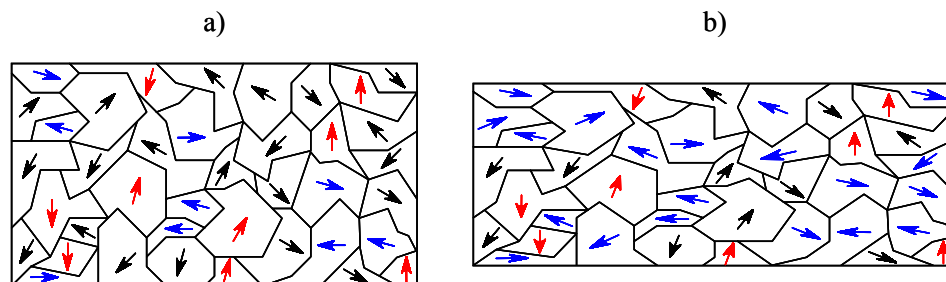


Figure 56 A schematic illustration of (a) texture-free and (b) textured microstructures in polycrystalline materials.

crystallographic classes can play a very similar role in electromagnetic testing of polycrystalline metals. All physical properties relating two first-order tensor quantities are characterized by second-order tensors, the directivity of which can be represented by an ellipsoid of revolution [98]. Such properties include electrical and thermal conductivity, thermoelectricity, dia- and paramagnetism, and dielectricity. In the most common cubic crystallographic system, the ellipsoid degenerates into a sphere and these properties become fully isotropic. However, in noncubic materials the same physical properties are inherently anisotropic. In contrast, elastic material properties relate two second-order tensor quantities therefore they are characterized by fourth-order tensors. As a result, from an electric point of view, cubic crystals are also anisotropic just like other crystallographic classes.

Neighbor was the first to apply the eddy current method to electrically anisotropic materials and showed theoretically that one can obtain the full conductance tensor from such measurements [99]. Special potential drop and eddy current coil configurations that allow the simultaneous measurement of electrical conductivity in two principal directions have been developed for texture assessment in plates [100, 101]. Although most materials are cubic and therefore do not exhibit electrical anisotropy due to crystallographic texture, weak morphological texture caused by grain boundary contributions to the electrical resistivity can cause perceivable electric anisotropy in polycrystalline materials of cubic symmetry [102]. Much stronger structural anisotropy caused by directional reinforcement in composite materials can be exploited for eddy current characterization of metal matrix composites [103, 104].

Figure 57 illustrates the geometrical configuration of a transversely isotropic crystal relative to the free surface of the specimen. In contrast with common electrically isotropic cubic crystals, less common materials of hexagonal symmetry can exhibit strong electrical anisotropy with

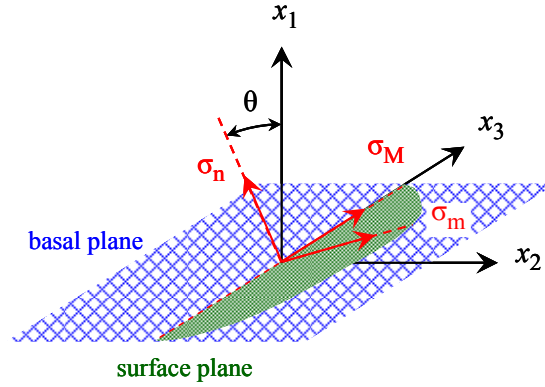


Figure 57 Geometrical configuration of a transversely isotropic crystal relative to the free surface of the specimen.

significant difference in conductivity between the basal plane and normal to it. Titanium is one of the few structural metals of practical importance, especially in aerospace applications, that preferentially crystallize in hexagonal symmetry and therefore exhibits strong electrical anisotropy.

Generally, the anisotropic constitutive relationship  $\mathbf{J} = \boldsymbol{\sigma} \mathbf{E}$  can be written in principal coordinates as follows

$$\begin{bmatrix} J_1 \\ J_2 \\ J_3 \end{bmatrix} = \begin{bmatrix} \sigma_1 & 0 & 0 \\ 0 & \sigma_2 & 0 \\ 0 & 0 & \sigma_3 \end{bmatrix} \begin{bmatrix} E_1 \\ E_2 \\ E_3 \end{bmatrix}. \quad (53)$$

For hexagonal crystals like pure titanium and its most common alloys the axial symmetry around the hexagonal axis allows the directional dependence of the electrical resistivity to be described by two orthogonal axes and the anisotropy can be represented as an ellipsoid of revolution. For fully isotropic cubic materials  $\sigma_1 = \sigma_2 = \sigma_3$ , while for transversely isotropic materials  $\sigma_1 \neq \sigma_2 = \sigma_3$ , where  $\sigma_1$  is the conductivity normal to the basal plane and  $\sigma_2$  is the conductivity in the basal plane. At  $\theta$  inclination angle from surface

$$\sigma_n(\theta) = \sigma_1 \cos^2 \theta + \sigma_2 \sin^2 \theta \quad (54a)$$

$$\sigma_m(\theta) = \sigma_1 \sin^2 \theta + \sigma_2 \cos^2 \theta, \quad (54b)$$

where  $\sigma_m$  is the minimum conductivity in the surface plane,  $\sigma_M = \sigma_2$  is the maximum conductivity in the surface plane, and  $\theta$  denotes the angle between the surface and the basal plane. The average conductivity  $\sigma_a$  measured by a non-directional circular eddy current probe coil in the surface plane is

$$\sigma_a(\theta) = \frac{1}{2} [\sigma_1 \sin^2 \theta + \sigma_2 (1 + \cos^2 \theta)]. \quad (55)$$

For example, in pure titanium  $\sigma_1 = 3.59$  %IACS and  $\sigma_2 = 3.8$  %IACS, i.e., the conductivity is approximately 6% higher in the basal plane than normal to it [105]. Because of the above described averaging effect of eddy current inspection with circular probe coils, the actual grain contrast is expected to be 50% lower in eddy current inspection than the maximum conductivity variation between principal crystallographic directions.

Macroscopic texture measurements can be conducted using directional probe coils of elliptical, racetrack, or meandering geometry [55, 59, 94]. As an example, Figure 58 shows the electric conductivity versus probe orientation in the plane of the surface in (a) highly textured Ti-6Al-4V and (b) equiaxed GTD-111 as measured by a racetrack coil at 500 kHz. Because of the significant electric grain noise to be discussed next, the measurement reproducibility indicated by the error bars is lower in the coarse-grained Ti-6Al-4V specimen. Still, it is quite apparent that the electric conductivity exhibits a considerable anisotropy of  $\approx 2.7\%$  in Ti-6Al-4V which crystallizes preferentially in hexagonal symmetry. In comparison, the GTD-111 nickel-base superalloy, which crystallizes preferentially in cubic symmetry, exhibits no perceivable anisotropy.

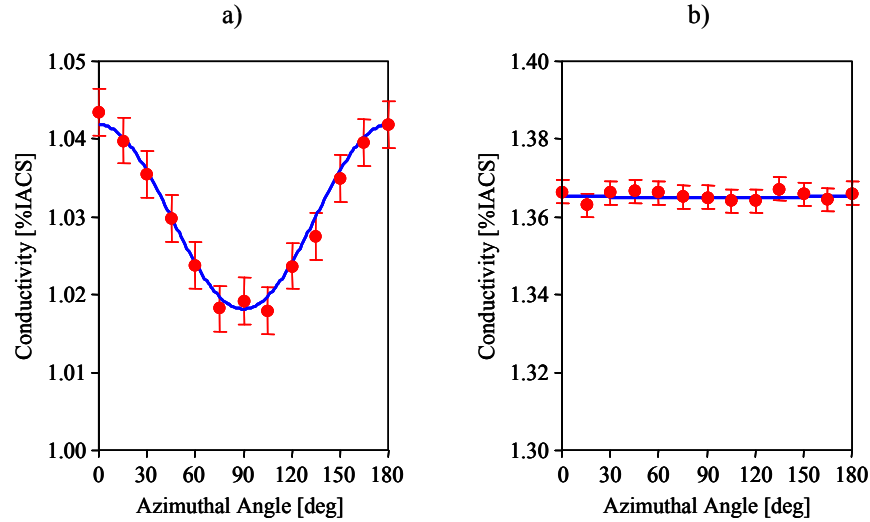


Figure 58 Electric conductivity versus probe orientation in the plane of the surface in (a) highly textured Ti-6Al-4V and (b) equiaxed GTD-111 as measured by a racetrack coil at 500 kHz.

It should be mentioned that the lack of intrinsic electric anisotropy in cubic materials can be taken advantage of for better detection of weak induced electric anisotropy due to plastic deformation or creep damage [60]. As an example, Figure 59a shows the electric conductivity variation in numerous GTD-111 nickel-base superalloy specimens at different levels of creep strain. The electric conductivity itself shows little correlation to the level of creep strain. In comparison, Figure 59b shows the relative electric conductivity anisotropy variation at different levels of creep strain, which clearly increases with increasing creep deformation.

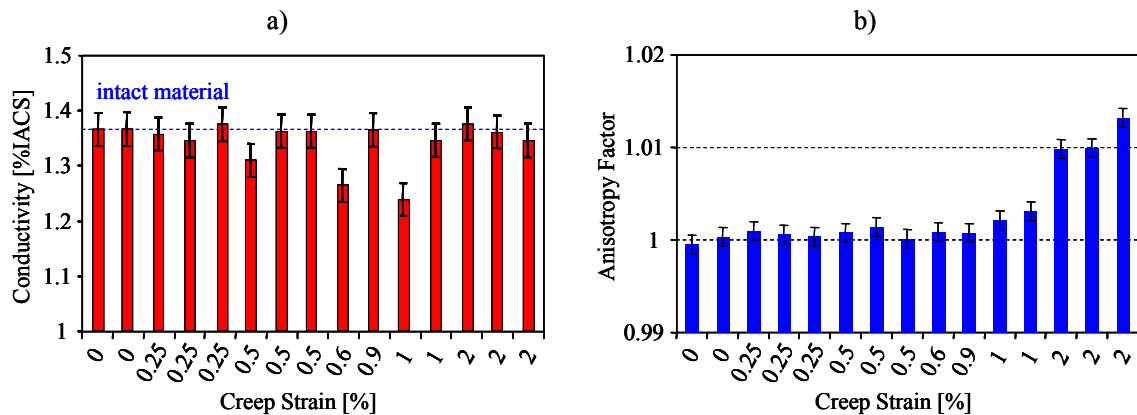


Figure 59 Absolute electric conductivity (a) and electric conductivity anisotropy (b) variation in numerous GTD-111 nickel-base superalloy specimens at different levels of creep strain.

### 3.3.2 Grain Structure

In the context of eddy current flaw detection, we already discussed how point to point conductivity variations cause a spatially incoherent material noise in eddy current inspection that ultimately limits the detectable smallest flaw. Figure 51b showed an example of such material noise in a Ti-6Al-4V specimen. The same effect can be also exploited for materials characterization just as the otherwise negative effect of grain noise in ultrasonic flaw detection can be also exploited for quantitative characterization of the microstructure in defect-free materials. Figure 60 shows six examples of typical grain noise patterns in Ti-6Al-4V specimens of various thermo-mechanical history at 2 MHz (1.5-mm-diameter probe coil, 25.4 mm  $\times$  25.4 mm). Under normal conditions, the lateral resolution of the probe coil is insufficient to see individual grains or grain colonies. Similarly, in ultrasonic imaging at typical inspection frequencies, even with focused transducers, the imaging resolution is usually not high enough to resolve individual grains. Under such conditions, the spatially coherent grain noise is an

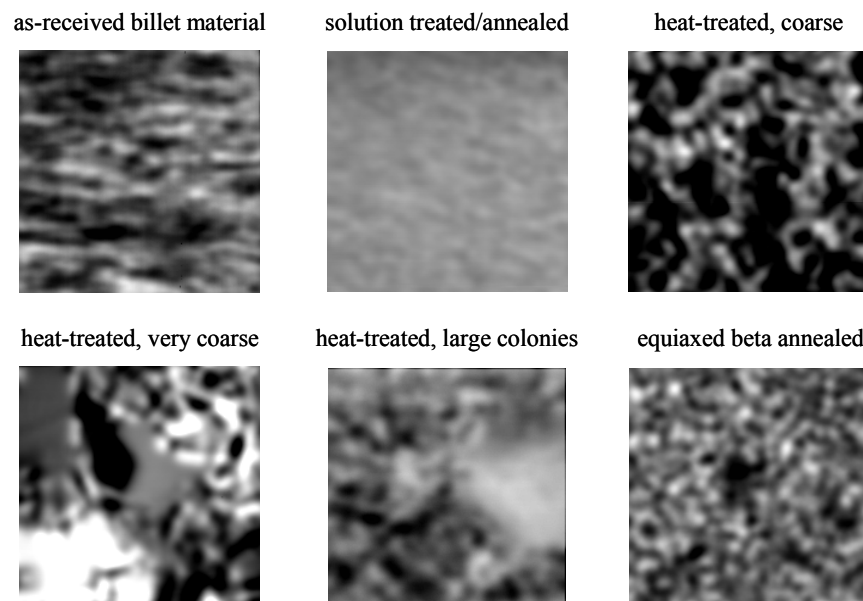


Figure 60 Examples of typical grain noise patterns in six Ti-6Al-4V specimens of various thermo-mechanical history at 2 MHz (1.5-mm-diameter probe coil, 25.4 mm  $\times$  25.4 mm).



interference pattern produced by a larger cluster of unresolved grains. In eddy current inspection a similar but simpler phase-insensitive averaging effect occurs since there is no possibility for frequency-dependent constructive and destructive interference effects.

In the depth direction the range of averaging is limited by the penetration depth, which can be made arbitrarily small by increasing the inspection frequency. However, in the plane of the surface the range of averaging is determined by the lateral resolution of the inspection, which is limited by the probe size even at very high inspection frequencies. Therefore, conclusive evidence for the origin of the grain noise observed in eddy current images of Ti-6Al-4V components can be more easily obtained by coarsening the grains rather than by reducing the imaging resolution. Figure 61 shows a direct comparison between (a) a 5-MHz eddy current scan and (b) a 40-MHz acoustic micrograph of the same coarse-grained Ti-6Al-4V sample from nearly the same area ( $25.4 \text{ mm} \times 25.4 \text{ mm}$ ). In spite of the obvious physical difference in the origin of contrast, namely electrical versus mechanical properties of the material, the eddy current contrast is quite similar to the contrast produced by scanning surface acoustic wave (SAW) microscopy.

Both techniques are sensitive to crystallographic orientation and therefore produce images on which large colonies formed by smaller grains of similar orientation show up as essentially homogeneous domains. In comparison, the more artificial optical contrast of metallurgically prepared samples is mainly due to chemical etching that brings out the grain boundaries between individual grains regardless whether there is a difference in orientation between neighboring features or not. Figure 61 illustrates that essentially the same macroscopic inhomogeneity of the microstructure can be observed in coarse-grained polycrystalline Ti-6Al-4V via eddy current imaging and acoustic microscopy. The large lamellar colonies are composed of alternating

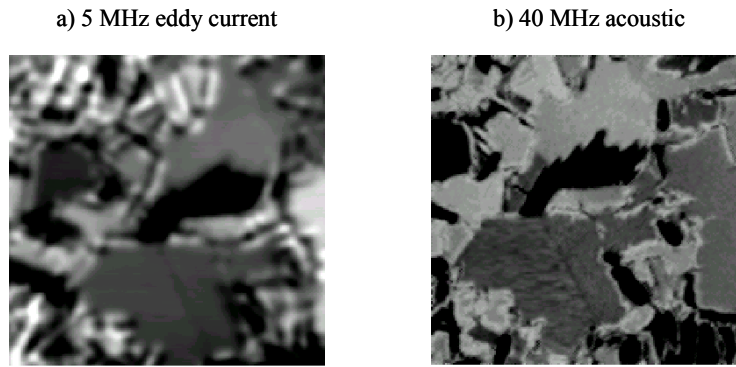


Figure 61 Comparison of (a) eddy current and (b) acoustic microscopic images of a coarse-grained Ti-6Al-4V sample from nearly the same area (25.4 mm× 25.4 mm).

plates of alpha and beta phases. The principal direction in each of these large colonies is essentially uniform, thereby forcing the colony to behave as if it were a single crystal. This coarse microstructure clearly demonstrates that like features could be observed with both eddy current and acoustic scanning techniques.

### 3.3.3 Hardness

Eddy current methods can be also used to characterize the hardness, or more precisely, hardness-related microstructural changes in metals [106-109]. Unfortunately, eddy current hardness testing, like all other indirect measurement methods, suffers from a lack of uniqueness that could arise from two fundamental causes. The first cause is non-monotonic dependence of the measured physical property on the sought material state parameter. One example of this is illustrated in Figure 62 showing the electric conductivity versus Rockwell C hardness in precipitation hardened IN718 nickel-base superalloy [60]. As the hardness increases, the electric conductivity first drops from  $\approx 1.56$  %IACS at HRC 25 to  $\approx 1.54$  %IACS at HRC 32, then increases to  $\approx 1.67$  %IACS at HRC 46, i.e., the electric conductivity is a non-monotonic, therefore not invertible function of hardness. However, over the hardness range of practical interest for engine applications (above HRC 40) the electric conductivity is a monotonic, therefore invertible function of hardness, which could be exploited for eddy current hardness

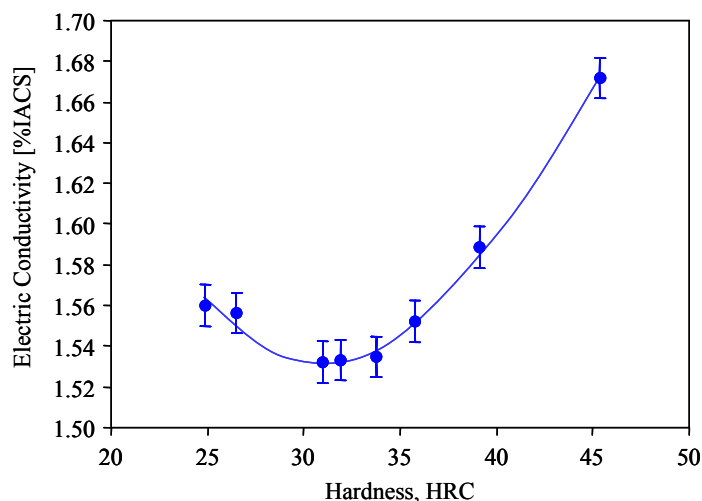


Figure 62 Electric conductivity versus Rockwell C hardness in precipitation hardened IN718 nickel-base superalloy (average AECC between 0.6 and 1.1 MHz).

assessment.

A second major cause of lack of uniqueness in eddy current hardness assessment arises from the lack of selectivity when the measured physical property changes by comparable amounts in response to more than one type of change in the state of the material. For example, the electric conductivity measured by eddy current methods is sensitive to numerous types of microstructural features, such as precipitate coarsening, changes in solute partitioning, dislocation density, coherency strain, not to mention the presence of residual stresses. Sometimes a dominant factor can be identified, but more often the measured conductivity change is caused by a combination of comparable effects. For example, in the above mentioned example of precipitation hardened IN718 nickel-base superalloy, the underlying reason turned out to be very fine nanometer-scale features of the microstructure, namely  $\gamma'$  and  $\gamma''$  precipitates, rather than micrometer-scale features, such as changing grain size or carbide precipitates [110]. In conclusion, the selectivity of eddy current hardness characterization leaves much to be desired, therefore can be used only under controlled conditions and after careful empirical calibration.

### 3.3.4 *Residual Stress*

Nondestructive residual stress assessment in fracture-critical components is one of the most promising opportunities as well as one of the most difficult challenges we face in the NDE community today. Residual stress assessment is important because there is mounting evidence that it is not possible to reliably and accurately predict the remaining service life of such components without properly accounting for the presence of residual stresses. Both the absolute level and spatial distribution of the residual stress are rather uncertain partly because residual stress is highly susceptible to variations in the manufacturing process and partly because subsequently it tends to undergo thermo-mechanical relaxation at operating temperatures. Eddy current conductivity spectroscopy emerged as one of the leading candidates for near-surface residual stress profiling in surface-treated components [55-57, 78-82, 110-117]. Eddy current residual stress profiling is based on the piezoresistivity of the material, i.e., on the characteristic dependence of the electric conductivity on stress or strain. If spurious material (e.g., magnetic permeability) and geometric (e.g., surface roughness) variations can be neglected, the frequency-dependent AECC can be inverted for the depth-dependent electric conductivity profile in the way described earlier in Section 3.2.5. Then, using the independently measured piezoresistivity of the material, the sought residual stress profile can be calculated.

In the presence of elastic stress  $\tau$  the electrical conductivity  $\sigma$  tensor of an otherwise isotropic conductor becomes slightly anisotropic. In general, the stress-dependence of the electric resistivity can be described by a fourth-order piezoresistivity tensor. In direct analogy to the well-known acoustoelastic coefficients, a widely used NDE terminology for the stress coefficient of the acoustic velocity, the stress coefficient of the electric conductivity is referred to as the electroelastic coefficient. In general tri-axial state of stress

$$\begin{bmatrix} \Delta\sigma_1 / \sigma_0 \\ \Delta\sigma_2 / \sigma_0 \\ \Delta\sigma_3 / \sigma_0 \end{bmatrix} = \begin{bmatrix} \kappa_{11} & \kappa_{12} & \kappa_{12} \\ \kappa_{12} & \kappa_{11} & \kappa_{12} \\ \kappa_{12} & \kappa_{12} & \kappa_{11} \end{bmatrix} \begin{bmatrix} \tau_1 / E \\ \tau_2 / E \\ \tau_3 / E \end{bmatrix}, \quad (56)$$

where  $E$  denotes Young's modulus,  $\Delta\sigma_i = \sigma_i - \sigma_0$  ( $i = 1, 2, 3$ ) denotes the conductivity change due to the presence of stress,  $\sigma_0$  denotes the electrical conductivity in the absence of stress, and  $\kappa_{11}$  and  $\kappa_{12}$  are the unitless parallel and normal electroelastic coefficients, respectively. During materials calibration, directional racetrack or meandering probe coils can be used to measure the parallel  $\kappa_{11}$  and normal  $\kappa_{12}$  electroelastic coefficients essentially independent of each other, as it was described in Section 3.3.1 in connection with texture assessment. In the case of shot-peened surfaces, essentially isotropic plane state of stress ( $\tau_1 = \tau_2 = \tau_{ip}$  and  $\tau_3 = 0$ ) prevails. Then, regardless whether conventional non-directional circular or directional probes are used, the effective electroelastic coefficient is  $\kappa_{ip} = \kappa_{11} + \kappa_{12}$ .

Figure 63 shows examples of piezoresistivity measurements in Waspaloy, IN718, and Ti-6Al-4V engine materials using a directional eddy current probe parallel and normal to the applied uniaxial load [115]. Here, the normalized change in conductivity  $\Delta\sigma/\sigma_0$  is plotted against the uniaxial strain  $\epsilon_{ua} = \tau_{ua}/E$ . In some materials, such as Ti-6Al-4V, the parallel and normal electroelastic coefficients are more or less equal in magnitude and opposite in sign, which renders the eddy current conductivity measurements essentially useless for residual stress assessment in the case of isotropic plane stress on surface-treated components. However, there is a very important group of materials, notably nickel-base super alloys, where the two coefficients have similar magnitudes and signs, therefore the parallel and normal effects reinforce each other to produce significant stress dependence. In order to quantitatively assess the prevailing residual stress from eddy current conductivity measurements, the electroelastic coefficients of the

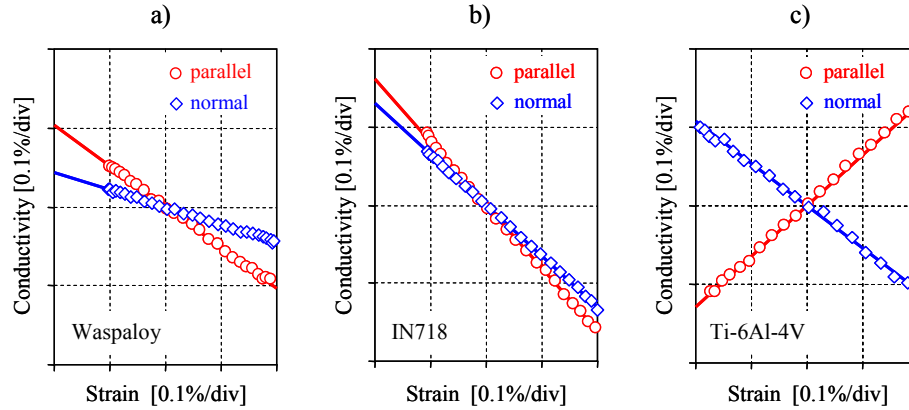


Figure 63 Piezoresistivity measurements in (a) Waspaloy, (b) IN718 and (c) Ti-6Al-4V using a directional eddy current probe parallel and normal to the applied uniaxial load.

material must be first determined using known external applied stresses. These calibration measurements are usually conducted on a reference specimen of the same material using cyclic uniaxial loads between 0.01 and 1 Hz, which is fast enough to produce adiabatic conditions. Such dynamic calibration measurements should be corrected for the thermoelastic effect, which is always positive, i.e., it increases the conductivity in tension, when the material cools down, and reduces it in compression, when the material heats up [115]. For high-conductivity alloys the difference between the adiabatic and isothermal properties could be as high as 50%. However, for high-temperature engine alloys of low electrical conductivity, such as nickel-base superalloys and titanium alloys, the difference between the isothermal and adiabatic parameters is fairly low at  $\approx 5\text{-}10\%$ .

Cold work exerts a very convoluted effect on residual stress profiling of shot-peened components by eddy current spectroscopic measurements [80]. However, it should be pointed out that this effect is much lower in moderately peened components, which exhibit better thermo-mechanical stability, and in laser shock peened (LSP) and low-plasticity burnished (LPB) specimens, which offer much lower plastic deformation than shot-peened ones. Figure 64 shows

the (a) cold work and (b) residual stress profiles obtained by destructive X-ray diffraction (XRD) measurements in shot-peened IN100 specimens of Almen 4A, 8A, and 12A peening intensities. For comparison purposes, Figure 64b also shows the residual stress profiles reconstructed from the measured AECC spectra. Except for a sharper-than-expected near-surface “hook” observed in the Almen 8A specimen, which is most probably caused by imperfect lift-off rejection above 25 MHz, the general agreement between the AECC and XRD data is very good.

In order to compensate for the uncorrected cold-work effects and to get the good overall agreement illustrated in Figure 64b, we had to use a corrected value of  $\kappa_{ip} = -1.06$ , which is 33% lower than the independently measured average value for IN100. The exact reason for the need for this “empirical” correction is currently not known, but recent results indicated that it is related to the effect of  $\gamma'$  and  $\gamma''$  precipitates [110]. Unfortunately, because of the above discussed reasons, eddy current materials characterization almost always must rely on such empirical corrections due to the lack of selectivity of the electric conductivity to the sought materials state parameter.

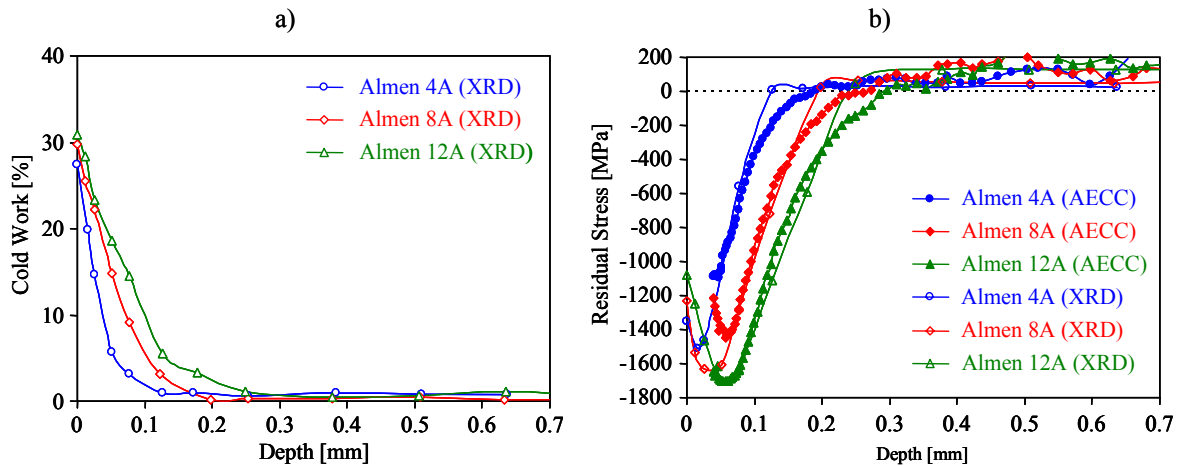


Figure 64 XRD profiling of near-surface cold work (a) and residual stress (b) profiles compared to the inverted eddy current residual stress profile in shot-peened IN100 specimens of Almen 4A, 8A and 12A intensity.

#### **4 *Current Field Measurement***

In this chapter we are going to review the main current field measurement techniques used in NDE. Current field measurements are based on the analysis of the electric current field distribution in a conducting specimen mainly for the purposes of crack detection and sizing. Both current injection and field analysis can be achieved by either galvanic or inductive coupling. First, we will consider Alternating Current Field Measurement (ACFM) techniques which use noncontacting mapping of the magnetic field produced by the current distribution inside a specimen. In ACFM the current injection can be implemented through either inductive or galvanic coupling. Second, we are going to discuss potential drop (PD) techniques which rely on galvanic sensing of the electric potential distribution on the surface of the specimen to detect and quantitatively characterize variations in specimen geometry and surface-breaking and near-surface cracks. Most PD techniques rely on galvanic injection, though the less known induced current potential drop (ICPD) technique uses eddy currents generated below the surface of the specimen by inductive means.

PD techniques will be further divided into direct-current potential drop (DCPD) and alternating current potential drop (ACPD) techniques depending on whether the penetration depth of the injected current is determined by the specimen and electrode geometry or the electromagnetic skin effect. This rather flexible separation between AC and DC inspection is necessary because in reality the underlying physics depends on geometrical and material parameters just as much as on the inspection frequency. Actually, the transition frequency ( $\approx 0.1$  Hz) between what is conventionally considered AC and DC regimes is rather meaningless in this context. For example, small-scale inspection of nonmagnetic components might still be safely in the quasi-static or DC range even at inspection frequencies as high as a few hundred Hz.



#### 4.1 Alternating Current Field Measurement

Alternating Current Field Measurement (ACFM) techniques rely on noncontacting mapping of the magnetic field produced by the current distribution inside a specimen. Figure 65 illustrates the basic operational principle of ACFM. Current can be injected into the specimen by either inductive or galvanic coupling. In the latter case direct current injection could be also used in combination with magnetic sensors, such as Hall detectors, capable of measuring static magnetic fields. However, most often the ACFM method is used in AC mode for sizing surface breaking cracks in metals by exploiting the fact that the current flowing below the surface can be squeezed into a thin skin depth by increasing the inspection frequency, which produces enhanced crack detection sensitivity [118-120].

Current injection is configured so that the local current density distribution in the inspected region is more or less unidirectional and uniform over the surface of an intact specimen. As shown in Figure 66, in the presence of a surface-breaking or near-surface crack this current distribution is perturbed and the resulting magnetic field perturbation can be exploited for crack detection and sizing. Let us assume that the  $x$  or axial direction of a Cartesian coordinate system is chosen to be aligned with the crack and the injected current flows in the  $y$  or transverse

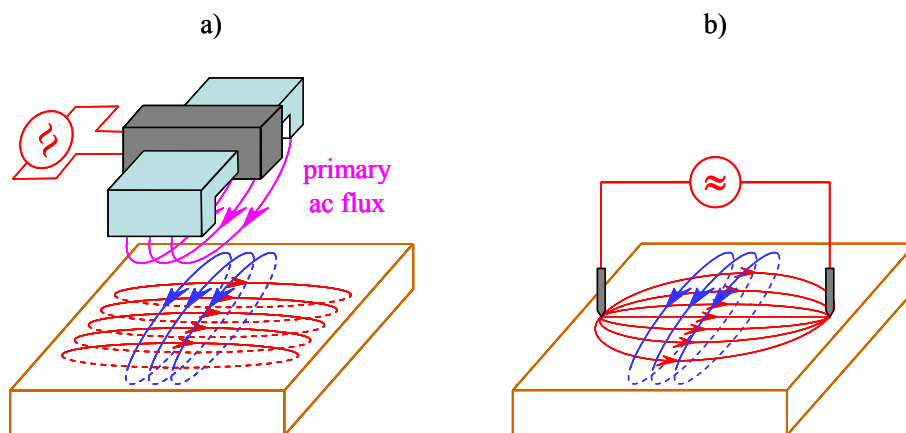


Figure 65 Operational principle of alternating current field measurement with (a) inductive and (b) galvanic current injection.

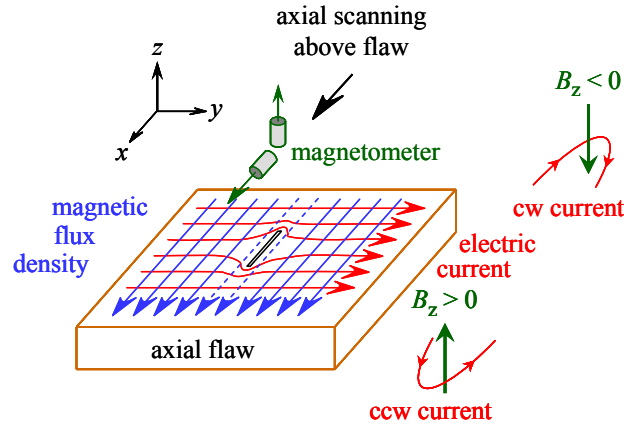


Figure 66 Field perturbation caused by a surface-breaking crack in ACFM inspection.

direction. Regardless whether magnetic or galvanic injection was used to produce the transverse current in the specimen, in the absence of a crack the magnetic flux density is directed strictly in the axial direction and exhibits negligible transverse  $B_y$  or normal  $B_z$  components. In the presence of a surface-breaking or near-surface crack the otherwise strictly transverse current distribution  $J_y$  will assume both axial  $J_x$  and normal  $J_z$  components as the current flows around the tips of the crack and under its depth, respectively.

Figure 67 illustrates the magnetic flux density perturbation caused by a surface-breaking crack in ACFM inspection. As a result of the curvature of the current path produced by the crack, the measured external magnetic flux density will exhibit strong normal components  $B_z$  of opposite sign at the tips of the crack as shown in Figure 67a. Figure 67b shows how the otherwise uniform axial magnetic flux density  $B_{x0}$  increases at the tips due to the higher current density there and exhibits a reduction above the center of the crack. It is common practice to plot the normal magnetic flux density  $B_z$  as a function of the axial component  $B_x$  as shown in Figure 67c, which yields a crack signature of easily recognizable “butterfly” shape (the corresponding loci are indicated by dots and open circles for easier identification).

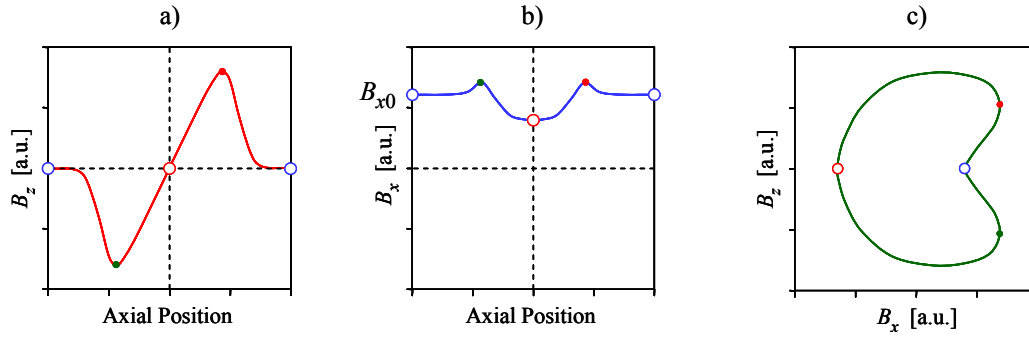


Figure 67 Magnetic flux density perturbation caused by a surface-breaking crack in ACFM inspection.

The ACFM technique has been used extensively in industry to successfully detect and size defects where traditional techniques have been unsuccessful [120]. The main advantages of this method over conventional eddy current inspection lie in its ability to conduct testing through thick coatings without layer removal, although the sensitivity inevitably reduces with increasing coating thickness. It provides crucial size and depth information on cracks and is less susceptible to boundary effects than conventional inspection techniques. It is particularly useful under tough field conditions that ACFM inspection requires no elaborated instrument calibration before testing and it is significantly faster than other conventional NDT methods. Because of its noncontacting nature and insensitivity to lift-off variations, it is also suitable for testing of components at elevated temperatures.

The main disadvantages of ACFM lie in its relatively modest sensitivity, high susceptibility to false alarms caused by geometrical variations, and limitations by access, location and wall thickness due to the large size of the sensor. ACFM is sensitive to surface breaking defects only and, of course, the specimen must be electrically conductive, but variations in magnetic properties, e.g., in welded zones of ferromagnetic steels, could lead to testing problems. This method is also limited by the need to identify the flaw orientation in advance to testing and often cannot be used because of the inherently large dimensions of ACFM sensors. Depth sizing

algorithms based on canonical models, such as an isolated semi-elliptical crack, are available in the literature, but may provide misleading results in the presence of multiple defects.

#### 4.2 Direct Current Potential Drop

Direct current (DC) electric resistance measurements have been used to measure the wall thickness of metal plates, pressure vessels, boilers, tubes, ship hulls, and castings since the 30's [121]. This simple technique was first found applicable for crack detection after a surface crack interposed between the electrodes had been claimed to be the reason for anomalous readings during wall thickness testing. Figure 68 illustrates the operational principle of potential drop (PD) measurement with galvanic current injection. The current is injected and drained at two points and the potential difference between two other points is measured. Usually spring-loaded electrodes are used, but permanently installed welded electrodes are also widely used for in-situ monitoring. Because of the inherently high contact resistance between the measuring electrodes and the specimen to be tested, the PD method is always realized as a four-point resistance measurement. A given current  $I$  is driven between the two outer electrodes and the resulting potential drop  $\Delta V$  between the two inner electrodes is measured by a high input resistance voltmeter to avoid any spurious voltage drop due to the uncertain contact resistance between the electrodes and the specimen.

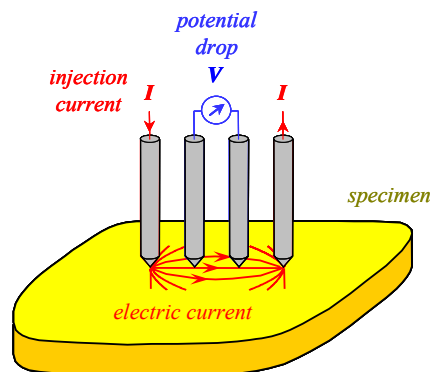


Figure 68 Operational principle of potential drop (PD) measurement with galvanic current injection.

Generally, the transfer resistance measured in such four-point configuration is

$$R = \frac{\Delta V}{I} = \rho \Lambda, \quad (57)$$

where  $\rho$  denotes the resistivity of the specimen and  $\Lambda$  is a resistance coefficient having the units of inverse length. Without a crack,  $\Lambda$  depends only on the separation of the electrodes and the thickness of the plate. In the presence of a crack,  $\Lambda$  also depends on the length, depth, and orientation of the crack. For a given electrode arrangement, material resistivity and excitation current, any change in the observed potential drop will represent a corresponding change in the geometry of the specimen including the crack. A calibration function must be obtained by analytical, numerical, or experimental means on a case to case basis in order to interpret the measured potential difference in terms of the varying geometrical parameter.

First, let us consider the static electric current distribution in a thin plate. Figure 69 shows a schematic diagram of DCPD measurement in a thin-plate with in-line electrode configuration. The plate thickness  $t$  is assumed to be much smaller than the half-separation  $a$  between the injection electrodes. The potential distribution is most easily calculated by superposition from the individual cylindrical potential distributions of the source  $I^{(+)}$  and sink  $I^{(-)}$  currents as illustrated in Figure 70a. The cylindrical electric field of a single current source  $I$  can be calculated from Gauss' law as follows

$$E(r) = \rho J(r) = \frac{I \rho}{2 \pi r t}, \quad (58)$$

so that the potential distribution is

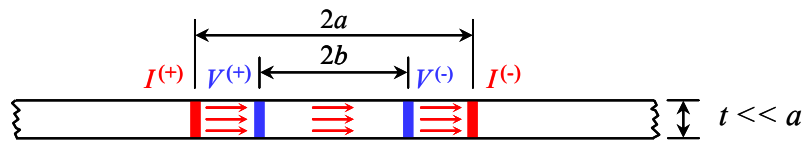


Figure 69 A schematic diagram of in-line DCPD measurement in a thin-plate.

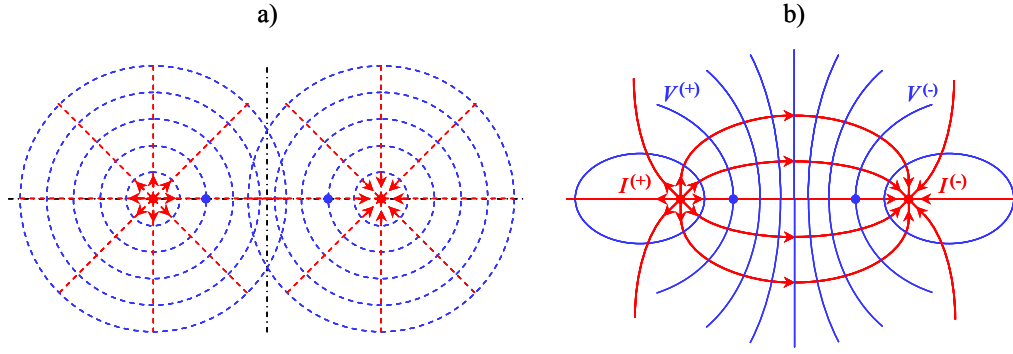


Figure 70 Potential distributions in a thin-plate for (a) separate source and sink and (b) the combined field.

$$V(r) = \int_r^{\infty} E(r) dr = -\frac{I \rho}{2 \pi t} \ln r + V_{\infty}, \quad (59)$$

where  $V_{\infty}$  is an arbitrary constant representing the potential far away from the source. The potential difference  $\Delta V = V^{(+)} - V^{(-)}$  between the two sensing points separated by distance  $2b$  can be calculated using superposition as illustrated in Figure 70b. In this case, the previously defined resistance coefficient

$$\Lambda_{\text{thin}} = \frac{1}{\pi t} \ln \frac{a+b}{a-b}, \quad (60)$$

turns out to be inversely proportional to the plate thickness  $t$ .

Next, let us consider the static electric current distribution in a half-space. Figure 71 shows a schematic diagram of the potential distribution in a half-space for (a) separate source and sink and (b) the combined field. The plate thickness is assumed to be much larger than the separation

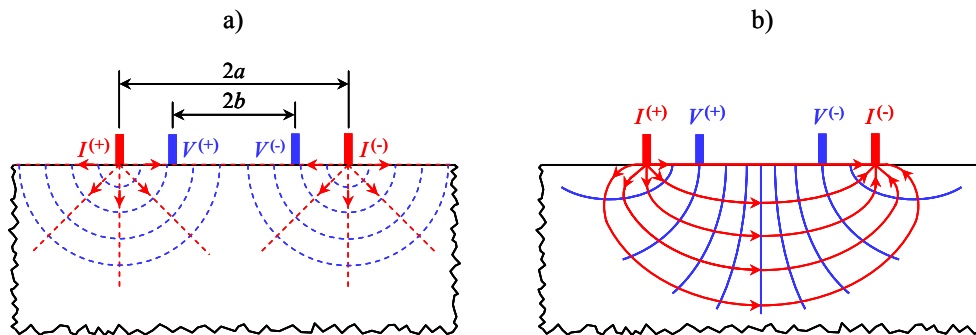


Figure 71 Potential distributions in a half-space for (a) separate source and sink and (b) the combined field.

between the injection electrodes. First, the electric potential distribution of the individual, this time spherical, contributions of the source  $I^{(+)}$  and sink  $I^{(-)}$  currents are calculated as illustrated in Figure 71a. The spherical electric field of a single current source  $I$  can be calculated from Gauss' law as follows

$$E(r) = \rho J(r) = \frac{I \rho}{2 \pi r^2}, \quad (61)$$

so that the potential distribution is

$$V(r) = \int_r^\infty E(r) dr = \frac{I \rho}{2 \pi r} + V_\infty \quad (62)$$

and the potential difference  $\Delta V = V^{(+)} - V^{(-)}$  between the two sensing points can be calculated again using superposition as illustrated in Figure 71b. The resulting resistance coefficient decreases with increasing electrode separation as follows

$$\Lambda_{\text{thick}} = \frac{1}{\pi} \left[ \frac{1}{a-b} - \frac{1}{a+b} \right]. \quad (63)$$

Figure 72a shows a schematic diagram of in-line DCPD in an intact finite-thickness plate. The boundary conditions on both the top and bottom surfaces of the plate require that the normal component of the electric field vanish. This condition can be satisfied by the application of an infinite series of point sources in an unbounded medium [122]. The resulting potential is

$$V(r) = \sum_{n=-\infty}^{\infty} \frac{I \rho}{2 \pi [r^2 + (2nt)^2]^{1/2}}, \quad (64)$$

and the resistance coefficient for an intact finite-thickness plate can be calculated from

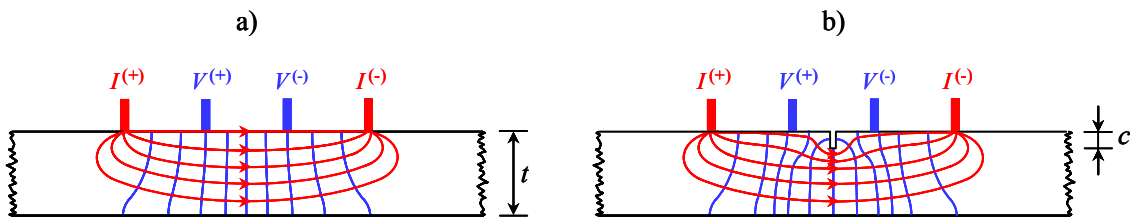


Figure 72 Schematic diagrams of in-line DCPD in a finite-thickness plate (a) without and (b) with a crack.

$$\Lambda = \frac{1}{\pi} \sum_{n=-\infty}^{\infty} \left[ \frac{1}{[(a-b)^2 + (2nt)^2]^{1/2}} - \frac{1}{[(a+b)^2 + (2nt)^2]^{1/2}} \right]. \quad (65)$$

Figure 73a shows the resistance coefficient  $\Lambda$  of an intact plate as a function of normalized thickness  $t/a$  for an electrode separation ratio of  $a = 3b$ . At small and large values of the normalized thickness the finite-plate solution of Eq. (65) quickly approaches the thin-plate and thick-plate asymptotes, respectively. In the transition region around  $t/a \approx 1$  the resistance coefficient is a more complicated function of the electrode “aspect” ratio  $a/b$ . Figure 73b shows the finite element prediction for the resistance coefficient of a cracked plate  $\Lambda_c$  containing an infinite notch of depth  $c$  after normalization to the intact value of the same plate. As one would expect, a relatively shallow slot ( $c/t \ll 1$ ) can be much better detected when the electrode separation is relatively small with respect to the plate thickness ( $a/t < 1$ ).

One of the main disadvantages of DCPD is the relatively low transfer resistance  $R = \Delta V/I$  caused by the uninhibited spread of the injected current constrained only by the contours of the specimen under test and the electrode separation. As a result, typically injection currents on the order of 10 A must be used to produce DC voltage differences that can be measured sufficiently

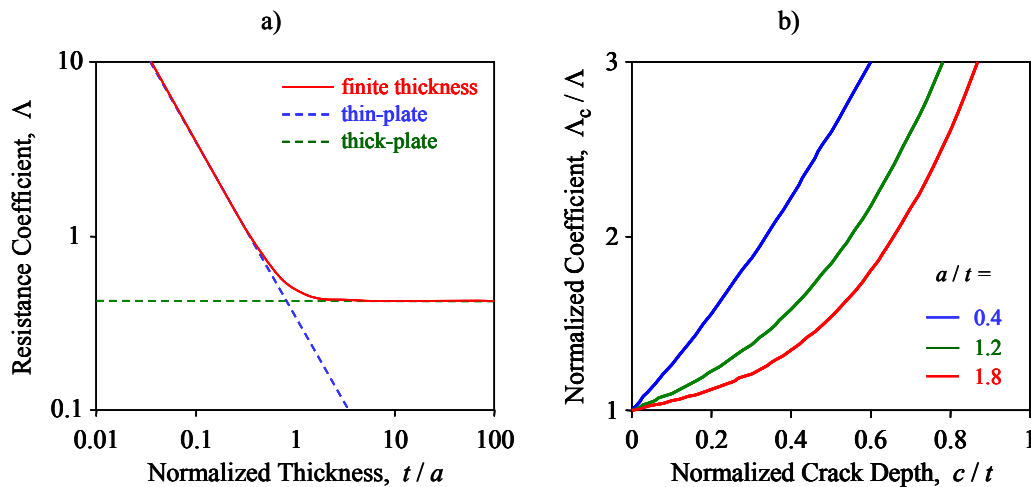


Figure 73 Resistance coefficient as a function of normalized plate thickness for (a) an intact plate and for (b) a cracked one containing an infinite notch after normalization to the intact value ( $a = 3b$ ).



accurately, especially on larger pieces [123]. Another problem is that comparable thermoelectric voltages might be produced between the sensing electrodes if the two junctions happen to have a slight temperature difference. In order to mitigate the thermoelectric effect, it is customary to make measurements with opposite injected current polarity and subtract the measured potential drops. Assuming that the polarity change can be implemented fast enough for the temperature distribution to change significantly, the spurious thermoelectric voltages cancel out.

#### 4.3 Alternating Current Potential Drop

The fundamental problem with DCPD inspection is due to the fact that the penetration depth of the injected current can be controlled only through the electrode separation. This drawback can be avoided by alternating current potential drop (ACPD) measurements at sufficiently high inspection frequencies where the penetration depth is determined by the electromagnetic skin depth. ACPD measurement is an electromagnetic technique for non-destructive testing, which has been employed for decades to monitor crack growth [124, 125], to estimate the depth of surface-breaking defects [126, 127], or simply to evaluate material properties such as conductivity or permeability [128, 129]. This method offers much higher sensitivity to the crucial near-surface layer than DCPD inspection, though on the flip side it is susceptible to magnetic permeability variations in ferritic steels and other ferromagnetic materials.

Figure 74 illustrates the current distribution in intact and cracked specimens using (a) DCPD and (b) ACPD inspection. In the former case the injected current spreads out through the

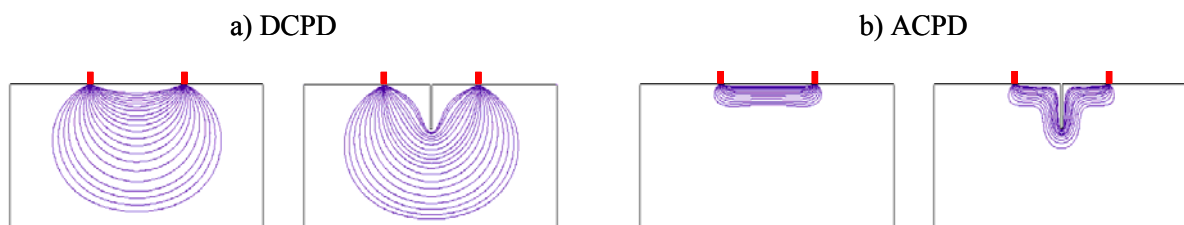


Figure 74 Current distribution in intact and cracked specimens using (a) DCPD and (b) ACPD inspection.

whole cross section of the specimen limited only by the electrode separation, while in the latter case the penetration depth is readily controlled by the inspection frequency through the electromagnetic skin depth. The main advantages of ACPD over DCPD are higher transfer resistance, therefore lower injection current requirement on the order of 10-100 mA only, no spurious influence from thermoelectric effects, easy control of the penetration depth through changing the inspection frequency, and higher sensitivity to the crucial near-surface layer. One distinct disadvantage of the ACPD technique is the susceptibility of the measurement to magnetic permeability variations.

Exact analytical solutions are available in the literature for the frequency-dependent transfer impedance  $Z = \Delta V/I$  of a thin plate [130] and a semi-infinite half-space representing a very thick plate [131]. Figure 75 shows analytical results for the transfer resistance illustrating the skin effect in thin nonmagnetic plates of (a) various conductivity at  $t = 2$  mm and (b) thickness at  $\sigma = 50$  %IACS for an in-line electrode of  $a = 20$  mm and  $b = 10$  mm. The fairly complex exact analytical solution can be approximated in the thin-skin approximation by replacing the plate thickness  $t$  of the thin-plate solution given in Eq. (60) by a generalized frequency-dependent skin depth  $T(\omega)$  to calculate the resistance coefficient as follows

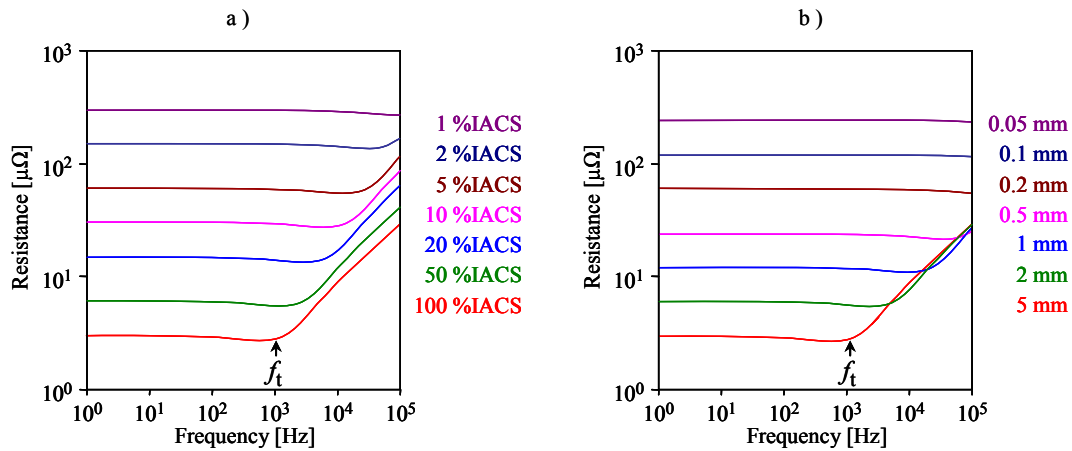


Figure 75 Resistance spectra in thin nonmagnetic plates of (a) various conductivity at  $t = 2$  mm and (b) thickness at  $\sigma = 50$  %IACS for an in-line electrode of  $a = 20$  mm and  $b = 10$  mm.

$$\Lambda(\omega) = \frac{\text{Re}\{Z\}}{\rho} = \frac{1}{\pi T(\omega)} \ln \frac{a+b}{a-b}. \quad (66)$$

The skin depth can be approximated by the smaller of the actual plate thickness  $t$  and the previously defined electromagnetic standard penetration depth  $\delta = \sqrt{\rho/(\pi f \mu)}$ , i.e.,  $T = \min\{t, \delta\}$ . At low frequencies,  $T(\omega) = t$  and the approximate solution asymptotically approaches the DC solution. At high frequencies,  $T(\omega) = \delta$  and the approximate solution asymptotically approaches the thin-skin AC solution

$$\lim_{f \rightarrow \infty} \Lambda \approx \sqrt{\frac{f \rho \mu}{\pi}} \ln \frac{a+b}{a-b}. \quad (67)$$

The transition between the low- and high-frequency behaviors occurs when  $\delta(f_t) \approx t$ , i.e., the transition frequency can be approximated as

$$f_t = \frac{1}{\pi \mu_0 \sigma t^2}. \quad (68)$$

It should be mentioned that, just like in the case of the previously discussed ACFM method, ACPD measurements can be also conducted using inductive injection, which is referred to as induced current potential drop technique in the literature [132, 133]. The primary application of ACPD measurements is crack sizing. Numerous inversion methods are available in the literature to relate the measured frequency-dependent transfer resistance to crack parameters [134-138]. Other typical applications include weld penetration measurement [139], case hardening measurement [140], corrosion/erosion assessment [141], and many others.

## 5 Special Inspection Methods

In this section we will review three emerging special EM NDE methods, namely microwave, dielectric, and thermoelectric inspections. These methods are less frequently used in everyday practice than the previously discussed eddy current and current field mapping methods, mainly

because they are limited to a smaller range of materials and are sensitive to a narrower class of damage mechanisms. Still, they well supplement those other more popular inspection methods and offer great advantages over them in some niche applications, therefore any review of electromagnetic NDE methods would not be complete without them.

### 5.1 Microwave Inspection

Figure 76 illustrates the main regions of the electromagnetic spectrum in terms of frequency, wavelength, and energy. Such multiple-parameter characterization of electromagnetic waves is customary because different fields use different description for essentially the same wave property. Eddy current inspection is conducted in the radio frequency range where cyclic frequency is used exclusively to characterize harmonic content. Microwave inspection is based on high-frequency electromagnetic radiation in the 1-1,000 GHz range, though no strict limits can be defined [142-145]. This frequency range corresponds to a wavelength range of 0.3-300 mm in a vacuum or in air. More recently, even higher frequency terahertz (THz) imaging has been adopted for nondestructive evaluation applications in aerospace and other areas [146-148].

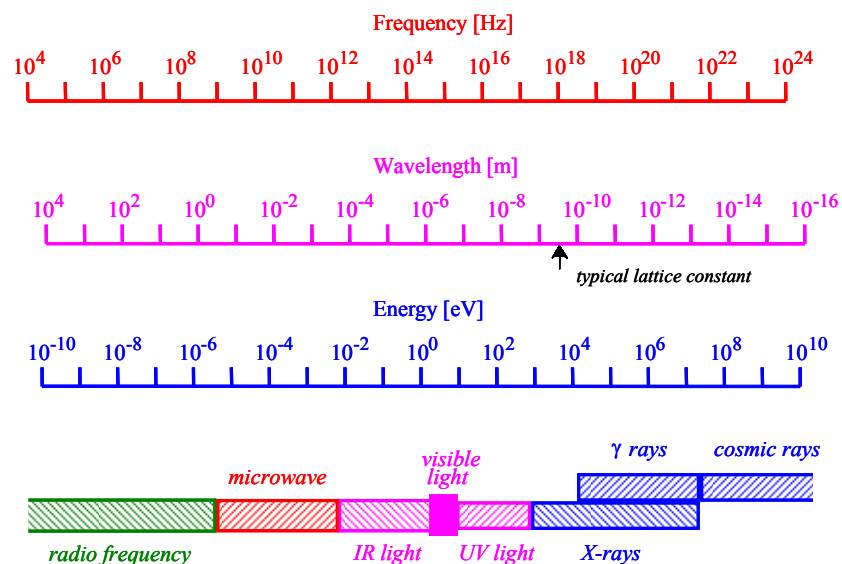


Figure 76. Electromagnetic spectrum in terms of frequency, wavelength, and energy.

Throughout the infrared, visible, and ultraviolet light regions wavelength is the parameter of choice to characterize the electromagnetic radiation. Of course the electromagnetic wavelength  $\lambda = c/f$  depends on the velocity  $c$  as well as on the cyclic frequency  $f$ , therefore the wavelength in free space is used for identification purposes even when propagation might occur in various materials. At even shorter wavelength, it is customary to refer to the energy of photons  $E = h\nu$ , where  $\nu$  is the frequency (instead of  $f$  which is traditionally used in the radio frequency range) and  $h \approx 6.63 \times 10^{-34}$  Js is the Planck constant. It is also customary to express the energy of the photon in electronvolt ( $\approx 1.6 \times 10^{-19}$  J) as it is shown by the third scale in Figure 76.

Microwave inspection has been used as an NDE tool for at least half a century, but has remained a relatively limited special method. This section will provide only a very brief introduction to microwave NDE and for more details the reader is referred to excellent monographs and reviews available on the subject [142-145]. The main applications of microwave NDE techniques include (i) thickness measurement of coatings, single- and multi-layer dielectric slabs, laminated composites made of plastics, ceramics and any other type of dielectric materials, (ii) detection and localization of disbonds, delaminations and voids, (iii) inspection of glass-fiber-reinforced epoxy-matrix composites, (iv) moisture content assessment, (v) porosity assessment in dielectrics, (vi) impact damage assessment in laminated composites, and (vii) detection of surface-breaking cracks under dielectric coatings.

Figure 77 shows the most common far-field measurement configurations used in microwave NDE, namely (a) reflection, (b) transmission, and (c) scattering modes. The reflection mode of operation shown in Figure 77a relies on a single antenna used as both transmitter and receiver (this mode of operation corresponds to monostatic and pulse-echo modes in radar and ultrasonic terminology, respectively). A circulator has three ports and allows energy

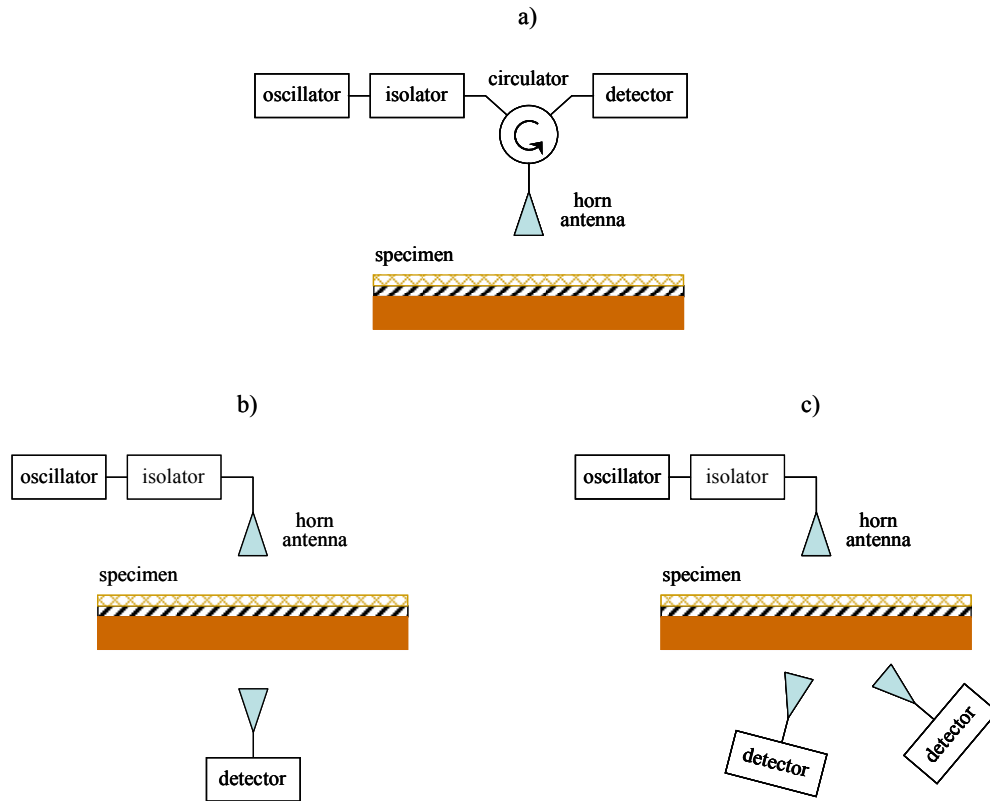


Figure 77 Most common far-field measurement configurations used in microwave NDE: (a) reflection, (b) transmission, and (c) scattering.

transfer between any two ports only in a counter clockwise rotation, thereby directing the driving signal from the oscillator to the antenna and the received target reflection from the antenna to the detector. The isolator placed between the oscillator and the circulator prevents internal reflections from getting back into the oscillator and causing interference.

The transmission mode of operation shown in Figure 77b uses separate transmitter and receiver antennas (this mode of operation corresponds to bistatic and pitch-catch modes in radar and ultrasonic terminology, respectively). In this case there is no need for a circulator. On the flip side, transmission mode inspection requires two-sided access to the component to be tested, which severely limits the application of this technique in practice. Finally, the scattering mode of operation shown in Figure 77c uses separate transmitter and receiver antennas just like the reflection mode, but rather than detecting the direct transmission, which is attenuated by the

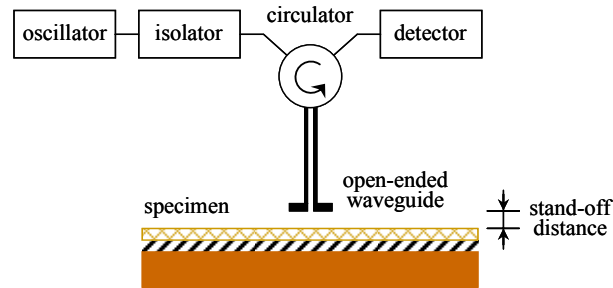


Figure 78 A schematic diagram of near-field microwave inspection.

presence of inhomogeneities, therefore produces a shadow image of negative contrast, it relies on scattering from inhomogeneities and flaws at oblique angles, therefore produces a bright image of positive contrast.

In spite of all the advantages of far-field microwave measurements, its sensitivity and resolution leaves much to be desired and can be significantly improved by placing the specimen to be tested in the near-field of an open-ended waveguide as shown in Figure 78. In such near-field microwave inspection the specimen acts as a terminator impedance at the end of the otherwise open waveguide and produces standing waves inside the waveguide that can be measured with excellent signal-to-noise ratio. Local variations in the electromagnetic impedance of the specimen can be used to construct a high-resolution image as the specimen is scanned relative to the waveguide [149-153]. Figure 79 shows schematic diagrams of microwave inspection of (a) a layered sample and (b) corrosion damage under coating. One disadvantage of

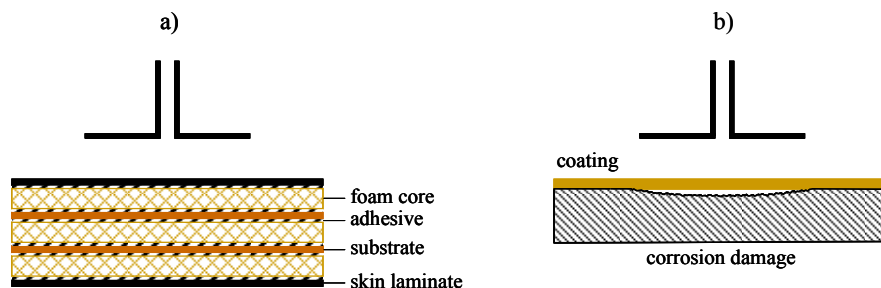


Figure 79 Schematic diagrams of microwave inspection of (a) a layered sample and (b) corrosion damage under coating.

this inspection method is that in order to achieve good sensitivity and imaging resolution the tip of the waveguide has to be closer to the inspected object than the characteristic transverse dimension of the waveguide, which is obviously rather impractical in some cases.

As an example, Figure 80 shows (a) the optical image of a 40 mm  $\times$  40 mm area of rust on a steel plate and (b) its microwave image under 0.267 mm of paint taken at 24 GHz from 12.5 mm standoff distance [154]. Detection of the rusted spot behind the paint is made difficult by the fact that both the paint ( $\epsilon_r \approx 3 - 0.1 i$ ) and rust ( $\epsilon_r \approx 2.7 - 0.03 i$ ) exhibit low permittivity and dielectric loss and that their dielectric properties are quite similar. Still, the rusted area is clearly visible in the center of the microwave image shown in Figure 80b.

As most of the microwave energy hitting a dielectric material is absorbed, microwave radiation can be also used as a heat source in thermography as shown in Figure 81. Since the dissipated energy is necessarily small, the best detection sensitivity can be achieved by phase-sensitive lock-in thermography. The basic arrangement is identical to that of near-field microwave inspection previously shown in Figure 78 with the exception that the oscillator is modulated at a frequency of 10-100 Hz. A high-speed infrared camera can be used to map the resulting temperature oscillations. The output signal of the camera is measured pixel by pixel

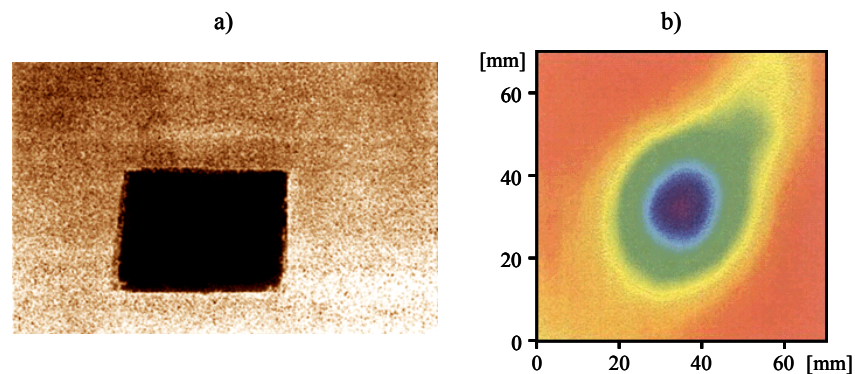


Figure 80 (a) Optical image of a 40 mm  $\times$  40 mm area of rust on a steel plate and (b) its microwave image under 0.267 mm of paint taken at 24 GHz from 12.5 mm standoff distance. From Qaddoumi et al., 1997 [154].



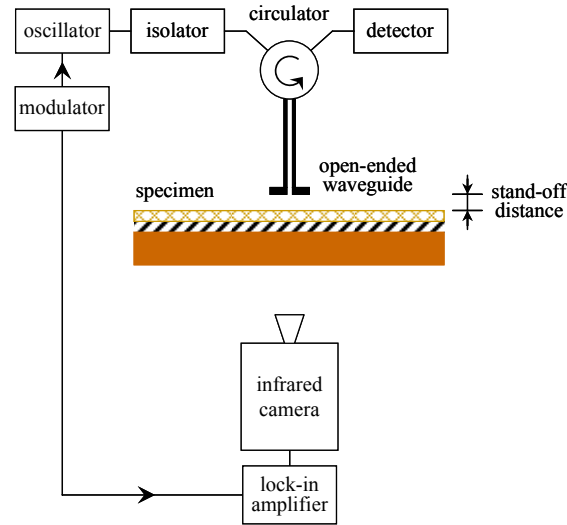


Figure 81 A schematic diagram of lock-in thermography with microwave excitation.

using a digital lock-in amplifier. In order to conduct a two-phase lock-in measurement, the frame frequency has to be at least four times faster than the modulation frequency. The spatial resolution of lock-in thermography can be on the order of  $100\ \mu\text{m}$  and the temperature resolution can reach  $0.1\ ^\circ\text{C}$ .

As an example, Figure 82 shows (a) a 30-GHz microwave raster image of two bonded glass fiber-reinforced polymer plates with some defects and (b) its lock-in thermographic phase image ( $50\ \text{mm} \times 75\ \text{mm}$ ) [155]. In addition to an artificially induced  $150\text{-}\mu\text{m}$ -thick air gap marked as “delamination” on the right side, there are three small bonding defects on the left side of the specimen. The line pattern across the microwave image is caused by the texture of the glass

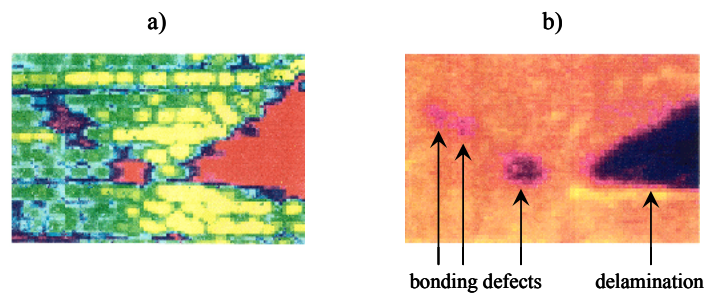


Figure 82 (a) Microwave raster image of two bonded glass fiber-reinforced polymer plates with artificially induced air gap and (b) its lock-in thermographic phase image ( $50\ \text{mm} \times 75\ \text{mm}$ ). From Diener, 1995 [155].

fabric. Compared to the microwave image, the lock-in thermographic phase image shows a smoother image with negative contrast.

### 5.2 Dielectric Inspection

Dielectric measurements are widely used for quantitative NDE and process-control of nonconducting materials [156]. The underlying physical phenomenon behind these techniques is electric polarization. The total electric flux density  $\mathbf{D} = \epsilon_0 \mathbf{E} + \mathbf{P}$  includes the electric polarization  $\mathbf{P}$  which is defined as the total electric polar moment in a unit volume

$$\mathbf{P} = \frac{\sum \mathbf{p}_e}{V} = \chi_e \epsilon_0 \mathbf{E}, \quad (69)$$

where  $\mathbf{p}_e = Q \mathbf{d}$  is the electric dipole moment of individual molecules produced by separating opposite charges of  $Q$  by a vector distance  $\mathbf{d}$ . The electric polarization  $\mathbf{P}$  is usually linearly proportional to the external electric field  $\mathbf{E}$  as given in Eq. (69), where  $\chi_e$  is the so-called electric susceptibility so that  $\mathbf{D} = \epsilon_0 \epsilon_r \mathbf{E}$  and the relative permittivity is  $\epsilon_r = 1 + \chi_e$ .

Electric polarization can take two basic forms. First, electric dipoles can form under the influence of an external electric field as shown schematically in Figure 83. In an otherwise nonpolar medium the centers of positive and negative charges coincide until they are separated by the electric force  $\mathbf{F}_e = \pm Q \mathbf{E}$  pulling them away from each other. Second, randomly oriented pre-existing electric dipoles can align themselves with the external electric field as shown schematically in Figure 84. In a medium consisting of polar molecules, like water, the centers of positive and negative charges are inherently separated, but the individual dipole moments  $\mathbf{p}_e$  are completely randomized, therefore there is no macroscopic polarization  $\mathbf{P}$ . Under the influence of the external electric field  $\mathbf{E}$  a twisting torque  $\mathbf{T}_e = \mathbf{p}_e \times \mathbf{E}$  acts on the dipoles and aligns them with the external electric field to the extent allowed by thermal vibrations.

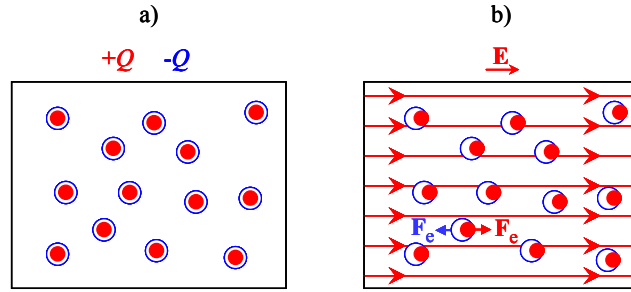


Figure 83 Dipole formation under the influence of an external electric field.

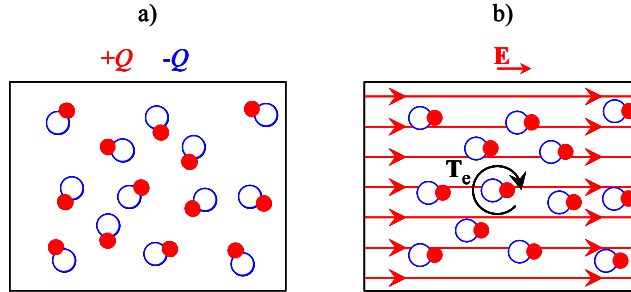


Figure 84 Dipole alignment under the influence of external electric field.

The dielectric properties of materials can be most conveniently assessed between a few Hz and a few MHz using capacitive coupling. The basic definition of capacitance between two electrodes is  $C = Q/V$ , where  $Q$  is the stored charge and  $V$  is the potential difference between the electrodes. For our purposes, the differential form of this definition

$$I = \frac{dQ}{dt} = C \frac{dV}{dt} \quad (70)$$

is more suitable. The complex admittance of a capacitance is then

$$\tilde{Y} = \frac{I}{V} = i\omega C. \quad (71)$$

Let us consider the simplest arrangement formed by two parallel electrodes with the dielectric between them as shown previously in Figure 2. The electric flux density is  $D \approx Q/A$ , where  $A$  is the surface area of the two parallel electrodes. For an ideal lossless dielectric, the electric field is simply  $E = D/\epsilon$  so that the potential difference between the electrodes separated by distance  $\ell$  is  $V = E\ell$ , therefore the capacitance can be approximated by neglecting the effects of stray electric

field at the edges as  $C = \epsilon A / \ell$ , where  $\epsilon = \epsilon_0 \epsilon_r$  is the electric permittivity.

Some dielectrics exhibit significant electric conductivity  $\sigma$  that produces a complex admittance

$$\tilde{Y} = i\omega C + G = i\omega\tilde{C}, \quad (72)$$

where the conductance  $G = \sigma A / \ell$ . Under such conditions the capacitance itself can be considered complex  $\tilde{C} = \tilde{\epsilon} A / \ell$  with the otherwise real electric permittivity replaced by a complex material parameter  $\tilde{\epsilon}(\omega) = \epsilon - i\sigma/\omega$  that incorporates both real permittivity and conductivity effects. In a lossy dielectric both the real permittivity  $\epsilon = \epsilon(\omega)$  and conductivity  $\sigma = \sigma(\omega)$  exhibit significant frequency dependence and it is customary to write the electric permittivity in a more general complex form as follows

$$\tilde{\epsilon}(\omega) = \epsilon'(\omega) - i\epsilon''(\omega), \quad (73)$$

where  $\epsilon'$  and  $\epsilon''$  are the real and (negative) imaginary components of the complex permittivity, respectively. Finally the loss factor  $D$  is defined as  $D = \tan\delta = \epsilon''(\omega)/\epsilon'(\omega)$ , where  $\delta$  is the loss angle, i.e., the deviation of the admittance phase angle from its ideal  $90^\circ$  value in lossless dielectrics.

Figure 85 illustrates the frequency dependence of the real and imaginary parts of the electric permittivity in a typical dielectric over a very wide frequency range from the audio regime up to approximately the end of the UV light regime. Below the low-frequency end of this range, the real permittivity  $\epsilon'$  is essentially constant and the imaginary permittivity  $\epsilon'' = \sigma/\omega$  is inversely proportional to frequency as pointed out earlier. As the frequency increases, numerous relaxation processes influence the complex electric permittivity of materials. At each relaxation frequency, the corresponding polarization process loses its mobility, therefore the real permittivity drops. Below this transition frequency, the polarization process is essentially free,

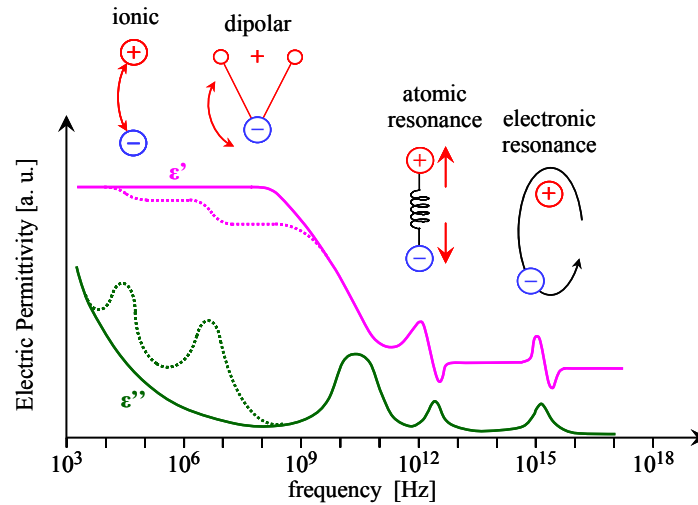


Figure 85 Various relaxation processes influencing the complex electric permittivity of materials.

therefore lossless, while above it the polarization process is frozen rigid, therefore becomes lossless again. In the vicinity of the relaxation frequency the dielectric loss reaches its maximum, which can be exploited for materials characterization purposes.

The frequency dependence of the real permittivity can cause very significant dispersion in electromagnetic wave propagation. For example, the relative permittivity of water at low frequencies is very high at  $\epsilon_r \approx 80$ . At the same time, the optical refractive index of water is only  $n \approx 1.33$  which indicates that at the frequencies of visible light the relative permittivity dropped to  $\epsilon_r \approx 1.8$ , an approximately fiftyfold reduction.

Figure 86a shows the configuration of a simple capacitive probe with parallel plane electrodes. By measuring the potential difference  $V_m$  between the electrodes and knowing the generator voltage  $V_g$  and resistance  $R_g$  the complex admittance of the probe can be calculated, which then can be further processed to assess the complex electric permittivity of the material under test. Of course this simplistic arrangement suffers from numerous drawbacks that can be relatively easily eliminated using more sophisticated probe designs and electronic processing.

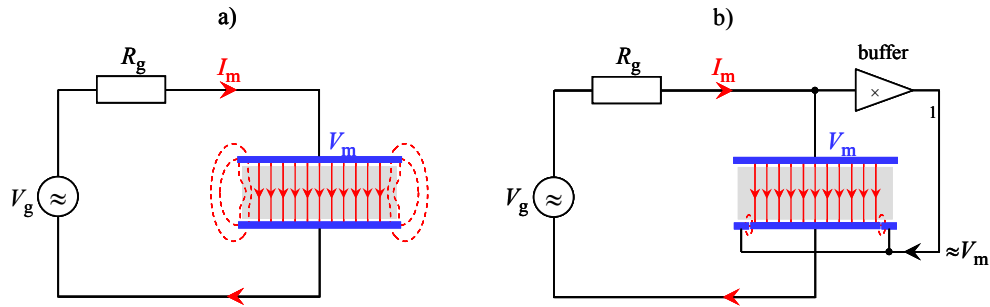


Figure 86 Capacitive probes with parallel plane electrodes; (a) basic sensor and (b) sensor with guard electrodes.

As an example, Figure 86b shows a dielectric sensor with guard electrodes. The guard ring around the edges of the “cold” electrode is kept at the same voltage  $V_m$  as the “hot” electrode by a high-input-impedance buffer amplifier of unity gain. This modification eliminates the uneven electric field distribution at the edges of the capacitive cell and the associated experimental errors. In practice, often only single-sided access is allowed, in which case stray-field capacitive sensors can be used as shown in Figure 87. The penetration depth of the interrogating electric field can be controlled by the spacing of the periodic electrode layout [157].

The complex dielectric permittivity is directly related to other material properties, such as moisture content, concentration of impurities and additives, density, aging status, etc. Analysis of spatial, temporal, and temperature variations of these properties offers valuable insights into the underlying physical phenomena. Monitoring of curing in polymer-matrix composites [158] and the detection of internal damage [159] are typical examples for application of dielectrometry in NDE. This cost-effective technique can be used for rapid damage screening, regularly scheduled inspection, or as a permanently installed sensor network for in-situ monitoring of composite components and structures.

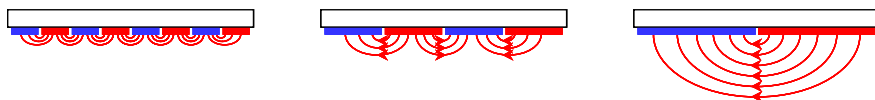


Figure 87 Single-sided capacitive inspection using stray-field electrode configuration.

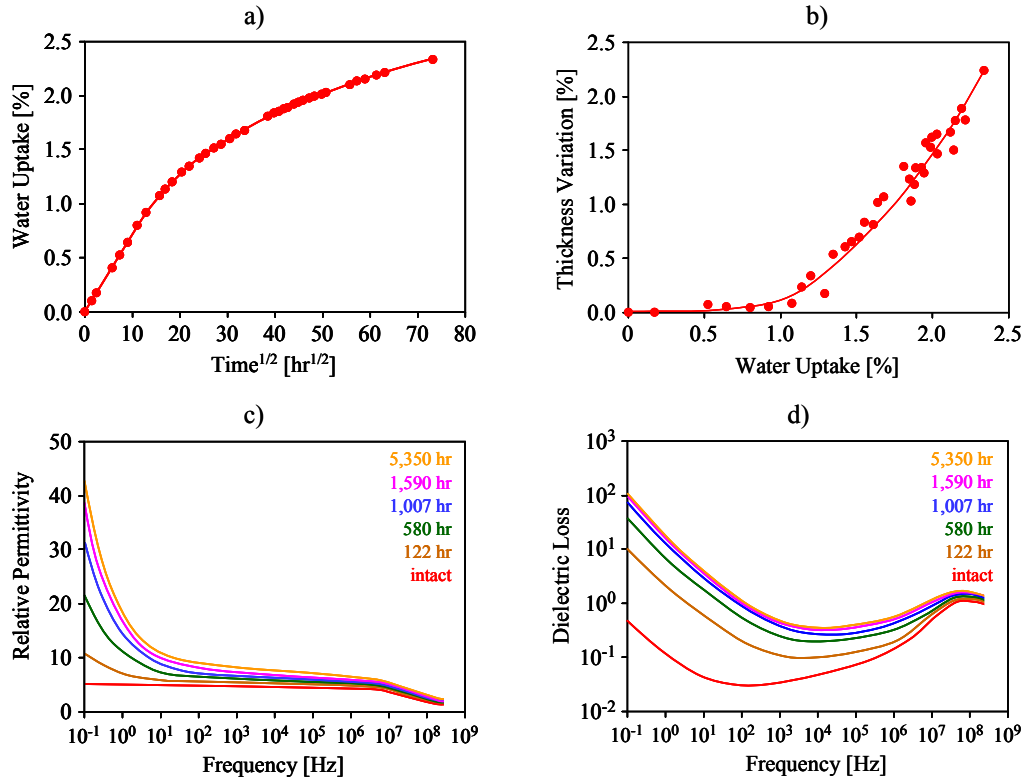


Figure 88 Illustration of how (a) water uptake increases the (b) volume, (c) relative permittivity, and (d) dielectric loss with time in an adhesively bonded composite. From Pethrick et al., 2002 [160].

Dielectric techniques are particularly well suited for studying the sorption and desorption of moisture in adhesively bonded composite structures because of the earlier mentioned very high electric permittivity of water. Figure 88 illustrates how water uptake increases both the relative permittivity and dielectric loss in an adhesively bonded composite over a very wide frequency range [160]. Most of the change in the relative permittivity occurs at very low frequencies below 10 Hz. The dielectric loss also changes most at low frequencies, but significant contrast between dry and partially saturated composite is exhibited up to 10 MHz.

### 5.3 Thermoelectric Inspection

Thermoelectricity is caused by coupled transport of heat and electricity in metals and semiconductors that leads to a number of interesting phenomena, some of which can be exploited for NDE and materials characterization. The coupled constitutive equations can be written as

follows

$$\begin{bmatrix} \mathbf{J} \\ \mathbf{h} \end{bmatrix} = \begin{bmatrix} \sigma & \sigma S \\ \sigma S T & \kappa \end{bmatrix} \begin{bmatrix} -\nabla V \\ -\nabla T \end{bmatrix}, \quad (74)$$

where  $\mathbf{J}$  is the electric current density,  $\mathbf{h}$  is the thermal flux density,  $V$  is the electric potential,  $T$  is temperature,  $\sigma$  is the electric conductivity at  $\nabla T = 0$ ,  $\kappa$  is the thermal conductivity at  $\nabla V = 0$ , and  $S$  denotes the thermoelectric power.

Most existing thermoelectric NDE methods are based on the well-known Seebeck effect that is commonly used in thermocouples to measure temperature at the junction between two different conductors [161, 162]. Figure 89 shows a schematic representation (a) of the open-circuit Seebeck effect and (b) its typical realization in contact thermoelectric NDE. In this commonly used configuration the current density  $\mathbf{J}$  is always zero, therefore Eq. (74) yields  $\nabla V = -S \nabla T$ . One of the reference electrodes is heated by electrical means to a preset temperature of 100-300 °C, pretty much like the tip of a temperature-stabilized soldering iron, and connected to the inverting (-) input of the differential amplifier driving the indicator. The other electrode is left cold at essentially room temperature and is connected to the non-inverting (+) input. The measurement is done quickly enough to assure (i) that the hot reference electrode is not cooled down perceivably by the specimen and (ii) that the rest of the specimen beyond the

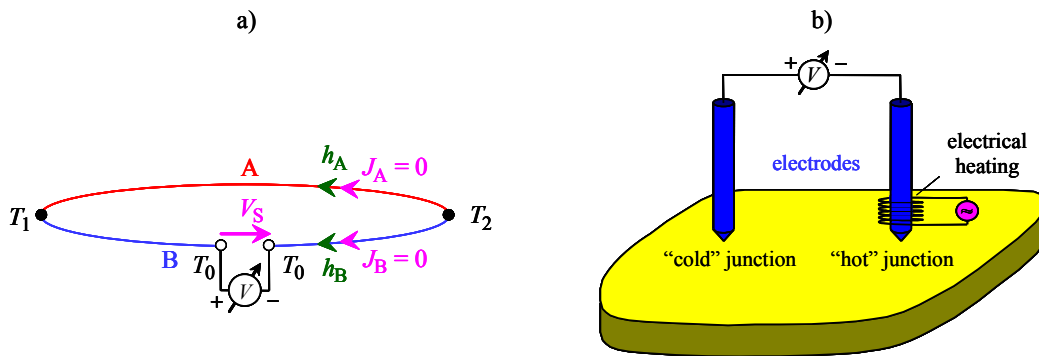


Figure 89 A schematic representation (a) of the open-circuit Seebeck effect and (b) its typical realization in contact thermoelectric NDE.



close vicinity of the contact point is not warmed up perceptibly. The measured thermoelectric voltage can be calculated as follows

$$V = \int_{T_1}^{T_2} (S_A - S_B) dT = \bar{S}_{AB} (T_2 - T_1), \quad (75)$$

where the relative thermoelectric power of the specimen with respect to the reference electrode is  $S_{AB} = S_A - S_B$  and the bar indicates averaging between  $T_1$  and  $T_2$ . The conventional contact thermoelectric technique is sensitive to material properties only in the vicinity of the hot electrode where significant temperature gradients occur [163]. In addition, it is very sensitive to thermal and electric interface conditions at the small contact area, which renders the reproducibility of contact thermoelectric measurements rather poor [164].

Self-referencing thermoelectric measurements can be done in an entirely non-contact way by using high-sensitivity magnetic detectors to sense the weak thermoelectric currents around inclusions and other types of inhomogeneity when the specimen to be tested is subjected to directional heating or cooling [165-168]. Figure 90 shows a schematic representation (a) of the closed-circuit Seebeck effect and (b) its typical realization in non-contact thermoelectric NDE. External heating or cooling is applied to the specimen to produce a substantial temperature gradient in the region to be tested. As a result, different points on the boundary between the host

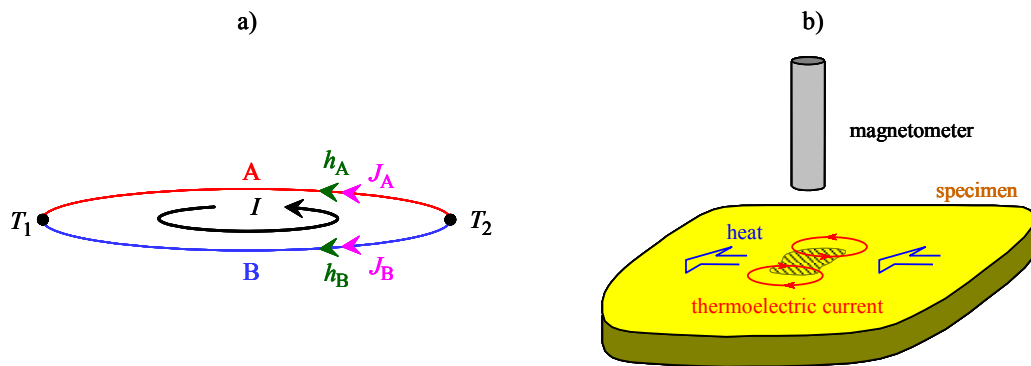


Figure 90 A schematic representation (a) of the closed-circuit Seebeck effect and (b) its typical realization in non-contact thermoelectric NDE.

material and the damaged region will be at different temperatures, therefore also at different thermoelectric potentials. These potential differences will produce opposite thermoelectric currents inside and outside the inclusion. The thermoelectric current forms local loops that run in opposite directions on the two sides of the inclusion relative to the prevailing heat flux, as it is indicated in Figure 90b. When the specimen is scanned with a sensitive magnetometer, such as a fluxgate or a Superconducting Quantum Interference Device (SQUID), the magnetic field of these thermoelectric currents can be detected even if the inclusion is buried below the surface and the sensor is fairly far away from the specimen.

Ideally, regardless of how high the temperature difference between the junctions is, only thermocouples made of different materials, i.e., materials of different thermoelectric powers, will generate thermoelectric signals. This unique feature makes the simple thermoelectric tester one of the most sensitive material discriminators used in nondestructive inspection. The thermoelectric power of metals is sensitive to a variety of material properties that can affect the measurement. Clearly, chemical composition exerts the strongest effect on the thermoelectric properties and accordingly the basic application of thermoelectric materials characterization is metal sorting. This unique sensitivity can be exploited for detecting minor variations in chemical composition such as those accompanying hydrogen embrittlement [169, 170]. However, it is known that materials of identical chemical composition can also produce an efficient thermocouple as a result of different heat treatments, hardening, texture, fatigue, etc., which can be further exploited for non-destructive testing of materials. For example, thermoelectric inspection has been successfully demonstrated for detection and characterization of thermal aging [171], radiation embrittlement, and low-cycle fatigue [172].

It is well known that thermoelectric measurements are uniquely sensitive to changes in

intensive material properties while being completely insensitive to extensive properties therefore offer unique advantages over other methods in cases when discrimination between these two different classes of variables is necessary. Figure 91a illustrates that a semi-spherical hole produced by low-stress milling, which is expected to generate only negligible hardening and residual stress below the machined surface, produces no significant thermoelectric signature while an otherwise similar semi-spherical indentation produced by pressing a stainless steel ball into the material in a manner that simulates a single impact during shot peening produces very strong effect. After annealing the copper specimens in a vacuum furnace for 30 minutes at 700 °C all the effects of plastic deformation during indentation disappear. This unique selectivity to material variations accompanied by total insensitivity to geometrical variations can be exploited for monitoring residual stress relaxation in shot-peened copper components as it is illustrated in Figure 91b [173]. The thermoelectric magnetic signature produced by shot peening exhibits essentially linear dependence on the peening intensity. After thermal relaxation, the magnetic signature vanishes as the residual stress completely relaxes in the specimen.

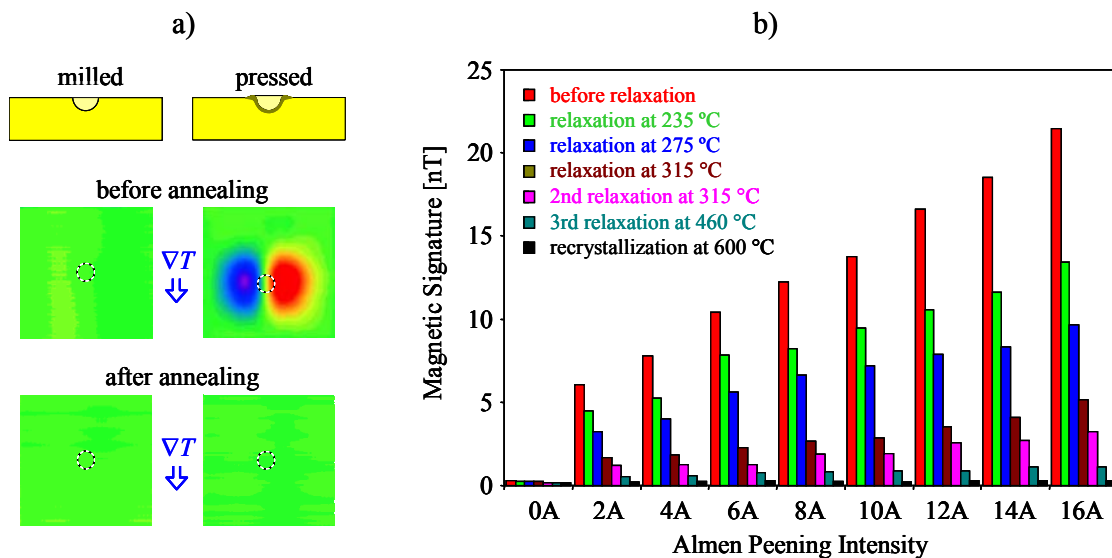


Figure 91 Non-contact thermoelectric detection of (a) plastic flow caused by surface indentation in copper and residual stress relaxation monitoring in shot-peened copper components [173].

## Exercise Problems

### Problem 1.1

Let us consider Gauss' law for the electrical flux density  $\mathbf{D}$ .

- Derive Gauss' law from Maxwell's equations.
- Use the relationship between the electrical flux density  $\mathbf{D}$  and the electrical field  $\mathbf{E}$  to derive Coulomb's law for the electrostatic force acting between two electric charges  $Q_1$  and  $Q_2$ .

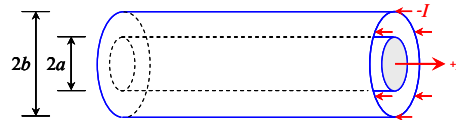
### Problem 1.2

Let us consider Ampère's law for the magnetic field strength  $\mathbf{H}$ .

- Derive Ampère's law from Maxwell's equations.
- Derive Ampère's law from the Biot-Savart law.
- Calculate the magnetic field of the known electrical current in a long straight wire.

### Problem 1.3

Let us consider a coaxial cable consisting of a highly conducting inner core of radius  $a$  and an outer shell of radius  $b$  as shown below. The insulation between the inner core and outer shell is a dielectric material of relative permittivity  $\epsilon_r$ .



- Find the capacitance of the coaxial cable over a unit length.
- Find the inductance of the coaxial cable over a unit length.
- Calculate the square root of the product of the capacitance and inductance for a given length  $\ell$ . What is the physical meaning of this quantity?

### Problem 1.4

Let us consider the two-dimensional vector field  $\mathbf{A} = A_x(x, y)\mathbf{e}_x + A_y(x, y)\mathbf{e}_y$ .

- Calculate  $\nabla \times (\nabla \times \mathbf{A})$ .
- Calculate  $\nabla(\nabla \cdot \mathbf{A})$
- Calculate  $\nabla^2 \mathbf{A}$

- d) Check the vector identity  $\nabla \times (\nabla \times \mathbf{A}) = \nabla(\nabla \cdot \mathbf{A}) - \nabla^2 \mathbf{A}$ .

### Problem 1.5

Let us consider a single-turn air-core coil of radius  $a$ . Calculate the magnetic field  $\mathbf{H}(z)$  along the axis of the coil for a given driving current  $I$ .

### Problem 1.6

Let us consider alternating current  $I$  flow in a long conducting cylindrical rod of radius  $a$  at frequency  $f$ . Assume that the conductivity  $\sigma$  and permeability  $\mu$  are known. The current distribution in the conductor is given by

$$J_z(r) = \frac{I}{\pi a^2} \frac{k a J_0(k r)}{2 J_1(k a)}$$

- Show that at very low frequencies the current distribution approaches the DC asymptote of uniform intensity.
- Show that the integrated current through the whole cross section is indeed equal to  $I$  regardless of frequency.
- Derive an asymptotic approximation for the current distribution at high frequencies.

### Problem 2.1

Let us consider electromagnetic wave penetration into an aluminum alloy of  $\sigma = 28$  %IACS at  $f = 400$  kHz.

- Calculate the standard penetration depth.
- Calculate the phase velocity of the diffuse electromagnetic wave.
- Estimate the complex transmission coefficient of the electric field at normal incidence.

### Problem 2.2

Let us consider eddy current penetration in a conducting material. What is the phase lag of the eddy current density at half of the standard penetration depth below the surface relative to the phase at the surface?

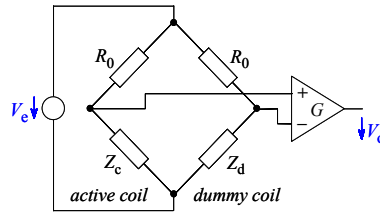
### Problem 2.3

Let us consider the complex electric impedance  $\tilde{Z}_{coil}$  of an eddy current probe coil. The probe-specimen arrangement can be modeled by an inductively coupled pair of coils, the

secondary coil being the material to be tested. The self-inductances of the primary and secondary coils are  $L_{11} = 20 \mu\text{H}$  and  $L_{22} = 2 \mu\text{H}$ , respectively. The inspection frequency is  $f = 100 \text{ kHz}$  and the loading resistance is  $R_e = 3 \Omega$ . What is the phase angle  $\phi$  of the measured complex electric impedance of the coil probe at  $k = 0.8$  coupling coefficient?

### Problem 3.1

The figure below illustrates a typical measurement bridge used in continuous excitation eddy current instruments. Both the active and dummy coils are driven through  $R_0$  resistances from a voltage source of  $V_e$ . Due to interaction with the magnetic field of eddy currents in the specimen under test, the complex electric impedance of the active coil  $Z_c$  will deviate from that of the otherwise identical dummy coil  $Z_d$  by a small relative difference  $\xi$  so that  $Z_c = Z_d (1 + \xi)$ . Estimate the frequency dependence of the sensitivity of the measurement bridge to such small impedance variations. How do you choose the driver resistance  $R_0$  to achieve maximum sensitivity at a given inspection frequency?



### Problem 3.2

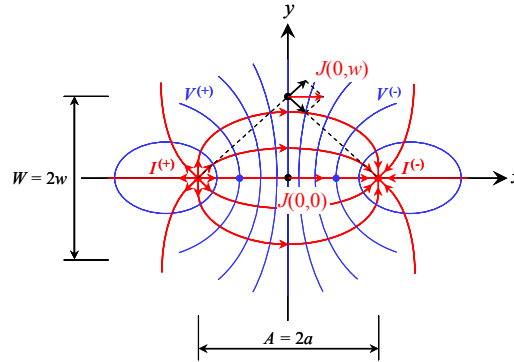
The apparent eddy current conductivity of a surface-treated nonmagnetic specimen has been measured as  $\text{AECC}(f) = \sigma_i + \Delta\sigma (1 - e^{-f/f_t})$ , where  $\sigma_i$  is the conductivity of the intact material measured at very low inspection frequencies,  $\Delta\sigma$  is the relatively small excess conductivity at the surface measured at very high inspection frequencies, and  $f_t$  is the transition frequency of the AECC spectrum. Estimate the electric conductivity depth profile  $\sigma(z)$ .

### Problem 3.3

Let us consider a stack of aluminum shims. Each shim has the same thickness of  $t = 0.127 \text{ mm}$ . The conductivity of the aluminum alloy is 36 %IACS. Approximately, how many shims can eddy current inspection penetrate at  $f = 10 \text{ kHz}$  inspection frequency before the current density drops to 10% of its maximum value in the top shim?

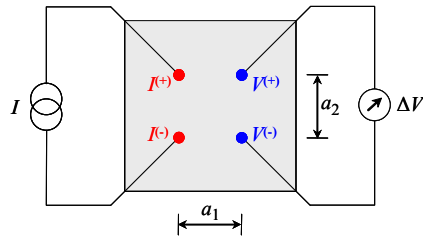
### Problem 4.1

Let us consider DCPD testing of a thin conducting plate as shown below. The separation between the point-like injection electrodes is  $A = 2a$ . Let us define the width  $W = 2w$  of the electric current distribution halfway between the two electrodes as the distance between the two points where the current intensity drops to half of its corresponding value on the axis between the injection electrodes, i.e.,  $J(0,w) = J(0,0)/2$ . Calculate the width of the current distribution.



### Problem 4.2

Let us consider DCPD testing of a thin conducting plate using a rectangular electrode system as shown below. Assume that the plate thickness  $t$ , and the electrode separations  $a_1$  and  $a_2$  are known ( $t \ll a_1, a_2$ ). Develop a formula for the electric resistivity  $\rho$  of the plate from the measured resistance  $R = \Delta V/I$ .



### Problem 4.3

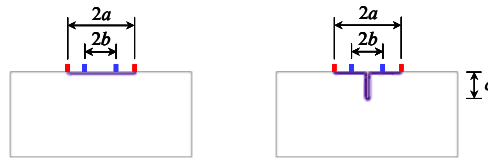
Repeat Problem 4.2 assuming that the plate thickness  $t$  is much larger than the electrode separations  $a_1$  and  $a_2$ . Specialize the case to a square electrode  $a_1 = a_2 = a$ .

### Problem 4.4

Repeat Problem 4.2 for a plate of finite thickness assuming that the plate thickness  $t$  is comparable to the electrode separations  $a_1$  and  $a_2$ .

### Problem 4.5

Let us consider a conducting specimen with a very long crack of constant depth  $c$  running through it normal to its surface. Intact and cracked specimens are inspected with an in-line four-point electrode configuration as shown below ( $a = 2b$  and  $b = 2c$ ). Use the thin-skin approximation to predict the relative resistivity increase caused by the crack in high-frequency ACPD inspection. Assume that the conductivity of the nonmagnetic material and the inspection frequency are known.



### Problem 5.1

Weakly conducting materials act like dielectrics above a certain transition frequency. Let us consider a material having relative magnetic permeability  $\mu_r = 1$ , relative electric permittivity  $\epsilon_r = 3$ , and electric conductivity  $\sigma = 1.2 \times 10^{-3}$  S/m.

- What is the approximate transition frequency above which this material acts like a dielectric?
- What is the attenuation coefficient of the propagating electromagnetic wave if the inspection frequency is much higher than this transition frequency?
- Recalculate a more accurate transition frequency between the conductive and dielectric regions based on the definition that at the transition frequency the attenuation coefficients predicted by the low-frequency (conductive) and high-frequency (dielectric) asymptotic models are the same.

### Problem 5.2

Let us consider L-band microwave radiation of 1.2 GHz frequency for ground-penetrating radar applications. The electric conductivity and relative permittivity of dry earth are  $\sigma_{\text{dry}} = 1 \times 10^{-4}$  S/m and  $\epsilon_{\text{rdry}} = 3$ , respectively. In wet earth, the same parameters increase to  $\sigma_{\text{rwet}} = 1 \times 10^{-3}$  S/m and  $\epsilon_{\text{rwet}} = 6$ . Assume that the relative magnetic permeability is  $\mu_r = 1$ .

- What is the reflection coefficient at the boundary between a dry surface layer and the wet earth below it?



b) What fraction of the energy is transmitted at the same interface?

### Problem 5.3

Let us consider the in-situ thermoelectric power (TEP) monitoring arrangement shown below. Two pairs of K-type thermocouple wires are electric spot welded to the specimen at two distant locations having temperatures  $T_1$  and  $T_2$  that are changing according to service conditions. Two temperature readings are taken in each measurement cycle using the C1-A1 ( $T_1$ ) and C2-A2 ( $T_2$ ) thermocouples. In addition, the voltage differences between the two Alumel wires A1-A2 ( $V_3$ ) and two Chromel wires C1-C2 ( $V_4$ ) are also measured. Derive a formula for the average TEP  $\bar{S}_S$  of the specimen from the measured quantities  $T_1$ ,  $T_2$ ,  $V_3$ , and  $V_4$ . Assume that the average TEP of Chromel  $\bar{S}_C \approx 22.3 \mu\text{V}/^\circ\text{C}$  and Alumel  $\bar{S}_A \approx -18.5 \mu\text{V}/^\circ\text{C}$  are known over the operational temperature range.



## References

- [1] C. A. de Coulomb, *First Memoir on Electricity and Magnetism* (1785).
- [2] A. M. Ampère, *Collection of Observations on Electrodynamics* (1822).
- [3] M. Faraday, *Experimental Researches in Electricity* (1839).
- [4] J. C. Maxwell, "A dynamic theory of the electromagnetic field," *Phil. Trans. Royal Soc. (London)* **155**, 450 (1865).
- [5] R. S. Elliott (1999). *Electromagnetics: History, Theory, and Applications* (Wiley, 1999).
- [6] D. K. Cheng, *Field and Wave Electromagnetics*, 2nd edition (Prentice Hall, 1989)
- [7] J. A. Edminister, *Electromagnetics*, 2nd edition (McGraw-Hill, 1993).
- [8] U. S. Inan and A. S. Inan, *Engineering Electromagnetics* (Adison Wesley Longman, 1999).
- [9] U. S. Inan and A. S. Inan, *Electromagnetic Waves* (Prentice Hall, 2000).
- [10] J. A. Stratton, *Electromagnetic Theory* (IEEE Press, 2007)
- [11] L. J. Giacoletto, "Frequency- and time-domain analysis of skin effects," *IEEE Trans. Magn.* **32**, 220-229 (1996).
- [12] G. Sposito, P. Cawley, and P. B. Nagy, "An approximate model for three-dimensional alternating current potential drop analyses using a commercial finite element code," *NDT&E International* **43**, 134-140 (2010).
- [13] H. L. Libby, *Introduction to Electromagnetic Nondestructive Testing Methods* (Wiley-Interscience, 1971).
- [14] G. Birnbaum, *Eddy Current Characterization of Materials and Structures* (ASTM Intl., 1981).
- [15] W. Lord, *Electromagnetic Methods of Nondestructive Testing* (Gordon and Breach, 1985).
- [16] D. J. Hagemaiier, *Fundamentals of Eddy Current Testing* (ASNT, 1990).
- [17] J. Blitz, *Electrical and Magnetic Methods of Nondestructive Testing* (Adam Hilger, 1991).
- [18] A. Krawczyk and J. A. Tegopoulos, *Numerical Modelling of Eddy Currents* (Clarendon Press, 1993).
- [19] S. S. Udpa (ed.) *Electromagnetic Testing: Eddy Current, Flux Leakage, and Microwave Nondestructive Testing, Nondestructive Testing Handbook*, 3rd edition, Vol. 5 (ASNT, 2004).
- [20] C. V. Dodd, C. C. Cheng, and W. E. Deeds, "Induction coils coaxial with an arbitrary number of cylindrical conductors," *J. Appl. Phys.* **45**, 638-647 (1974).
- [21] C. V. Dodd and W. E. Deeds, "Analytical solutions to eddy-current probe-coil problems," *J. Appl. Phys.* **39**, 2829-2838 (1968).
- [22] C. C. Cheng, C. V. Dodd, and W. E. Deeds, "General analysis of probe coils near stratified conductors," *Int. J. Nondestr. Testing* **3**, 109-130 (1971).
- [23] J. R. Bowler, "Eddy current interaction with an ideal crack, Part I: The forward problem," *J. Appl. Phys.* **75**, 8128-8137 (1994).
- [24] N. Ida, *Numerical Modeling for Electromagnetic Non-Destructive Evaluation* (Chapman & Hall, 1995).
- [25] J. R. Bowler, Y. Yoshida, and N. Harfield, "Vector-potential boundary-integral evaluation of eddy-current interaction with a crack," *IEEE Trans. Magn.* **33**, 4287-4294 (1997).
- [26] B. A. Auld and J. C. Moulder, "Review of advances in quantitative eddy current nondestructive evaluation," *J. Nondestr. Eval.* **18**, 3-36 (1999).

- [27] R. Palanisamy and W. Lord, "Finite element modeling of electromagnetic NDT phenomena," *IEEE Trans. Magn.* **15**, 1479-1481 (1979).
- [28] R. Palanisamy and W. Lord, "Prediction of eddy current probe signal trajectories," *IEEE Trans. Magn.* **16**, 1083-1085 (1980).
- [29] W. Lord and R. Palanisamy, "Development of theoretical models for nondestructive testing eddy current phenomena," in *Eddy Current Characterization of Materials and Structures*, (ASTM, 1981) pp. 5-21.
- [30] N. R. Ida, R. Palanisamy, and W. Lord, "Eddy current probe design using finite element analysis," *Mat. Eval.* **42**, 1389-1394 (1984).
- [31] R. Becker, K. Betzold, K. D. Boness, R. Collins, C. C. Holt, and J. Simkin, "The modeling of electrical current NDT methods: Its application to weld testing (Part 1)," *British J. Nondestr. Test.* **28**, 286-294 (1986).
- [32] M. Blodgett, W. Hassan, and P. B. Nagy, "Theoretical and experimental investigations of the lateral resolution of eddy current imaging," *Mat. Eval.* **58**, 647-654 (2000).
- [33] Z. Mottl, "The quantitative relations between true and standard depth of penetration for air-cored probe coils in eddy current testing," *NDT Int.* **23**, 11-18 (1990).
- [34] P. Stucky and W. Lord, "Skin depth considerations in eddy current NDT," *Rev. Progr. Quant. Nondestr. Eval.* Vol. **11**, 299-306 (1992).
- [35] D. L. Atherton and S. Sullivan, "The remote-field through-wall electromagnetic inspection technique for pressure tubes," *Mat. Eval.* **44**, 1544-1550 (1986).
- [36] S. Sullivan and D. L. Atherton, "Analysis of the remote field eddy current effect in non-magnetic tubes," *Mat. Eval.* **47**, 80-86 (1989).
- [37] S. Sullivan, D. L. Atherton, and T. R. Schmidt, "Comparison of conventional, through-wall and remote field eddy current techniques," *NDT Int.* **22**, 203-206 (1989).
- [38] Y. S. Sun, M. X. Qu, J. T. Si, C. T. Lu, X. Y. Zhou, and D. L. Atherton, "Improvements in remote-field eddy current probe structure," *Mat. Eval.* **50**, 600-604 (1992).
- [39] D. L. Atherton, W. Czura, and D. D. Mackintosh, "Remote field eddy current defect interactions: effects on the external field," *Mat. Eval.* **52**, 1288-1291 (1994).
- [40] D. L. Waidelich, "Pulsed eddy currents," in: *Research Techniques in Nondestructive Testing*, ed. R. S. Sharpe Vol. 1, (Academic, 1970) pp. 383-416.
- [41] H. C. Ohanian, "On the approach to electro- and magneto-static equilibrium," *Am. J. Phys.* **51**, 1020-1022 (1983).
- [42] J. Bowler and M. Johnson, "Pulsed eddy-current response to a conducting half-space," *IEEE Trans. Magn.* **33**, 2258-2264 (1997).
- [43] M. Morozov, G. Y. Tian, and D. Edgar, "Comparison of PEC and SFEC NDE techniques," *Nondestr. Test. Eval.* **24**, 153-164 (2009).
- [44] C. Mandache and J. H. V. Lefebvre, "Transient and harmonic eddy currents: Lift-off point of intersection," *NDT&E Int.* **39**, 57-60 (2006).
- [45] E. Peterson, "Harmonic production in ferromagnetic materials at low frequencies and low flux densities," *Bell Syst. Tech. J.* **7**, 762-796 (1928).
- [46] K. Gruska, "Use of harmonic analysis for inspection of ferromagnetic materials," *Sov. J. Nondestr. Testing* **19**, 399-409 (1983).
- [47] B. Heutling, W. Reimche, A. Krysz, L. Grube, M. Stock, Fr.-W. Bach, J. Kroos, M. Stolzenberg, and G. Westkämper, "Online NDE of mechanical-technological material characteristics of cold rolled steel strips by using the harmonic analysis of eddy current signals," *Int. J. Appl. Electromagn. Mech.* **19**, 445-451 (2004).

- [48] A. McNab and J. Thomson, "Measurement technique for eddy-current arrays," in: *IEE Proc.: Physical Science, Measurement and Instrumentation, Management and Education*, pp. 147–154 (1990).
- [49] L. Hardy, A. Billat, and G. Villerman-Lecolier, "Flat eddy-current matrix sensor for detecting metallic objects," *Sens. Actuators A: Phys.* **29**, 13–19 (1991).
- [50] M. Gramz and T. Stepinski, "Eddy current imaging, array sensors and flaw reconstruction," *Res. Nondestr. Eval.* **5**, 157–174 (1994).
- [51] A. McNab and J. Thomson, "An eddy-current array instrument for application on ferritic welds," *NDT&E Int.* **28**, 103–112 (1995).
- [52] N. Goldfine, V. Zilberstein, J. S. Cargill, D. Schlicker, I. Shay, A. Washabaugh, V. Tsukernik, D. Grundy, M. Windoloski, "Meandering winding magnetometer array eddy current sensors for detection of cracks in regions with fretting damage," *Mater. Eval.* **60**, 870–877 (2002).
- [53] H. Y. Huang, N. Sakurai, T. Takagi, T. Uchimoto, "Design of an eddy-current array probe for crack sizing in steam generator tubes," *NDT&E Int.* **36**, 515–522 (2003).
- [54] R. Grimberg, L. Udpa, A. Savin, R. Steigmann, V. Palihovici, and S. S. Udpa, "2D Eddy current sensor array," *NDT&E Int.* **39**, 264–271 (2006).
- [55] M. P. Blodgett and P. B. Nagy, "Eddy current assessment of near-surface residual stress in shot-peened nickel-base superalloys," *J. Nondestr. Eval.* **23**, 107–123 (2004).
- [56] B. Abu-Nabah and P. B. Nagy, "Lift-off effect in high-frequency eddy current conductivity spectroscopy," *NDT&E Int.* **40**, 555–565 (2007).
- [57] B. A. Abu-Nabah, F. Yu, W. T. Hassan, M. P. Blodgett, and P. B. Nagy, "Eddy current residual stress profiling in surface-treated engine alloys," *Nondestr. Testing Eval.* **24**, 209–232 (2009).
- [58] D. Jiles, *Introduction to Magnetism and Magnetic Materials* (Chapman & Hall, 1998).
- [59] N. J. Goldfine, "Magnetometers for improved materials characterization in aerospace applications," *Mat. Eval.* **5**, 396–405 (1993).
- [60] P. B. Nagy, "Nondestructive methods for materials state awareness monitoring," *Insight* **52**, 61–71 (2010).
- [61] D. Kalkhof, M. Grosse, M. Niffenegger, and H. J. Leber, "Monitoring fatigue degradation in austenitic stainless steels," *Fatigue Fract. Engg. Mater. Struct.* **27**, 595–607 (2004).
- [62] J. Moulder, C. E. Uzal, and J. H. Rose, "Thickness and conductivity of metallic layers from eddy current measurements," *Rev. Sci. Instrum.* **63**, 3455–3465 (1992).
- [63] A. Sethuraman and J. H. Rose, "Rapid inversion of eddy current data for conductivity and thickness of metal coatings," *J. Nondestr. Eval.* **14**, 39–46 (1995).
- [64] Y. Nonaka, "A double coil method for simultaneously measuring the resistivity, permeability, and thickness of a moving metal sheet," *IEEE Trans. Instrum. Meas.* **45**, 478–482 (1996).
- [65] C. C. Tai, J. H. Rose, and J. C. Moulder, "Thickness and conductivity of metallic layers from pulsed eddy-current measurements," *Rev. Sci. Instrum.* **67**, 3965–3972 (1996).
- [66] W. Yin and A. J. Peyton, "Thickness measurement of non-magnetic plates using multi-frequency eddy current sensors," *NDT&E Intern.* **40**, 43–48 (2007).
- [67] A. Sethuraman and J. H. Rose, "Rapid inversion of eddy current data for conductivity and thickness of metal coatings," *J. Nondestr. Eval.* **14**, 39–46 (1995).
- [68] C. C. Tai, J. H. Rose, and J. C. Moulder, "Characterization of coatings on magnetic metals using swept-frequency eddy current and transient eddy current methods," *Rev. Progr.*

- Quant. Nondestr. Eval.* **16**, 1593–1600 (1997).
- [69] H. C. Yang and C. C. Tai, “Pulsed eddy-current measurement of a conducting coating on a magnetic metal plate,” *Meas. Sci. Techn.* **13**, 1259–1265 (2002).
  - [70] J. R. Bowler and S. J. Norton, “Eddy current inversion for layered structures,” *Res. Nondestr. Eval.* **4**, 205–219 (1992).
  - [71] E. Uzal and J. H. Rose, “The impedance of eddy current probes above layered metals whose conductivity and permeability vary continuously,” *IEEE. Trans. Magn.* **29**, 1869–1873 (1993).
  - [72] E. Uzal, J. C. Moulder, S. Mitra, and J. H. Rose, “Impedance of coils over layered metals with continuously variable conductivity and permeability: Theory and experiment,” *J. Appl. Phys.* **74**, 2076–2089 (1993).
  - [73] E. Uzal, J. C. Moulder, and J. H. Rose, “Experimental determination of the near-surface conductivity profiles of metals from electromagnetic induction (eddy current) measurements,” *Inv. Probl.* **10**, 753–764 (1994).
  - [74] T. P. Theodoulidis, T. D. Tsiboukis, and E. E. Kriezis, “Analytical solutions in eddy current testing of layered metals with continuous conductivity profiles,” *IEEE Trans. Magn.* **31**, 2254–2260 (1995).
  - [75] M. P. Blodgett, C. V. Ukpabi, and P. B. Nagy, “Surface roughness influence on eddy current electrical conductivity measurements,” *Mat. Eval.* **61**, 765–772 (2003).
  - [76] K. Kalyanasundaram and P. B. Nagy, “A simple numerical model for calculating the apparent loss of eddy current conductivity due to surface roughness,” *NDT&E Int.* **37**, 47–56 (2004).
  - [77] F. Yu and P. B. Nagy, “Numerical method for calculating the apparent eddy current conductivity loss on randomly rough surfaces,” *J. Appl. Phys.* **95**, 8340–8351 (2004).
  - [78] F. Yu and P. B. Nagy, “Simple analytical approximations for eddy current profiling of the near-surface residual stress in shot-peened metals,” *J. Appl. Phys.* **96**, 1257–1266 (2004).
  - [79] F. Yu, M. P. Blodgett, and P. B. Nagy, “Eddy current assessment of near-surface residual stress in shot-peened inhomogeneous nickel-base superalloys,” *J. Nondestr. Eval.* **25**, 17–28 (2006).
  - [80] F. Yu and P. B. Nagy, “On the influence of cold work on eddy current characterization of near-surface residual stress in shot-peened nickel-base superalloys,” *J. Nondestr. Eval.* **25**, 107–122 (2006).
  - [81] B. Abu-Nabah and P. B. Nagy, “Iterative inversion method for eddy current profiling of near-surface residual stress in surface-treated metals,” *NDT&E Int.* **39**, 641–651 (2006).
  - [82] Y. Shen, C. Lee, C.C. H. Lo, N. Nakagawa, and A.M. Frishman, “Conductivity profile determination by eddy current for shot-peened superalloy surfaces toward residual stress assessment,” *J. Appl. Phys.* **101**, 014907 (2007).
  - [83] W. Yin, S. J. Dickinson, and A. J. Peyton, “Imaging the continuous conductivity profile within layered metal structures using inductance spectroscopy,” *IEEE Sensors J.* **5**, 161–166 (2005).
  - [84] V. Sundararaghavan, “A multi-frequency eddy current inversion method for characterising conductivity gradients on water jet peened components,” *NDT&E Int.* **38**, 541–547 (2005).
  - [85] I. T. Rekanos, T. P. Theodoulidis, S. M. Panas, and T. D. Tsiboukis, “Impedance inversion in eddy current testing of layered planar structures via neural networks,” *NDT&E Int.* **30**, 69–74 (1997).
  - [86] C. Glorieux, J. Moulder, J. Basart, and J. Thoen, “The determination of electrical

- conductivity profiles using neural network inversion of multi-frequency eddy-current data,” *J. Phys. D: Appl. Phys.* **32**, 616-622 (1999).
- [87] H. A. Sabbagh, E. H. Sabbagh, R. K. Murhpy, and J. Nyenhuis, “Assessing thermal barrier coatings by eddy current inversion,” *Mat. Eval.* **59**, 1307-1312 (2001).
  - [88] S. M. Nair and J. H. Rose, “Reconstruction of three-dimensional conductivity variations from eddy current (electromagnetic induction) data,” *Inv. Probl.* **6**, 1007-1030 (1990).
  - [89] J. H. Rose and S. M. Nair, “Exact recovery of the DC electrical conductivity of a layered solid,” *Inv. Probl.* **7**, L31-L36 (1991).
  - [90] S. Ross, M. Lusk, and W. Lord, “Application of a diffusion-to-wave transformation for inverting eddy current nondestructive evaluation data,” *IEEE Trans. Magn.* **32**, 535-546 (1996).
  - [91] J. R. Bowler, S. A. Jenkins, L. D. Sabbagh, and H. A. Sabbagh, “Eddy-current probe impedance due to a volumetric flaw,” *J. Appl. Phys.* **70**, 1107-1114 (1991).
  - [92] S. J. Norton and J. R. Bowler, “Theory of eddy-current inversion,” *J. Appl. Phys.* **73**, 501-512 (1993).
  - [93] Y. Li, L. Udpa, and S. S. Udpa, “Three-dimensional defect reconstruction from eddy-current NDE signals using a genetic local search algorithm,” *IEEE Trans. Magn.* **40**, 410-417 (2004).
  - [94] M. Blodgett and P. B. Nagy, “Anisotropic grain noise in eddy current inspection of noncubic polycrystalline metals,” *Appl. Phys. Lett.* **72**, 1045-1047 (1998).
  - [95] S. S. Hecker, M. G. Stout, K. P. Staudhammer, and J. L. Smith, “Effects of strain state and strain rate on deformation-induced transformation in 304 stainless-steel,” *Metall. Trans. A* **13**, 619-626 (1982).
  - [96] K. Mumtaz, S. Takahashi, J. Echigoya, Y. Kamada, L. F. Zhang, H. Kikuchi, K. Ara, and M. Sato, “Magnetic measurements of the reverse martensite to austenite transformation in a rolled austenitic stainless steel,” *J. Mat. Sci.* **39**, 1997-2010 (2004).
  - [97] D. Kalkhof, M. Grosse, M. Niffenegger, and H. J. Leber, “Monitoring fatigue degradation in austenitic stainless steels,” *Fatigue Fract. Engg. Mater. Struct.* **27**, 595-607 (2004).
  - [98] J. F. Nye, *Physical Properties of Crystals, Their Representation by Tensors and Matrices* (Clarendon Press, Oxford, 1985).
  - [99] J. E. Neighbor, “Eddy-current method for measuring anisotropic resistivity,” *J. Appl. Phys.* **40**, 3078-80 (1969).
  - [100] V. M. Tatarnikov, “Use of probes for measuring the electrical conductance of anisotropic plates,” *Meas. Tech.* **13**, 877-881 (1970).
  - [101] V. I. Gordienko and V. G. Rybachuk, “Device for measuring the anisotropy of electric conductivity,” *Meas. Tech.* **32**, 371-374 (1989).
  - [102] P. L. Rossitier, *The Electrical Resistivity of Metals and Alloys* (Cambridge University Press, 1987).
  - [103] R. Pitchumani, P. K. Liaw, D. C. Yao, D. K. Hsue, and H. Jeong, “Eddy current technique for the measurement of constituent volume fractions in a three-phase metal-matrix composite,” *J. Comp. Mat.* **28**, 1742-1769 (1994).
  - [104] R. Pitchumani, P. K. Liaw, D. C. Yao, D. K. Hsue, and H. Jeong, “Theoretical models for the anisotropic conductivities of two-phase and three-phase metal-matrix composites,” *Acta. Metal. Mat.* **43**, 3045-3059 (1995).
  - [105] G. T. Meaden, *Electrical Resistance of Metals* (Plenum, 1965).
  - [106] K. Grotz and B. Lutz, “Electromagnetic multiparameter determination of material

- characteristics,” *Mat. Eval.* **49**, 40-43 (1991).
- [107] M. Zergoug, S. Lebaili, H. Boudjellal, and A. Benchaala, “Relation between mechanical microhardness and impedance variations in eddy current testing,” *NDT&E Int.* **37**, 65-72 (2004).
  - [108] S. Konoplyuk, T. Abe, T. Uchimoto, T. Takagi, and M. Kurosawa, “Characterization of ductile cast iron by eddy current method,” *NDT&E Int.* **38**, 623–626 (2005).
  - [109] D. Mercier, J. Lesage, X. Decoopman, and D. Chicot, “Eddy currents and hardness testing for evaluation of steel decarburizing,” *NDT&E Int.* **39**, 652-660 (2006).
  - [110] B. A. Abu-Nabah, W. T. Hassan, D. Ryan, M. P. Blodgett, and P. B. Nagy, “The effect of hardness on eddy current residual stress profiling in shot-peened nickel alloys,” *J. Nondestr. Eval.* **29**, 143-153 (2010).
  - [111] F. C. Schoenig, Jr., J. A. Soules, H. Chang, and J. J. DiCillo, “Eddy current measurement of residual stresses induced by shot peening in titanium Ti-6Al-4V,” *Mat. Eval.* **53**, 22-26 (1995).
  - [112] M. Blaszkiewicz, L. Albertin, and W. Junker “The eddy current technique for determining residual stresses in steels,” *Mater. Sci. Forum* **210**, 179-186 (1996).
  - [113] H. Chang, H., F. C. Schoenig, Jr., and J. A. Soules, “Eddy current offers a powerful tool for investigation of residual stress and other metallurgical properties,” *Mat. Eval.* **57**, 1257-1260 (1999).
  - [114] V. Zilberstein, M. Fisher, D. Grundy, D. Schlicker, V. Tsukernik, V. Vengrinovich, N. Goldfine, and T. Yentzer, “Residual and applied stress estimation from directional magnetic permeability measurements with MWM sensors,” *ASME J. Press. Vessel Techn.* **124**, 375-381 (2002).
  - [115] F. Yu and P. B. Nagy, “Dynamic piezoresistivity calibration for eddy current nondestructive residual stress measurements,” *J. Nondestr. Eval.* **24**, 143-152 (2005).
  - [116] B. Abu-Nabah and P. B. Nagy, “High-frequency eddy current conductivity spectroscopy for residual stress profiling in surface-treated nickel-base superalloys,” *NDT&E Int.* **40**, 405-418 (2007).
  - [117] Y. Shen, C. C. H. Lo, N. Nakagawa, and A. M. Frishman, “Residual stress profile assessment by eddy current for shot peened nickel superalloy,” *J. Nondestr. Eval.* **29**, 1-13 (2010).
  - [118] M. P. Connolly, D. H. Michael, and R. Collins, “The inversion of surface potential measurements to determine crack size and shape,” *J. Appl. Phys.* **64**, 2638-2647 (1988).
  - [119] A. M. Lewis, D. H. Michael, M. C. Lugg, and R. Collins, “Thin-skin electromagnetic fields around surface-breaking cracks in metals,” *J. Appl. Phys.* **64**, 3777-3784 (1988).
  - [120] R. LeTessier, R. W. Coade, and B. Geneve, “Sizing of cracks using the alternating current field measurement technique,” *Int. J. Press. Vess. Piping* **79**, 549–554 (2002).
  - [121] R. C. McMaster, “Electric current test principles,” in: *Nondestructive Testing Handbook* (Ronald Press, 1959) pp. 35.1–35.11.
  - [122] A. Uhler, “The potentials of infinite systems of sources and numerical solutions of problems in semiconductors engineering,” *Bell. Syst. Techn. J.* **34**, 105–28 (1955).
  - [123] I. Cerny, “The use of DCPD method for measurement of growth of cracks in large components at normal and elevated temperatures,” *Engg. Fract. Mech.* **71**, 837-848 (2004).
  - [124] T. V. Venkatasubramanian and B. A. Unvala, “An AC potential drop system for monitoring crack length,” *J. Phys. E: Sci. Instr.* **17**, 765–771 (1984).
  - [125] W. D. Dover, R. Collins, and D. H. Michael, “The use of AC-field measurements for crack

- detection and sizing in air and underwater,” *Phil. Trans. Roy. Soc. Lond. A* **320**, 271–283 (1986).
- [126] D. H. Michael, R. T. Waechter, and R. Collins, “The measurements of surface cracks in metals by using AC electric fields,” *Proc. Roy. Soc. Lond. A* **381**, 139–157 (1982).
  - [127] H. Saguy and D. Rittel, “Flaw detection in metals by the ACPD technique: theory and experiments,” *NDT&E Int.* **40**, 505–509 (2007).
  - [128] N. Bowler and Y. Huang, “Model-based characterization of homogeneous metal plates by four-point alternating current potential drop measurements,” *IEEE Trans. Magn.* **41**, 2102–2110 (2005).
  - [129] J. R. Bowler and N. Bowler, “Theory of four-point alternating current potential drop measurements on conductive plates,” *Proc. Roy. Soc. Lond. A* **463**, 817–836 (2007).
  - [130] N. Bowler, “Electric field due to alternating current injected at the surface on a metal plate,” *J. Appl. Phys.* **96**, 4607–4613 (2004).
  - [131] N. Bowler, “Analytical solution for the electric field in a half space conductor due to alternating current injected at the surface,” *J. Appl. Phys.* **95**, 344–348 (2004).
  - [132] Y. Sato, Y. Takeda, and T. Shoji, “Nondestructive evaluation of fatigue and creep-fatigue damage by means of ICFPD technique,” *Fat. Fract. Eng. Mater. Struct.* **24**, 885–893 (2001).
  - [133] Y. Sato, T. Atsumi, and T. Shoji, “Application of induced current potential drop technique for measurements of cracks on internal wall of tube-shaped specimens,” *NDT&E Int.* **40**, 497–504 (2007).
  - [134] D. Mirshekar-Syahkal, R. Collins, and D. H. Michael, “The influence of skin depth on crack measurement by the AC field technique,” *J. Nondestr. Eval.* **3**, 65–76 (1982).
  - [135] M. C. Lugg, “Data interpretation in ACPD crack inspection,” *NDT Int.* **22**, 149–154 (1989).
  - [136] I. S. Hwang and R. G. Ballinger, “A multi-frequency AC potential drop technique for the detection of small cracks,” *Meas. Sci. Techn.* **3**, 62–74 (1992).
  - [137] M. O. Lai and C. K. Ng, “Measurement of crack profiles using AC field measurement method,” *J. Nondestr. Eval.* **13**, 155–63 (1994).
  - [138] D. H. Michael, A. M. Lewis, M. McIver, and R. Collins, “Thin-skin electromagnetic fields in the neighbourhood of surface-breaking cracks in metals,” *Proc. Roy. Soc. Lond. A* **434**, 587–603 (1991).
  - [139] S. Chen and P. B. Nagy, “Edge weld penetration assessment using the potential drop technique,” *NDT&E Int.* **31**, 1–10 (1998).
  - [140] J. R. Bowler, Y. Q. Huang, H. Y. Sun, J. Brown, and N. Bowler, “Alternating current potential-drop measurement of the depth of case hardening in steel rods,” *Meas. Sci. Techn.* **19**, 075204 (2008).
  - [141] G. Sposito, P. Cawley, and P. B. Nagy, “Potential drop mapping for the monitoring of corrosion or erosion,” *NDT&E Int.* **43**, 394–402 (2010).
  - [142] A. J. Bahr, *Microwave Nondestructive Testing Methods* (Gordon and Breach, 1982).
  - [143] N. Ida, *Microwave NDT* (Kluwer Academic, 1992).
  - [144] R. Zoughi, “Microwave and millimeter wave nondestructive testing: A succinct introduction,” *Res. Nondestr. Eval.* **7**, 71–74 (1995).
  - [145] R. Zoughi, *Microwave Non-Destructive Testing and Evaluation* (Kluwer, 2000).
  - [146] D. M. Mittleman, R. H. Jacobsen, and M. C. Nuss, “T-ray imaging,” *IEEE J. Sel. Topics Quant. Eeetr.* **2**, 679–692 (1996).



- [147] D. M. Mittleman, M. Gupta, R. Neelamani, R. G. Baraniuk, J. V. Rudd, and M. Koch, "Recent advances in terahertz imaging," *Appl. Phys. B* **68**, 1085-1094 (1999).
- [148] D. Zimdars, J. S. White, G. Stuk, G. A. Chernovsky, G. Fichter, and S. Williamson, "Large area terahertz imaging and non-destructive evaluation applications," *Insight* **48**, 537-539 (2006).
- [149] Y. L. Lu, T. Wei, F. Duewer, Y. Q. Lu, N. B. Ming, P. G. Schultz, and X. D. Xiang, "Nondestructive imaging of dielectric-constant profiles and ferroelectric domains with a scanning-tip microwave near-field microscope," *Science* **276**, 2004-2006 (1997).
- [150] S. J. Lockwood and H. Lee, "Pulse-echo microwave imaging for NDE of civil structures: Image reconstruction, enhancement, and object recognition," *Int. J. Imag. Syst. Techn.* **8**, 407-412 (1997).
- [151] S. Caorsi, A. Massa, and M. Pastorino, "A crack identification microwave procedure based on a genetic algorithm for nondestructive testing," *IEEE Trans. Ant. Prop.* **49**, 1812-1820 (2001).
- [152] M. Pastorino, S. Caorsi, and A. Massa, "A global optimization technique for microwave nondestructive evaluation," *IEEE Trans. Instr. Meas.* **51**, 666-673 (2002).
- [153] M. T. Ghasr, S. Kharkovsky, R. Zoughi, and R. Austin, "Comparison of near-field millimeter-wave probes for detecting corrosion precursor pitting under paint," *IEEE Trans. Instr. Meas.* **54**, 1497-1504 (2005).
- [154] N. Qaddoumi, A. Shroyer, and R. Zoughi, "Microwave detection of rust under paint and composite laminates," *Res. Nondestr. Eval.* **9**, 201-212 (1997).
- [155] L. Diener, "Microwave near-field imaging with open-ended waveguide – Comparison with other techniques of nondestructive testing," *Res. Nondestr. Eval.* **7**, 137-152 (1995).
- [156] J. Bakerjarvis, C. Jones, B. Riddle, M. Janezic, R. G. Geyer, J. H. Grosvenor, and C. M. Weil, "Dielectric and magnetic measurements - a survey of nondestructive, quasi-nondestructive, and process-control techniques," *Res. Nondestr. Eval.* **7**, 117-136 (1995).
- [157] A. V. Mamishev, B. C. Lesieutre, and M. Zahn, "Optimization of multi-wavelength interdigital dielectrometry instrumentation and algorithms," *IEEE Trans. Dielectr. Electr. Insul.* **5**, 408-420 (1998).
- [158] S. D. Senturia and N. F. Sheppard, "Dielectric analysis of thermoset cure," *Adv. Polym. Sci.* **80**, 1-47 (1986).
- [159] A. A. Nassr and W. W. El-Dakhkhni, "Non-destructive evaluation of laminated composite plates using dielectrometry sensors," *Smart Mat. Struct.* **18**, 055014 (2009).
- [160] R. A. Pethrick, P. Boinard, and W. M. Banks, "Use of dielectric spectroscopy to assess adhesively bonded composite structures," *J. Adhes.* **78**, 1015-1026 (2002).
- [161] C. M. Stuart, "Thermoelectric differences used for metal sorting," *J. Testing Eval.* **15**, 224-230 (1987).
- [162] W. Morgner, "Introduction to Thermoelectric Nondestructive Testing," *Mat. Eval.* **9**, 1081-1088 (1991).
- [163] X. Kleber, "Detection of surface and subsurface heterogeneities by the hot tip thermoelectric power method," *NDT&E Int.* **41**, 364-370 (2008).
- [164] J. Hu and P. B. Nagy, "On the role of interface imperfections in thermoelectric nondestructive materials characterization," *Appl. Phys. Lett.* **73**, 467-469 (1998).
- [165] J. H. Hinken and Y. Tavrín, "Thermoelectric SQUID method for the detection of segregations," *Rev. Prog. Quant. Nondestr. Eval.* **19**, 2085-2092 (2000).
- [166] P. B. Nagy and A. H. Nayfeh, "On the thermoelectric magnetic field of spherical and

- cylindrical inclusions,” *J. Appl. Phys.* **87**, 7481-7490 (2000).
- [167] K. Maslov and V. K. Kinra, “Noncontact thermoelectric NDT for alloy microstructural analysis,” *Mater. Eval.* **59**, 1081-1084 (2001).
  - [168] A. H. Nayfeh, H. Carreon, and P. B. Nagy, “Role of anisotropy in noncontacting thermoelectric materials characterization,” *J. Appl. Phys.* **91**, 225-231 (2002).
  - [169] A. W. Szafranski, “Effect of dissolved hydrogen on electron transport in nickel–chromium alloys,” *J. Alloys Compd.* **340**, 54-61 (2002).
  - [170] P. Termsuksawad, S. Niyomsoan, R. B. Goldfarb, V. I. Kaydanov, D. L. Olson, B. Mishra, and X. Gavra, “Measurement of hydrogen in alloys by magnetic and electronic techniques,” *J. Alloys Compd.* **373**, 86-95 (2004).
  - [171] F. Sevini, B. Acosta, and L. Debarberis, “Combined thermo-electric power and resistivity measurements of embrittlement recovery in aged JRQ ferritic steel,” *Int. J. Press. Vess. Piping* **83**, 525-530 (2006).
  - [172] M. Niffenegger, K. Reichlin, and D. Kalkhof, “Application of the Seebeck effect for monitoring of neutron embrittlement and low-cycle fatigue in nuclear reactor steel,” *Nucl. Engg. Design* **235**, 1777-1788 (2005).
  - [173] H. Carreon, P. B. Nagy, and M. P. Blodgett, “Thermoelectric nondestructive evaluation of residual stress in shot-peened metals,” *Res. Nondestr. Eval.* **14**, 59-80 (2002).